UC Berkeley
UC Berkeley Electronic Theses and Dissertations

Title
Constraining sources and sinks of atmospheric trace gases: Spectroscopy and kinetics of C1-C3 Criegee intermediates and the isotopic composition of lightning-produced N2O

Permalink
https://escholarship.org/uc/item/0fj5x2w6

Author
Smith, Mica

Publication Date
2016

Peer reviewed|Thesis/dissertation

eScholarship.org Powered by the California Digital Library
University of California

Constraining sources and sinks of atmospheric trace gases: Spectroscopy and kinetics of C1-C3 Criegee intermediates and the isotopic composition of lightning-produced N_2O

By

Mica Caitlin Smith

A dissertation submitted in partial satisfaction of the

requirements for the degree of

Doctor of Philosophy

in

Chemistry

in the

Graduate Division

of the

University of California, Berkeley

Committee in charge:

Professor Kristie A. Boering, Chair
Professor Ronald C. Cohen
Professor Allen H. Goldstein

Summer 2016

Abstract

Constraining sources and sinks of atmospheric trace gases: Spectroscopy and kinetics of C1-C3 Criegee intermediates and the isotopic composition of lightning-produced N_2O

by

Mica Caitlin Smith

Doctor of Philosophy in Chemistry

University of California, Berkeley

Professor Kristie A. Boering, Chair

This dissertation presents a series of research projects designed and carried out to elucidate the physical chemistry and assess the atmospheric relevance of (1) carbonyl oxide radicals (*i.e.*, Criegee intermediates) produced in alkene ozonolysis and (2) nitrous oxide (N_2O) produced in lightning-induced corona discharges. The results provide UV absorption spectra and reaction rate coefficients for Criegee intermediates that will help constrain the formation and loss pathways of aerosol nucleation precursors such as H_2SO_4 and oxidized volatile organic compounds, and the isotopic signature of N_2O formed in lightning that can help distinguish various N_2O sources in atmospheric measurements.

Criegee intermediates are byproducts of the reaction of alkenes with ozone. Bimolecular reactions of Criegee intermediates can lead to the production of low-volatility organic compounds and acids in the atmosphere, which in turn play a role in determining the concentration, size, and optical properties of aerosols. Recently, a novel method for producing measurable quantities of stabilized Criegee intermediates in the laboratory paved the way for the development of new experimental techniques to study their chemical properties and predict their importance in the atmosphere. For this dissertation, a unique apparatus combining time-resolved UV absorption in a flow cell with laser depletion in a molecular beam was adapted to obtain the absolute absorption spectrum of CH_3CHOO with high resolution and accuracy relative to previous spectral measurements by other groups. The resulting absorption cross sections imply a photolysis lifetime of about seven seconds in the atmosphere, long enough for CH_3CHOO to participate in unimolecular and bimolecular reactions. The broad absorption band with weak structure in the long-wavelength region of the spectrum represents a "spectral fingerprint" for identifying CH_3CHOO in future studies, and the cross sections provide valuable benchmarks for theory to characterize electronically excited states of CH_3CHOO.

The fast reaction of CH_2OO with water dimer is thought to dominate CH_2OO removal in the atmosphere. However, reaction rates can vary considerably under different conditions of temperature, humidity, and pressure. A temperature-controlled flow cell was designed to measure the transient absorption of CH_2OO and obtain rate coefficients for its reaction with water dimer from 283 to 324 K. The rate of the reaction of CH_2OO with water dimer was found to exhibit a strong negative temperature dependence, pointing to the participation of a hydrogen-bonded pre-reactive complex between CH_2OO and two water molecules. Due to the strong temperature dependence, and shifting competition between water dimer and water monomer (which has a positive temperature dependence), the effective loss rate of CH_2OO by reaction with water vapor is highly sensitive to atmospheric conditions. The role played by the stable pre-reactive complex suggests that similar complexes could form between water dimer

and other larger Criegee intermediates, and that the stability and relative energy of these complexes control the reaction rate with water and its temperature dependence.

Effective loss rates of Criegee intermediates due to bimolecular reactions in the atmosphere are limited by their rates of unimolecular decomposition. The rates of decomposition depend strongly on the molecular geometry, which affects the accessible isomerization pathways and dissociation products. $(CH_3)_2COO$ is the main product of tetramethylethylene ozonolysis, and has been found to react slowly with water dimer and rapidly with SO_2. While CH_2OO decomposes slowly via isomerization to dioxirane, $(CH_3)_2COO$ may decompose faster via intramolecular hydrogen transfer to form vinyl hydroperoxide. Fast $(CH_3)_2COO$ decomposition could affect the significance of the Criegee intermediate H_2SO_4 source, as well as the non-photolytic production of OH radicals. In this dissertation, measurements of the transient absorption of $(CH_3)_2COO$ to obtain thermal decomposition rate coefficients from 283 to 323 K by extrapolating the observed loss rate to zero concentration are reported. The rate of unimolecular decomposition is ~400 s^{-1} at 298 K and varies by nearly an order of magnitude within the studied temperature range. The effective loss rate of $(CH_3)_2COO$ in the atmosphere due to thermal decomposition is thus competitive with its loss due to reaction with water vapor and with SO_2, suggesting that the unimolecular decomposition pathway is a significant sink for $(CH_3)_2COO$ and possibly other di-substituted Criegee intermediates, and should be included in models of Criegee chemistry in the atmosphere as well as in kinetic models of tetramethylethylene ozonolysis.

N_2O is the third most important greenhouse gas after CO_2 and methane, and is mainly emitted to the atmosphere as a byproduct of microbial activity in soils. The expanding use of nitrogen-containing fertilizers in agriculture has led to an increase in N_2O atmospheric concentrations since preindustrial times. Isotopic measurements are a valuable tool to distinguish the influence of different sources of N_2O, but the isotopic composition of N_2O formed from corona discharge in lightning has not previously been measured. Here, a corona discharge cell apparatus was used to generate a corona discharge in flowing or static zero air, and the N_2O formed at discharge cell pressures from ~0.1 to 10 Torr and discharge voltages from 0.25 to 5 kV was collected and measured with isotope ratio mass spectrometry to determine its isotopic composition. The results show enrichments in ^{15}N of N_2O up to 32‰ relative to the reactant N_2, and even larger enrichments in ^{15}N of up to 77‰ at the central nitrogen atom. Large depletions in ^{18}O as large as -71‰ relative to reactant O_2 were also measured. The isotopic composition measured here may help to elucidate the chemical mechanisms leading to N_2O formation and destruction in a corona discharge. Furthermore, the isotope-isotope relationships of the N_2O produced in the corona discharge experiments are distinct from those of N_2O from other sources, implying that isotopic measurements can be used to determine whether local variations in the atmospheric concentration of N_2O – *e.g.*, the enhanced N_2O levels recently measured in the upper tropical and subtropical troposphere – are due to lightning activity, soil emissions, or biomass burning.

For Mom, Dad, and Andrew

Table of Contents

List of Figures

List of Tables

Acknowledgements

The road to this point has been long, spanning years and oceans. I would never have gotten here without the continuous support of great friends. Among them I want to thank my first Berkeley roommate Katie who helped me ease in to grad school life; my best friend and roommate Dawn who is always up for a spur-of-the-moment camping trip; and the kids at Chem Keg, physics hour, and Stanley Hall common room who made sure I put down the lab goggles and lifted my spirits on Friday afternoons.

I owe much to the mentors and colleagues that have collaborated with and guided me through these years. My advisor Kristie Boering introduced me to the world of atmospheric chemistry and isotope effects, providing lots of advice and encouragement along the way. Thanks are due to Aaron and John for helping me find my way around the lab, Amadu for offering jokes and pep talks at every group meeting, Lauren and Armando for braving Taiwan with me, and Quinby for her hard work and upbeat attitude in the summer of 2015. In addition, the team in Taiwan deserves recognition. Many thanks to Jim and YT for welcoming me to the lab at IAMS, and to a series of helpful labmates including Grace, Man-Nung, Allen, Guang-Tou, Jenny, and Zhao Wen. Thanks as well to my committee members Ron Cohen and Allen Goldstein for their patience and understanding in the final months of my journey down this extraordinary road.

To my undergraduate advisor, who believed in me more than I believed in myself: thank you for sparking my fascination with physical chemistry and fanning the flames that led me to UC Berkeley.

CHAPTER 1: Overview

1.1 Introduction

Increasing media and political focus on global warming has highlighted the importance of understanding the chemistry and composition of the atmosphere. The rise in temperature attributed to anthropogenic changes in atmospheric composition is caused by the trapping of outgoing infrared radiation by greenhouse gases (GHGs); however, accurately predicting the magnitude of this temperature rise and its effect on our climate will require an improved understanding of regional, seasonal, and diurnal variations in the source and sink magnitudes of GHGs, as well as the radiative heating or cooling effects of aerosols.

To reduce the uncertainties in these factors, it is necessary to elucidate the fundamental chemistry of key reactions that govern concentrations of aerosols and/or GHGs in the atmosphere. For example, reactions leading to aerosol formation involve short-lived radicals that oxidize volatile organic compounds (VOCs), forming low-volatility organic compounds (LVOCs) which can partition into the condensed phase. The properties and atmospheric reactivity of these oxidizing radicals may influence the optical and radiative properties of the resulting aerosols (such as sulfuric acid and secondary organic aerosol). Reactions leading to GHG formation and destruction are also of considerable interest, particularly non-CO_2 GHGs such as CH_4 and N_2O, the significance of which has historically been downplayed relative to concerns over the rise in CO_2, but is likely to grow as rates of food production, for example, increase worldwide.

In this dissertation, I present several investigations into the physical chemistry of key species in the atmosphere. This work includes (1) UV spectral features and reaction kinetics of Criegee intermediates, a class of highly reactive radical oxidants produced in the atmosphere by the reaction of ozone with natural and anthropogenic hydrocarbons, and (2) the isotopic composition of N_2O, the third most important anthropogenic greenhouse gas, produced in the laboratory in a corona discharge to simulate atmospheric production by lightning. The results of these investigations expand current understanding of the atmospheric sinks of Criegee intermediates, and provide benchmark measurements for (1) improving estimates of aerosol concentrations and (2) identifying and partitioning natural and anthropogenic influences on atmospheric N_2O concentrations.

1.2 UV spectrum and reaction kinetics of Criegee intermediates (Chapters 2-4)

In Chapters 2, 3, and 4, I describe my experiments using and modifying an apparatus at the Institute for Atomic and Molecular Sciences (IAMS), Academia Sinica, Taipei, Taiwan, consisting of a gas flow reactor, iCCD camera, and balanced photodiode detector to produce and detect Criegee intermediates with high time resolution and sensitivity. In these chapters, previously elusive properties such as UV absorption cross sections and temperature-dependent bimolecular reaction rate coefficients are determined with accuracy and precision. Since the apparatus operates under atmospheric pressures, temperatures, and humidities while maintaining stability in the experimental conditions over the time required to achieve a high signal-to-noise ratio, it is uniquely well-suited for probing Criegee intermediate spectral properties and reaction kinetics.

Criegee intermediates are produced during alkene ozonolysis (*i.e.*, the reaction of alkenes with ozone), which is a central component of gas-phase chemistry in Earth's troposphere. Short-

chain and branched alkenes are emitted from vehicle exhaust pipes, while alkenes with more complex structures such as α-pinene can be emitted by plants and trees. Ozone is produced in the stratosphere via O_2 photolysis or by the photochemical oxidation of VOCs in the lower troposphere. Hence, in the troposphere, alkene ozonolysis is ubiquitous in both urban and forested regions. In 1949, Rudolph Criegee proposed a mechanism for alkene ozonolysis involving (1) the formation of a primary ozonide and (2) subsequent cleavage of an O-O bond and a bond in the alkyl group to form a carbonyl oxide such as CH_2OO (Figure 1.1).[1] The carbonyl oxide, or Criegee intermediate, is formed with a large amount of internal energy (>50 kcal mol^{-1})[2] and may rapidly isomerize to another species such as dioxirane, or thermally decompose, before it can be collisionally stabilized under atmospheric conditions. The fraction of Criegee intermediates that survive long enough to be collisionally stabilized can participate in bimolecular reactions with species such as SO_2, NO_2, and VOCs, and are therefore a subject of great interest in atmospheric chemistry. Since "hot" Criegee intermediates were not measured in the experiments described in Chapter 2-4, this dissertation concerns only the stabilized fraction, hereafter referred to as "CIs".

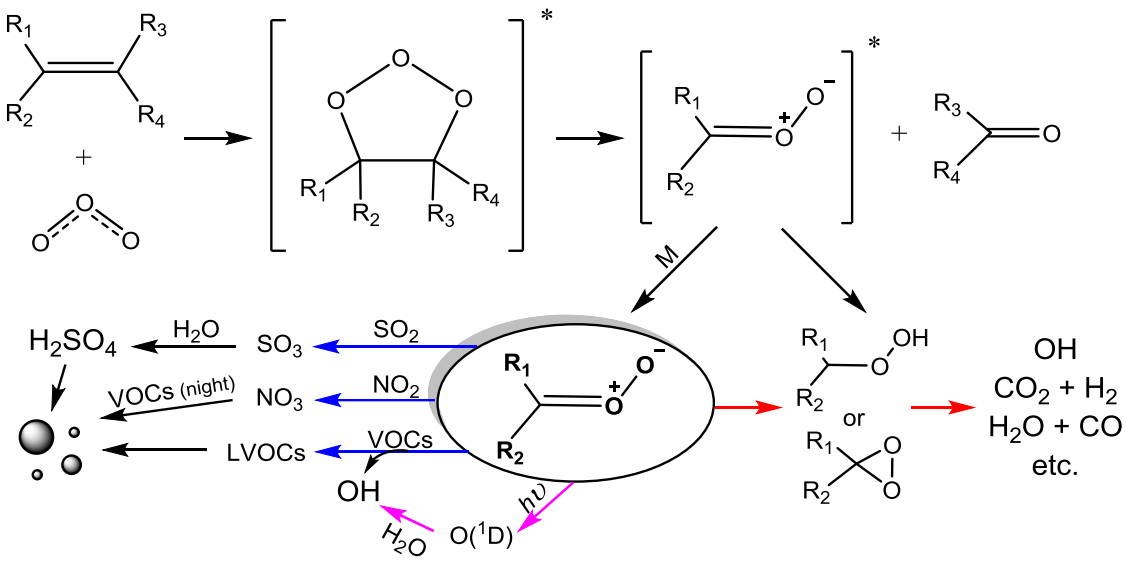

Figure 1.1. Formation of CIs and example loss pathways via bimolecular reaction (blue), UV photolysis (magenta), and unimolecular decomposition following isomerization (red).

The reactions of CIs with SO_2 garnered considerable attention in 2012 when Mauldin *et al.*[3] reported results from a combined observational and laboratory study which indicated a missing sink of SO_2, and hence a missing source of H_2SO_4, to the atmosphere. The group postulated that CIs could account for the discrepancies between their measurements and model predictions of SO_2 and H_2SO_4. Gas-phase H_2SO_4 is well established as a precursor to aerosol formation and poses an environmental concern as a precursor to acid rain.

The role for CIs in SO_2 oxidation suggested by Mauldin *et al.*[3] was at odds with previous laboratory investigations that reported slow reaction rates of CIs with SO_2.[4,5] These investigations produced CIs using the ozonolysis reaction, which forms a wide variety of other

products that can interfere with kinetics measurements. They also employed indirect detection methods to infer the properties and reaction kinetics of CIs; for example, the reaction rate of CH_2OO with SO_2 was estimated by monitoring the formation of OH (a CI decomposition product) with and without SO_2 during ethene ozonolysis.[5] The resulting rate coefficients varied over several orders of magnitude among different groups and had large uncertainties, but no direct CI measurement method was available to constrain them, since typical steady state concentrations of CIs produced from ozonolysis are too low to detect with current measurement capabilities.

Then, a breakthrough occurred in 2012 with the introduction by Welz *et al.*[6] of a new method for preparing CIs in the laboratory at much higher steady state concentrations than those produced in ozonolysis. With this method (hereafter called the "diiodo" method), the direct detection of CH_2OO and other CIs became possible. In the diiodo method, as shown in Figure 1.2, one iodine atom is cleaved from a diiodoalkane precursor such as CH_2I_2 (*e.g.*, via photolysis at 248 nm) in the presence of O_2. The remaining iodine atom in the resulting iodoalkyl radical is rapidly replaced by O_2, producing CH_2OO in an almost thermoneutral reaction (ΔH_{rxn} ~ -1 kcal mol^{-1})[7] and with very few side products (*e.g.*, no isomers such as dioxirane or formic acid to complicate mass spectrometric studies)[6]. Welz *et al.*[6] used the diiodo method to show that the reaction of CH_2OO with SO_2 was 1-4 orders of magnitude faster than previous estimates from indirect laboratory measurements, thus confirming that CI reaction kinetics were not properly characterized and suggesting that other reaction rates may have been underestimated.

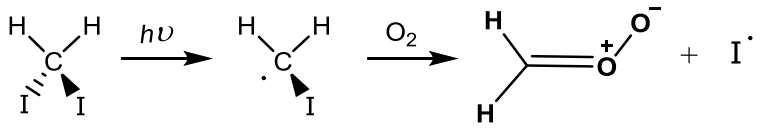

Figure 1.2. Reaction scheme of the diiodo method for producing CH_2OO.

The simplicity, controllability, and adaptability of the diiodo method inspired a number of studies revisiting CI reaction kinetics and chemical properties, which a recent review has covered in detail.[2] Since CIs cannot be measured in the atmosphere, a complete characterization of possible CI loss pathways (including photodissociation, bimolecular reactions, and unimolecular decomposition) in the laboratory is necessary in order to estimate their steady state concentrations in the atmosphere and their influence on the concentrations of other key species such as H_2SO_4 and organic aerosol precursors. Novel approaches to CI measurements in the laboratory, with the help of the diiodo method, can offer new capabilities for probing the physical chemistry of CIs.

The set of laboratory techniques I describe in this dissertation represent a unique approach to obtaining reaction rate coefficients of CIs under a wide range of atmospherically relevant conditions via their strong UV absorption. First, I demonstrate in Chapter 2 the measurement of CI UV absorption and the determination of wavelength-resolved absorption cross sections, which are required for accurate measurements of CI reaction rates and for estimates of UV photolysis of CIs in the atmosphere. Then, I present in Chapters 3 and 4 the first quantitative measurements of the temperature dependence of CI reactions, which is an important metric for

understanding how the competition between various CI reaction pathways changes under different atmospheric conditions, as well as the features of the potential energy surface governing the reaction mechanism.

To enable kinetics measurements of CIs using UV absorption methods, accurate quantitative UV spectra are required. In 2012 and 2013, the UV absorption bands of CH_2OO (the simplest CI) were measured by several groups using different detection techniques,[8,9] but significant discrepancies were evident among the resulting spectra. One group also reported the UV absorption of CH_3CHOO, the next simplest CI with a single methyl substituent.[10] In 2014, Professor Jim Lin of IAMS used two new and complementary detection techniques – transient absorption in a flow cell and laser depletion in a molecular beam – to obtain the absorption spectrum of CH_2OO;[11] the resulting spectrum has been supported by subsequent theoretical and experimental studies (*e.g.*, Refs. 12,13), signifying that this method is reliable and accurate. In the published study reproduced in Chapter 2,[14] I extended this work to directly measure the UV absorption spectrum of the C2 Criegee intermediate CH_3CHOO. Combining time-resolved UV absorption under near-atmospheric conditions with sensitive detection of CH_3CHOO laser depletion in a molecular beam, I acquired absolute UV absorption cross sections which can be used to estimate the contribution of loss via photolysis to CH_3CHOO concentrations in the atmosphere. In addition, the measured strong absorption band provides a spectral fingerprint that can be used to measure CH_3CHOO in future spectroscopic studies.

In a subsequent experimental study by Prof. Lin using this apparatus,[15] it was found that CH_2OO reacts rapidly with water dimer. Considering the high abundance of water vapor in the atmosphere, this fast reaction rate would suggest that water is the dominant sink for CH_2OO in the atmosphere, thus diminishing the potential importance of SO_2 or VOC oxidation. However, the effective loss rate of CH_2OO due to reaction with water may depend on temperature and humidity conditions in the atmosphere. In the published work reproduced in Chapter 3,[16] I modified the apparatus introduced in Chapter 2 to achieve precise temperature control and high relative humidities in the reaction system, and measured temperature-dependent rate coefficients for the reaction of CH_2OO with water vapor. The results show that the rate of the CH_2OO reaction with water dimer indeed varies substantially under different atmospheric conditions. Furthermore, both the kinetic data and theoretical work[16] show that the formation of a stable pre-reactive complex between CH_2OO and water dimer lowers the barrier height of the reaction, resulting in a strong negative temperature dependence. The temperature-dependent rate coefficients can be used to improve theoretical treatments of this key CI reaction (see Ref. 17) and to constrain the reactivity of CH_2OO in different regions of the atmosphere.

The hydroxyl radical (OH) is another key species that can be produced in CI reactions, via decomposition of products from CI bimolecular reactions, atmospheric photolysis, or unimolecular decomposition (see Figure 1.1). Evidence for an unaccounted-for non-photolytic source of OH in forested regions was reported by Heard *et al.*,[18] whose measurements of OH concentrations were up to an order of magnitude higher than the predicted concentrations based on ozone photolysis. Although at least some of the instances of very large concentrations of HO_x may be an artifact due to an interference in the detection method (*e.g.*, Refs. 19,20), it is also thought that the dimethyl CI $(CH_3)_2COO$ has a faster rate of unimolecular decomposition than CIs with lower carbon numbers (CH_2OO or CH_3CHOO) which have been more widely studied.[21–23] Hence, it is possible that $(CH_3)_2COO$ and CIs with similar structures play a central role in non-photolytic OH production. Previously reported unimolecular decomposition rates for $(CH_3)_2COO$ varied by two orders of magnitude,[22–25] however, so more accurate rates are needed to assess their potential importance in the atmosphere. In the published work

reproduced in Chapter 4,[26] I measured thermal decomposition rates of $(CH_3)_2COO$ by monitoring time-resolved UV absorption at different $(CH_3)_2COO$ concentrations, and fit the data to a kinetics model to derive unimolecular reaction rate coefficients as a function of temperature. The reported rates are the first to be determined from direct measurements under thermal conditions, and indicate that thermal decomposition may compete with water and SO_2 scavenging for $(CH_3)_2COO$ loss in the atmosphere.

1.3 Isotopic composition of N_2O produced in a corona discharge (Chapter 5)

In Chapter 5, I present the first direct measurements of the isotopic composition of N_2O formed in zero air in a corona discharge, using an apparatus designed and constructed in our laboratory. The dependence of the N_2O yields and bulk and site-specific isotopic composition on corona discharge voltage and pressure is analyzed and compared with aspects of several previous indirect studies and compared with known sources and sinks of N_2O. At the highest pressures studied (5-10 Torr), large enrichments in the average ^{15}N isotopic composition ($\delta^{15}N$ up to +32‰, or parts per thousand relative to ^{14}N and to the $^{15}N/^{14}N$ ratio in reactant N_2; see Chapter 5 for a description of δ-value notation) and in the ^{15}N isotopic composition at the central (α) nitrogen atom position ($\delta^{15}N^{\alpha}$ up to +77‰) were measured, while large depletions in the ^{18}O isotopic composition were observed. I use these isotope characteristics to speculate on the dominant reaction pathway(s) leading to N_2O formation in a corona discharge, which are currently not well-understood, and to explore the feasibility of using isotope-isotope relationships (*e.g.*, $\delta^{15}N$ vs. $\delta^{18}O$ or $\delta^{15}N$ vs. $\delta^{15}N^{\alpha}$) for N_2O from corona discharge to distinguish the underlying cause of local or regional variations in N_2O concentrations, such as the enhanced N_2O levels recently measured in regions of the upper troposphere which could be attributed to production by lightning, biomass burning, lofting of surface air influenced by soil emissions, or transport from the stratosphere.

N_2O has a lifetime of 120 years[27] and has contributed 4-18% of the total increase in radiative forcing by GHGs in the atmosphere since 1750, making it the third most important anthropogenic GHG after CO_2 and CH_4.[27] The majority of N_2O emissions to the atmosphere comes from microbial activity in soils (estimated at almost 60% of total N_2O sources to the atmosphere each year).[28,29] Production of N_2O from biomass burning and fossil fuel combustion also contribute to the total N_2O source budget (~4% and ~6% respectively).[28,29] Finally, atmospheric sources (such as the oxidation of NH_3 and production by lightning) contribute about 3% to the sum of all N_2O sources each year.[28] The main sink (~90%) for N_2O is photolysis at UV wavelengths between 195 and 230 nm in the stratosphere to form N_2 + $O(^1D)$. The remaining 10% of N_2O loss in the stratosphere each year is due to reaction with $O(^1D)$, forming either N_2 + O_2 or NO, and hence leads to the production of NO_x in the stratosphere which plays a role in the catalytic destruction of stratospheric ozone.[30] Figure 1.3 summarizes the sources and sinks of N_2O.

Although CO_2 is the GHG targeted most aggressively by policy recommendations due to the large magnitude of its anthropogenic sources, N_2O has a global warming potential 265 times that of CO_2.[27] Furthermore, the concentration of N_2O in the atmosphere has been increasing by 0.3% per year over the last few decades[31] and has increased by 20% since 1750.[27] Although the imbalance of the budget of sources and sinks in Figure 1.3 is roughly in agreement with the measured increase in the atmosphere,[27] there are still large uncertainties in the contributions of various sources and, as a corollary, in how their magnitudes may therefore change as climate changes.

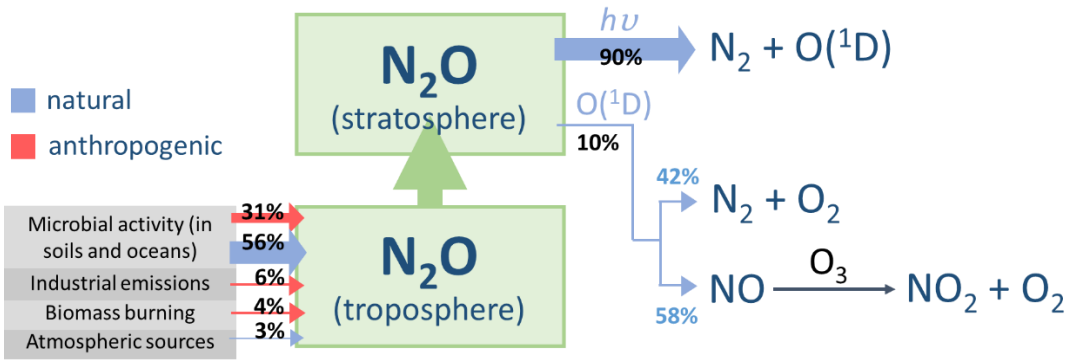

Figure 1.3. Schematic of N_2O sources and sinks.

One means of obtaining a better mechanistic understanding of the imbalance of the sources and sinks of N_2O is from measurements of its isotopic composition. For example, Park *et al.*[32] recently used measurements of the nitrogen, site-specific nitrogen, and oxygen isotopic composition and the mixing ratios of N_2O in Antarctic firn air (with a mean age dating back to 1940) and in archived air from Tasmania (dating back to 1978) to demonstrate that the increase in N_2O since 1940 is mainly due to the increased use of nitrogen-containing fertilizers. These observations and their analysis also demonstrated that isotopic composition measurements can be used to distinguish variations in N_2O concentrations due to transport of N_2O-depleted air from the stratosphere to the Earth's surface from variations due to differences in the magnitudes and timing of N_2O emitted from soils or from the oceans, since the isotopic signature (combination of the nitrogen and oxygen isotopic composition) of the sources and sink are so different. Thus, because the influence of stratosphere-troposphere exchange on N_2O concentrations at the Earth's surface is the largest uncertainty in inverse model estimates of the geographic distribution and timing of N_2O sources to the atmosphere,[33,34] including isotope measurements in studies of atmospheric N_2O may greatly reduce uncertainties in our mechanistic understanding of N_2O sources to the atmosphere and how they change over time.

Notably, both inverse modeling studies of N_2O concentrations[33–38] and recent observations of unexpectedly high N_2O mixing ratios in the tropical and subtropical upper troposphere during the HIPPO campaign[39,40] suggest that some tropical or subtropical source(s) of N_2O are larger than previous estimates. Some possible sources are lofting of surface air influenced by tropical soil or ocean emissions, biomass burning, or production in thunderstorms (by corona discharge), all of which could potentially be larger in the tropics than elsewhere. The least characterized of these sources, both mechanistically and isotopically, is production in a corona discharge, a low-current electrical discharge that occurs in lightning storms. High levels of N_2O have been measured in the atmosphere during some thunderstorms,[41] and laboratory studies simulating corona discharge in atmospheric lightning observed the production of large amounts of N_2O.[42] Furthermore, several experimental studies have suggested there might be large ^{15}N enrichments in nitrogen atoms or in nitrogen oxides produced in plasma discharges.[43–45] Although the global source of N_2O from lightning is expected to be only a very small fraction of the total N_2O sources (0.0004 Tg y^{-1}, or ~0.002%),[46] a large isotopic signature that is distinct from that of the other N_2O sources and sink may be detectable in the atmosphere, such that measurements of the N_2O isotopic composition in air showing N_2O enhancements in the tropics, as during HIPPO, could be used to determine whether the enhancements are due to lightning activity.

In Chapter 5, I present measurements of the isotopic composition of N_2O formed in a corona discharge in flowing zero air (N_2 and O_2) as a function of pressure and discharge voltage. I compare the resulting yields and isotopic composition of N_2O with previous (albeit indirectly relevant) laboratory studies of the ^{15}N enrichments of nitrogen atoms and nitrogen oxides produced in electric discharges, as well as with the known isotopic signatures of other N_2O sources and sinks. The large enrichments in ^{15}N and large depletions in ^{18}O in N_2O measured at the highest pressures are (1) likely to be large enough to be measurable even for N_2O changes of only 1 or 2 ppbv (as were observed in HIPPO) and (2) distinct from the isotopic signatures for microbial sources (which show depletions in ^{15}N and ^{18}O relative to reactant air with a strong ^{15}N site preference, *i.e.*, ^{15}N enrichment at the central nitrogen atom relative to the terminal nitrogen atom), transport of residual stratospheric N_2O (which shows enrichments in ^{15}N and ^{18}O and a strong ^{15}N site preference), and biomass burning (depletion in ^{18}O with ^{15}N similar to air N_2). Therefore, isotopic analysis of whole air samples collected in regions of small but significant enhancements in N_2O concentrations on future missions may allow the source of the enhanced N_2O to be determined. In addition, the dependence of the N_2O isotopic composition on the corona discharge voltage and pressure and flow conditions, which suggests shifting competition among various mechanisms of N_2O formation and destruction in the discharge, will be useful for understanding the physical chemistry of N_2O formation in a corona discharge, *e.g.*, by incorporating isotope effects into a kinetics model of the discharge chemistry.

References

1. Criegee, R. & Wenner, G. Die Ozonisierung des 9,10-Oktalins. *Justus Liebigs Ann. Chem.* **564,** 9–15 (1949).
2. Osborn, D. L. & Taatjes, C. A. The physical chemistry of Criegee intermediates in the gas phase. *Int. Rev. Phys. Chem.* **34,** 309–360 (2015).
3. Mauldin III, R. L. *et al.* A new atmospherically relevant oxidant of sulphur dioxide. *Nature* **488,** 193–196 (2012).
4. Hatakeyama, S. & Akimoto, H. Reactions of Criegee intermediates in the gas phase. *Res. Chem. Intermed.* **20,** 503–524 (1994).
5. Johnson, D., Lewin, A. G. & Marston, G. The effect of Criegee-intermediate scavengers on the OH yield from the reaction of ozone with 2-methylbut-2-ene. *J. Phys. Chem. A* **105,** 2933–2935 (2001).
6. Welz, O. *et al.* Direct kinetic measurements of Criegee intermediate (CH_2OO) formed by reaction of CH_2I with O_2. *Science* **335,** 204–207 (2012).
7. Lee, E. P. F. *et al.* Spectroscopy of the simplest Criegee intermediate CH_2OO: simulation of the first bands in its electronic and photoelectron spectra. *Chem. – Eur. J.* **18,** 12411–12423 (2012).
8. Beames, J. M., Liu, F., Lu, L. & Lester, M. I. Ultraviolet spectrum and photochemistry of the simplest Criegee intermediate CH_2OO. *J. Am. Chem. Soc.* **134,** 20045–20048 (2012).
9. Sheps, L. Absolute ultraviolet absorption spectrum of a Criegee intermediate CH_2OO. *J. Phys. Chem. Lett.* **4,** 4201–4205 (2013).
10. Beames, J. M., Liu, F., Lu, L. & Lester, M. I. UV spectroscopic characterization of an alkyl substituted Criegee intermediate CH_3CHOO. *J. Chem. Phys.* **138,** 244307 (2013).
11. Ting, W.-L., Chen, Y.-H., Chao, W., Smith, M. C. & Lin, J. J.-M. The UV absorption spectrum of the simplest Criegee intermediate CH_2OO. *Phys. Chem. Chem. Phys.* **16,** 10438 (2014).
12. Dawes, R., Jiang, B. & Guo, H. UV absorption spectrum and photodissociation channels of the simplest Criegee intermediate (CH_2OO). *J. Am. Chem. Soc.* **137,** 50–53 (2015).
13. Foreman, E. S. *et al.* High resolution absolute absorption cross sections of the $\tilde{B}^1A'$–$\tilde{X}^1A'$ transition of the CH_2OO biradical. *Phys. Chem. Chem. Phys.* **17,** 32539–32546 (2015).
14. Smith, M. C. *et al.* UV absorption spectrum of the C2 Criegee intermediate CH_3CHOO. *J. Chem. Phys.* **141,** 74302 (2014).
15. Chao, W., Hsieh, J.-T., Chang, C.-H. & Lin, J. J.-M. Direct kinetic measurement of the reaction of the simplest Criegee intermediate with water vapor. *Science* **347,** 751–754 (2015).
16. Smith, M. C. *et al.* Strong negative temperature dependence of the simplest Criegee intermediate CH_2OO reaction with water dimer. *J. Phys. Chem. Lett.* **6,** 2708–2713 (2015).
17. Lin, L.-C. *et al.* Competition between H_2O and $(H_2O)_2$ reactions with CH_2OO/CH_3CHOO. *Phys. Chem. Chem. Phys.* **18,** 4557–4568 (2016).
18. Heard, D. E. *et al.* High levels of the hydroxyl radical in the winter urban troposphere. *Geophys. Res. Lett.* **31,** L18112 (2004).
19. Fuchs, H. *et al.* Detection of HO_2 by laser-induced fluorescence: calibration and interferences from RO_2 radicals. *Atmos. Meas. Tech.* **4,** 1209–1225 (2011).
20. Whalley, L. K., Blitz, M. A., Desservettaz, M., Seakins, P. W. & Heard, D. E. Reporting the sensitivity of laser-induced fluorescence instruments used for HO_2 detection to an interference from RO_2 radicals and introducing a novel approach that enables HO_2 and certain RO_2 types to be selectively measured. *Atmos. Meas. Tech.* **6,** 3425–3440 (2013).

21. Martinez, R. I. & Herron, J. T. Stopped-flow studies of the mechanisms of ozone-alkene reactions in the gas phase: tetramethylethylene. *J. Phys. Chem.* **91,** 946–953 (1987).
22. Berndt, T. *et al.* H_2SO_4 formation from the gas-phase reaction of stabilized Criegee Intermediates with SO_2: Influence of water vapour content and temperature. *Atmos. Environ.* **89,** 603–612 (2014).
23. Newland, M. J. *et al.* Kinetics of stabilised Criegee intermediates derived from alkene ozonolysis: reactions with SO_2 , H_2O and decomposition under boundary layer conditions. *Phys. Chem. Chem. Phys.* **17,** 4076–4088 (2015).
24. Kroll, J. H., Sahay, S. R., Anderson, J. G., Demerjian, K. L. & Donahue, N. M. Mechanism of HO_x formation in the gas-phase ozone-alkene reaction. 2. Prompt versus thermal dissociation of carbonyl oxides to form OH. *J. Phys. Chem. A* **105,** 4446–4457 (2001).
25. Berndt, T. *et al.* Gas-phase ozonolysis of selected olefins: the yield of stabilized Criegee intermediate and the reactivity toward SO_2. *J. Phys. Chem. Lett.* **3,** 2892–2896 (2012).
26. Smith, M. C., Chao, W., Takahashi, K., Boering, K. A. & Lin, J. J.-M. Unimolecular decomposition rate of the Criegee intermediate $(CH_3)_2COO$ measured directly with UV absorption spectroscopy. *J. Phys. Chem. A* **120**, 4789-4798 (2016).
27. Stocker, T. F. *et al.* IPCC, 2013: Climate change 2013: the physical science basis. Contribution of working group I to the fifth assessment report of the intergovernmental panel on climate change (2013).
28. Stein, L. Y. & Yung, Y. L. Production, isotopic composition, and atmospheric fate of biologically produced nitrous oxide. *Annu. Rev. Earth Planet. Sci.* **31,** 329–356 (2003).
29. Bouwman, L. & United Nations Environment Programme. Drawing down N_2O to protect climate and the ozone layer: a UNEP synthesis report (2013).
30. Ravishankara, A. R., Daniel, J. S. & Portmann, R. W. Nitrous oxide (N_2O): The dominant ozone-depleting substance emitted in the 21st century. *Science* **326,** 123–125 (2009).
31. Davidson, E. A. The contribution of manure and fertilizer nitrogen to atmospheric nitrous oxide since 1860. *Nat. Geosci.* **2,** 659–662 (2009).
32. Park, S. *et al.* Trends and seasonal cycles in the isotopic composition of nitrous oxide since 1940. *Nat. Geosci.* **5,** 261–265 (2012).
33. Hirsch, A. I. *et al.* Inverse modeling estimates of the global nitrous oxide surface flux from 1998–2001. *Glob. Biogeochem. Cycles* **20,** GB1008 (2006).
34. Huang, J. *et al.* Estimation of regional emissions of nitrous oxide from 1997 to 2005 using multinetwork measurements, a chemical transport model, and an inverse method. *J. Geophys. Res. Atmospheres* **113,** D17313 (2008).
35. Thompson, R. L. *et al.* Nitrous oxide emissions 1999 to 2009 from a global atmospheric inversion. *Atmos. Chem. Phys.* **14,** 1801–1817 (2014).
36. Thompson, R. L. *et al.* TransCom N_2O model inter-comparison – Part 2: Atmospheric inversion estimates of N_2O emissions. *Atmos. Chem. Phys.* **14,** 6177–6194 (2014).
37. Saikawa, E. *et al.* Global and regional emissions estimates for N_2O. *Atmos. Chem. Phys.* **14,** 4617–4641 (2014).
38. Bergamaschi, P. *et al.* Top-down estimates of European CH_4 and N_2O emissions based on four different inverse models. *Atmos. Chem. Phys.* **15,** 715–736 (2015).
39. Wofsy, S. C. & the HIPPO Science Team and Cooperating Modellers and Satellite Teams. HIAPER Pole-to-Pole Observations (HIPPO): fine-grained, global-scale measurements of climatically important atmospheric gases and aerosols. *Philos. Trans. R. Soc. Math. Phys. Eng. Sci.* **369,** 2073–2086 (2011).
40. Kort, E. A. *et al.* Tropospheric distribution and variability of N_2O: Evidence for strong tropical emissions. *Geophys. Res. Lett.* **38,** L15806 (2011).

41. Levine, J. S. & Shaw, E. F. In situ aircraft measurements of enhanced levels of N_2O associated with thunderstorm lightning. *Nature* **303,** 312–314 (1983).
42. Hill, R. D., Rahmim, I. & Rinker, R. G. Experimental study of the production of NO, N_2O, and O_3 in a simulated atmospheric corona. *Ind. Eng. Chem. Res.* **27,** 1264–1269 (1988).
43. Basov, N. G. *et al.* Isotope separation in chemical reactions occurring under thermodynamic nonequilibrium conditions. *JETP Lett. USSR Engl. Transl. V 19 No 6 Pp 190-191* (1974).
44. Manuccia, T. J. & Clark, M. D. Enrichment of N^{15} by chemical reactions in a glow discharge at 77 °K. *Appl. Phys. Lett.* **28,** 372–374 (1976).
45. Gorshunov, N. M. & Gudenko, S. V. Enrichment of the nitrogen atomic component with the ^{15}N isotope in a post-discharge zone. *J. Exp. Theor. Phys. Lett.* **77,** 162–166 (2003).
46. Schumann, U. & Huntrieser, H. The global lightning-induced nitrogen oxides source. *Atmos. Chem. Phys.* **7,** 3823–3907 (2007).
47. Trapp, R. J. *et al.* Changes in severe thunderstorm environment frequency during the 21st century caused by anthropogenically enhanced global radiative forcing. *Proc. Natl. Acad. Sci.* **104,** 19719–19723 (2007).
48. Diffenbaugh, N. S., Scherer, M. & Trapp, R. J. Robust increases in severe thunderstorm environments in response to greenhouse forcing. *Proc. Natl. Acad. Sci.* **110,** 16361–16366 (2013).

Chapter 2

UV absorption spectrum of the C2 Criegee intermediate CH_3CHOO

Adapted with permission of all coauthors from M. C. Smith, W.-L. Ting, C.-H. Chang, K. Takahashi, K. A. Boering, J. J.-M. Lin, J. Chem. Phys. **141**, 074302 (2014).

2.1 Introduction

Carbonyl oxides, or Criegee intermediates, have been studied extensively with the aim of understanding their chemical properties and their role as oxidizers in the troposphere.[1, 2] Criegee proposed the formation of such intermediates in the reaction of ozone with unsaturated hydrocarbons.[3, 4] An example is shown in (R1) for ethene. The carbonyl oxide formed (*e.g.*, CH_2OO) may subsequently decompose, undergo photolysis, or react with other species. Because the formation of Criegee intermediates during ozone-alkene reactions is much slower than their decomposition,[5, 6] these species typically have low steady-state concentrations, which have hindered efforts to directly detect Criegee intermediates in the laboratory until recently.[7]

(R1) $CH_2{=}CH_2 + O_3 \rightarrow CH_2OO + CH_2O \rightarrow$ products

The simplest Criegee intermediate, CH_2OO, was directly observed by Welz *et al.*[8] using tunable vacuum UV photoionization mass spectrometry (PIMS), a sensitive technique that allowed separation of CH_2OO from its various isomers on the basis of ionization energies. Remarkably, their work introduced an efficient method for producing CH_2OO and other Criegee intermediates, by preparing CH_2I_2 (or a corresponding diiodoalkane) in O_2 and irradiating the mixture with UV light. CH_2OO is then produced by the reaction of the resulting CH_2I with O_2.

Subsequent studies have adapted this synthesis scheme to characterize vibrational,[9] rotational[10] and electronic states[11-14] of CH_2OO, as well as its reactivity with atmospheric species such as SO_2, NO_2, and volatile organic compounds.[8, 15-20] Notably, an unexpectedly large rate coefficient was determined for the reaction of CH_2OO with SO_2.[8] This result could dramatically alter estimates of sulfuric acid concentrations and aerosol formation rates in the atmosphere.[21]

Most work has focused on the 'simplest' Criegee intermediate CH_2OO. Only a handful of studies have investigated other carbonyl oxides such as CH_3CHOO, the 'next simplest' Criegee intermediate. Taatjes *et al.* probed the *syn* and *anti* conformers of CH_3CHOO with PIMS and estimated the relative thermal population of the *syn* conformer over the *anti* conformer to be 90:10 at 298 K, assuming similar photoionization cross sections for both conformers. They also determined conformer-specific rate constants for reaction with SO_2 and H_2O.[22] Beames *et al.* measured the UV absorption spectrum of CH_3CHOO by laser depletion of the ground electronic state, which was detected with PIMS at 10.5 eV.[23]

Direct measurement of the UV absorption spectrum of CH_3CHOO has not been reported. Furthermore, considerable discrepancies in the reported UV spectra of CH_2OO[11-13] suggest that additional studies may also be necessary for CH_3CHOO. In this work, the UV absorption spectrum of CH_3CHOO is measured by transient absorption spectroscopy, and is scaled to the absolute absorption cross section at 308 nm measured by laser depletion in a molecular beam.

2.2 Methods

2.2.1 Transient absorption spectroscopy

The transient absorption measurements of CH_3CHOO were carried out in a flow apparatus.[13, 24] A schematic of the apparatus is shown in Figure 2.1. For CH_3CHOO absorption experiments, a mixture of O_2 and N_2 was bubbled through liquid CH_3CHI_2 (Aldrich, ≥98.0%). The CH_3CHI_2 liquid was slightly heated (311 K) to ensure saturation of its vapor above the liquid, resulting in a stable concentration of CH_3CHI_2 in the gas flow. For SO_2 scavenging experiments, SO_2 (99.98%) was also introduced from a cylinder maintained at 273 K to achieve a low vapor pressure for easier flow control. The mixing ratio of each gas (CH_3CHI_2, O_2, N_2 and SO_2) was controlled by four mass flow controllers (Brooks Instruments, 5850E). A fifth mass flow controller was used to maintain a small flow of the N_2/O_2 carrier gas (1–2% of the total N_2/O_2 flow rate) near the photolysis cell windows to avoid contamination. All gases were mixed in Teflon tubes and passed through a smaller cell (201 mm long) upstream of the photolysis cell. The absorption of CH_3CHI_2 and SO_2 in this small cell was monitored continuously throughout the experiment with a D_2 lamp (Ocean Optics, D-2000) and a spectrometer (Ocean Optics, USB2000+UV-VIS-ES).

Transient absorption in the photolysis cell (750 mm long, 20 mm inner diameter) was detected with a continuous light source (Energetiq, EQ-99) and a gated iCCD spectrometer (Spectrometer: Andor SR303i; iCCD: Andor iStar DH320T-18F-E3). The wavelength scale of the spectrometer was calibrated with the emission spectrum from a mercury lamp (1.5 nm resolution, calibration accuracy 0.25 nm) before each experiment. The pressure and flow rate in the photolysis cell were controlled with the mass flow controllers and an outlet valve to a mechanical pump. A linear flow velocity faster than 0.8 m/s was maintained to allow complete refreshment of gases between laser pulses (1 Hz repetition rate).

CH_3CHOO was produced from photolysis of CH_3CHI_2 by a 248 nm KrF excimer laser (Coherent Compex Pro 205 F) and subsequent reaction of CH_3CHI with O_2. The change in absorption by CH_3CHOO and other species was measured at a series of delay times (16 or 18 delay times total, ranging from 1 to 484 μs) between the laser pulse and the center of the iCCD spectrometer gate opening (gate width 1 μs). In addition, one reference spectrum was recorded before the photolysis laser pulse. The delay sequence was controlled automatically by a program written in Andor Basic within the iCCD spectrometer data acquisition software (Andor Solis). Signal at each delay time was accumulated over at least 120 laser pulses for each set of experimental conditions to improve the signal-to-noise ratio.

2.2.2 Absolute cross section measured by photodepletion in a molecular beam

The absolute absorption cross sections of CH_3CHOO at 308 and 352 nm were determined from laser depletion of CH_3CHOO in a molecular beam. A mixture of 20% O_2 in Ar was bubbled through liquid CH_3CHI_2. The CH_3CHI_2/O_2/Ar mixture flowed through a pulsed valve operating at 50 Hz (with a typical backing pressure of 30 psia) and entered a SiO_2 capillary (1 mm inner diameter, 20 mm length) attached to the pulsed valve nozzle. An excimer laser (XeCl or XeF, Lambda Physik, LPX-210i) with a pulse rate of 50 Hz (308 nm for the 352 nm depletion measurements, 352 nm for the 308 nm measurements) was used to photolyze CH_3CHI_2 in the SiO_2 capillary. The resulting CH_3CHI in the capillary reacted with O_2 to form CH_3CHOO. The mixture gas then expanded at the exit of the SiO_2 capillary. After passing through a skimmer (4

mm diameter) 45 cm downstream of the SiO_2 capillary, the molecular beam was further defined with a slit (0.5 mm height, 4 mm width).

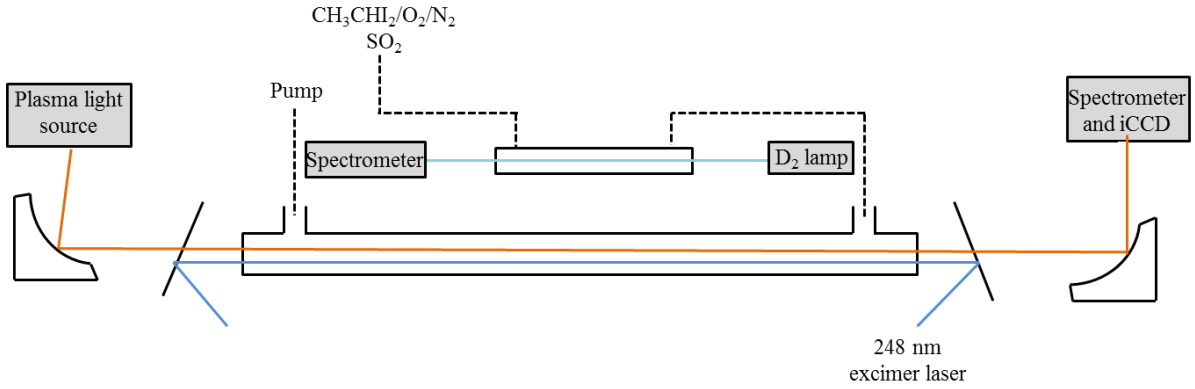

Figure 2.1. Schematic view of the transient absorption experimental setup (not to scale). Gases (CH_3CHI_2, SO_2, O_2, N_2) flow through a small absorption cell and a larger photolysis cell before exiting to the pump. Absorption in the small cell is monitored continuously by a D_2 lamp and a UV-Vis spectrometer. A 248 nm excimer laser is directed into and out of the photolysis cell by long-pass edge-filters (Semrock, LP02-257RU-25). Absorption at various delay times after the photolysis pulse is measured with a continuous plasma light source (EQ99) which is reflected through the cell and into the iCCD detector with parabolic mirrors (Newport, 50329AL and 50338AL, f = 50.8 mm and 101.6 mm).

The molecular beam signal was detected with a mass spectrometer located 75 cm downstream of the SiO_2 capillary. CH_3CHOO molecules were ionized by electron impact at 45 eV, and the ions traveled through a quadrupole mass filter to a Daly detector. Arrival time profiles of CH_3CHOO (at m/z = 60, $C_2H_4O_2^+$) were recorded using a multichannel scaler (Ortec, Turbo-MCS).

Another excimer laser beam operating at 25 Hz (at either 352 nm or 308 nm) intersected the CH_3CHOO molecular beam directly after it passed the defining slit at a point 25 cm upstream of the mass spectrometer, resulting in depletion of the signal at m/z = 60. The laser beam was attenuated homogeneously by a variable attenuator (Laseroptik, IVA351nm or IVA308nm) to the desired pulse energy, which was measured with a power meter (Gentec-EO, UP25N + Solo 2 controller).

Under the molecular beam conditions in these experiments, the photodepletion signal can be related to the absorption cross section σ, the photodissociation quantum yield ϕ, and the laser fluence I using equation (1), where N_0 and N are the numbers of molecules before and after laser irradiation.

(1) $$\frac{N}{N_0} = e^{-I\sigma\phi}, \quad \frac{\Delta N}{N_0} = \frac{N_0 - N}{N_0} = 1 - e^{-I\sigma\phi}$$

Absorption at the wavelengths studied here excites CH_3CHOO and CH_3CHI_2 to repulsive states or states higher than their dissociation thresholds,[23] resulting in rapid and complete dissociation ($\phi = 1$). Because of inhomogeneity in the laser beam profile, however, the absolute laser fluence I may be difficult to quantify with sufficient accuracy to yield accurate cross sections σ for CH_3CHOO using equation (1). Two additional methods of determining absolute CH_3CHOO cross sections were therefore used.

First, in addition to measuring the depletion of CH_3CHOO, the relative depletion of CH_3CHI_2 at 308 nm was measured in the molecular beam. By analyzing the experimental data with equation (1), the value of $I\sigma$ was obtained for both CH_3CHOO and CH_3CHI_2, assuming $\phi = 1$. Then, the ratio of $\sigma(CH_3CHOO)/\sigma(CH_3CHI_2)$ can be deduced. As discussed later, if $\sigma(CH_3CHI_2)$ is known and reliable, the absolute value of $\sigma(CH_3CHOO)$ can be obtained.

Second, a method was developed to estimate the absolute fluence of the excimer laser beam. The profile of the laser beam was recorded using a laser beam profiling digital camera (WinCamD, model UCD23, 8.8 mm x 6.6 mm image area, 6.45 μm x 6.45 μm pixel area, 14-bit ADC) and DataRay imaging software. A rectangular slit (2 mm high, 19 mm wide) in the laser beam path, 15 mm ahead of the laser beam-molecular beam crossing point, removed the "wings" of the laser beam vertical profile so that only the most intense and uniform portion of the laser beam was used. Using the measured laser pulse energy and the intensity profile, the absolute laser fluence can be deduced. This method was used to obtain absolute cross section values at 352 nm for both CH_3CHOO and CH_2OO.

2.3 Results and discussion

2.3.1 Transient absorption

Figure 2.2 (top) shows examples of transient absorption measured at different photolysis delay times. Depletion of the broad CH_3CHI_2 absorption peaked at 290 nm by photolysis as in (R2) is clearly visible, and absorption of CH_3CHOO (the peak labeled as band A) appears in the first few μs due to (R3) and decreases as the delay time is increased. Formation of IO produced by (R4), with its distinct vibrational peaks at 412, 420, 428, and 436 nm, can also be seen at longer delay times. Absorption spectra[25] for CH_3CHI_2 and IO are shown in Appendix 2A.

(R2) $CH_3CHI_2 + h\nu \rightarrow CH_3CHI + I$

(R3) $CH_3CHI + O_2 \rightarrow CH_3CHOO + I$

(R4) $CH_3CHOO + I \rightarrow CH_3CHO + IO$

(R5) $CH_3CHOO + SO_2 \rightarrow$ products

(R6) $CH_3CHOO + CH_3CHOO \rightarrow$ products

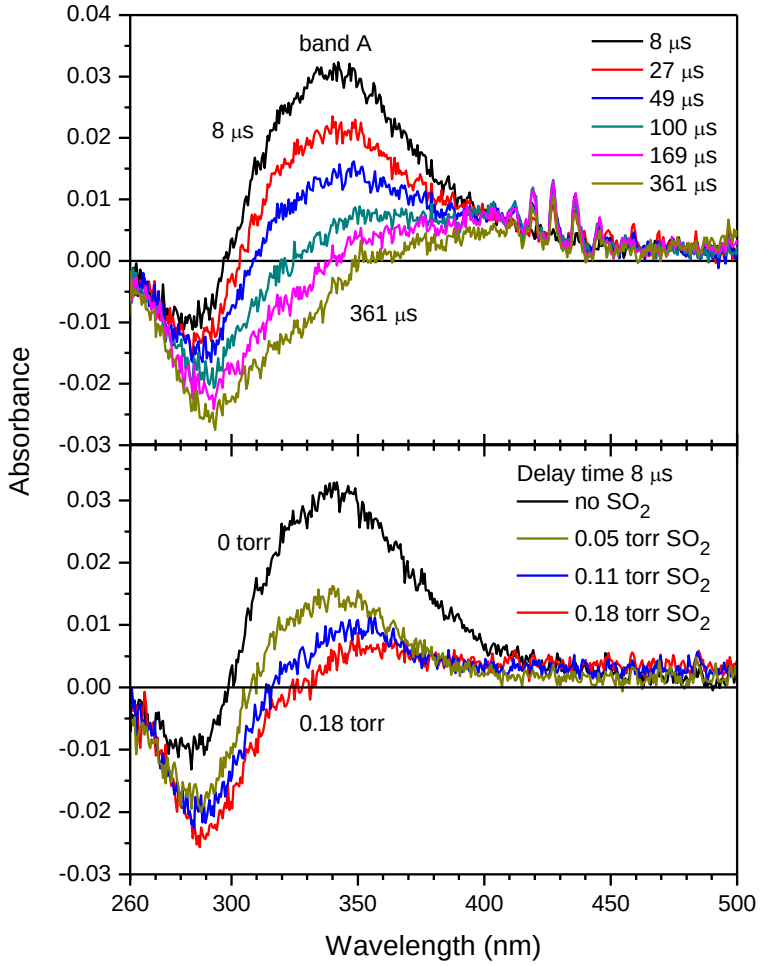

Figure 2.2. Top: Examples of transient absorbance traces probed at different delay times after the photolysis pulse, with no SO_2 present. Depletion of CH_3CHI_2 results in the negative absorbance peaked near 290 nm. Formation of IO gives rise to distinct peaks at 412, 420, 428, and 436 nm at longer delay times. Absorption of CH_3CHOO, with peak labeled band A, decreases with increasing delay time. Number densities in the cell are $[CH_3CHI_2]_0 = 1.2\times10^{16}$ cm^{-3}, $[O_2]_0 = 9.7\times10^{17}$ cm^{-3}, total number density (N_2 balance) 2.1×10^{18} cm^{-3}. Bottom: Examples of absorbance traces at a delay time of 8 μs at different SO_2 concentrations. $[CH_3CHI_2]_0 = 1.3\times10^{16}$ cm^{-3}, $[O_2]_0 = 1.0\times10^{18}$ cm^{-3}, total number density 2.1×10^{18} cm^{-3}.

The fast rate of (R5) ($2.4–6.7\times10^{-11}$ cm^3 $molecule^{-1}$ s^{-1} reported by Taatjes *et al.*)[22] allows SO_2 to be used as an efficient scavenger for CH_3CHOO. Figure 2.2 (bottom) shows absorbance traces for different concentrations of SO_2 scavenger. The rapid depletion in absorbance upon addition of SO_2 is expected to originate solely from CH_3CHOO depletion (since the absorption change due to other species consumed or produced, such as SO_2, CH_3CHO, and SO_3, is much weaker). When all experimental conditions except the SO_2 concentrations are kept constant, subtracting the absorbance in the presence of SO_2 from the absorbance without SO_2 yields an absorption spectrum containing contributions from CH_3CHOO and SO_2 at a 1:1 ratio.[13] After

scaling the UV absorption spectrum to the absolute cross sections obtained by laser depletion (discussed below), the contribution of SO_2 absorption to the spectrum can be easily removed.

As shown in Figure 2.3, the SO_2 scavenging experiments allowed the measurement of the decay rate of CH_3CHOO in the presence of SO_2 under pseudo first-order conditions. We determined the rate constant for (R5) to be $(2.0\pm0.3)\times10^{-11}$ cm^3 molecule^{-1} s^{-1}, which agrees with a value of $(2.4\pm0.3)\times10^{-11}$ cm^3 molecule^{-1} s^{-1} reported for the dominant *syn* conformer of CH_3CHOO.[22] Under the experimental conditions in this work, we did not observe the kinetics of the *anti* conformer, which is reasonable if its thermal population is only 10%.[22] The *anti* conformer was reported to react with SO_2 at a faster rate of $(6.7\pm1.0)\times10^{-11}$ cm^3 molecule^{-1} s^{-1}.[22]

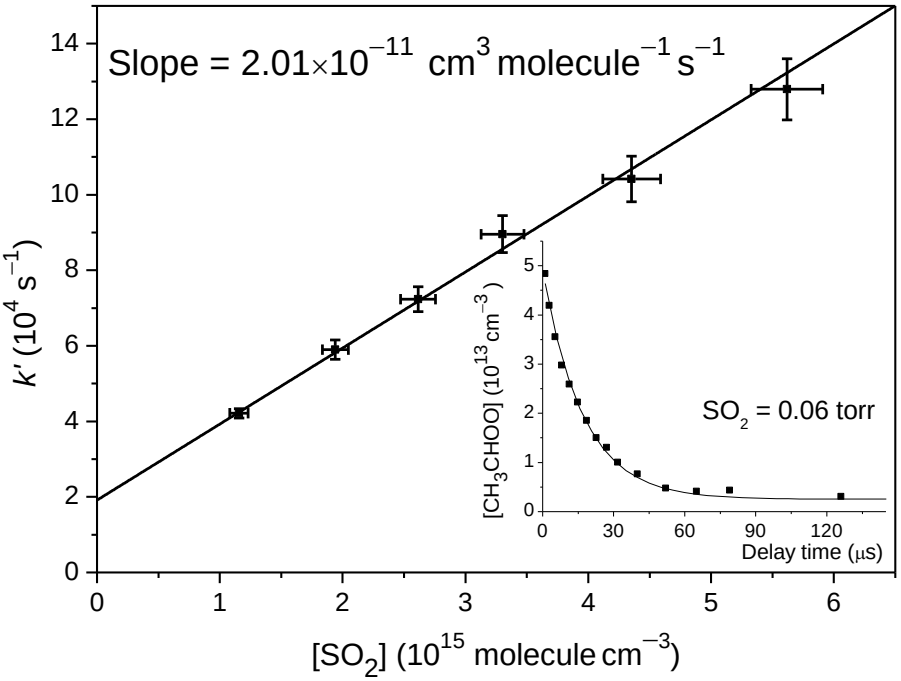

Figure 2.3. Pseudo-first order rate constant *k'* as a function of SO_2 concentration for the decay of CH_3CHOO. The slope of the linear fit represents the second-order rate constant for reaction of CH_3CHOO with SO_2. Inset: Exponential decay fit to the CH_3CHOO number density calculated from the measured absorbance at different kinetic (delay) times.

Without SO_2 in the photolysis cell, decay of CH_3CHOO is due primarily to (R6), the self-reaction of the Criegee intermediate, and to (R4). Figure 2.4 shows simulated absorption profiles at short and long delay times, containing contributions from CH_3CHOO as well as CH_3CHI_2 and IO (see Appendix 2A for the absorption spectra of CH_3CHI_2, IO, and other relevant species). Because (i) CH_3CHI is consumed by excess O_2 within the first few μs, (ii) CH_3CHOO is relatively short-lived in comparison with CH_3CHI_2 and IO, and (iii) the shapes of the CH_3CHI_2 and IO spectra are quite distinct, the contributions of CH_3CHI_2 and IO to the

absorbance can be easily subtracted. The resulting spectrum is consistent with the spectrum obtained using SO_2 scavenger (see Figure 2.5), although slight discrepancies at wavelengths longer than 400 nm suggest contributions from other absorbing species (possibly CH_3CHIOO, an adduct of CH_3CHI and O_2). The SO_2 scavenging method used in this work to extract the CH_3CHOO spectrum provides species selectivity based on the chemical reactivity of CH_3CHOO. The "self-reaction" method has somewhat lower selectivity. Hence, small discrepancies between the SO_2-scavenging spectrum and the self-reaction spectrum in Figure 2.5 should originate from contaminants that have weaker absorption.

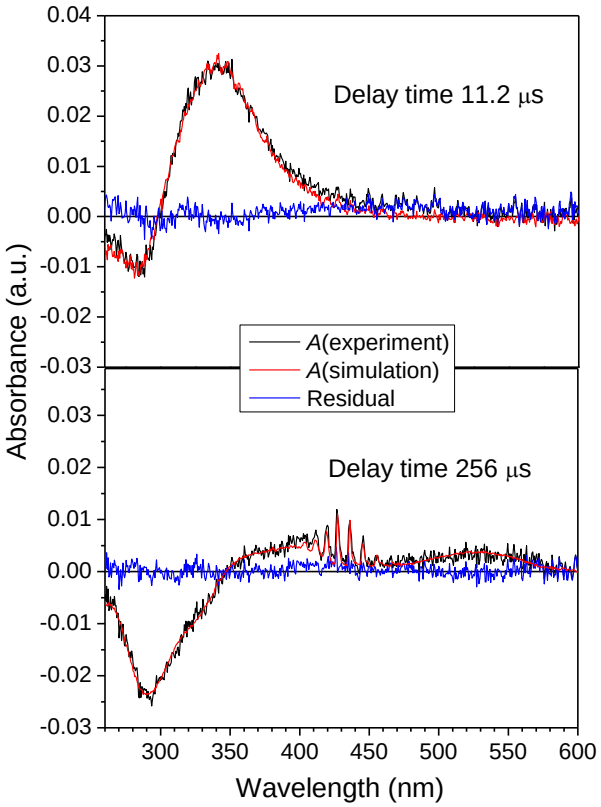

Figure 2.4. Experimental and simulated absorbance (A) spectra at short and long delay times (no SO_2). The depletion of CH_3CHI_2 causes negative absorbance peaked at 290 nm. Absorption from I_2 appears at longer delay times, after CH_3CHOO is mostly depleted, and therefore it should not significantly affect determination of the CH_3CHOO spectrum. Calculated number densities of the depleted CH_3CHI_2 and of CH_3CHOO, IO, and I_2 are 1.24×10^{14}, 4.81×10^{13}, 2.05×10^{12}, 5.70×10^{5} cm^{-3}, respectively, at 11.2 μs, and 1.08×10^{14}, 5.55×10^{12}, 8.39×10^{12}, 1.73×10^{13} cm^{-3}, respectively, at 256 μs.

The absorption spectrum of CH_3CHOO was determined under a variety of conditions utilizing CH_3CHOO decay from SO_2 scavenging and from CH_3CHOO self-reaction, including variations in cell pressure (15-100 Torr), O_2 concentration (15-45 Torr), SO_2 concentration (0-0.18 Torr),

photolysis laser power (44-88 mJ), and the delay time between CH_3CHI_2 photolysis and the absorption measurement (8-49 μs). Appendix 2B shows the averaged results of all CH_3CHOO spectra obtained from both methods. No significant difference in the shape of the resulting CH_3CHOO spectra was observed upon varying these conditions, which strongly suggests that no other species besides CH_3CHOO contributes significantly to the spectra obtained with these two methods. The higher baseline (as well as some small peaks in the 440–500 nm range) of the self-reaction spectrum may be due to small contributions of other species to the transient absorption measurements, such as CH_3CHIOO. However, the main absorbing region of CH_3CHOO from 260–400 nm does not appear to be significantly affected by these contributions.

2.3.2 Laser depletion of CH_3CHOO in a molecular beam

While the absorbance due to CH_3CHOO can be extracted from the transient absorption, it is difficult to know the absolute number density of CH_3CHOO in the photolysis cell. Therefore, to convert the spectrum of CH_3CHOO to absorption cross sections, the absolute cross sections at 308 nm and 352 nm were measured by mass spectrometric detection of the laser depletion of CH_3CHOO in a molecular beam. This method has been used previously to selectively detect species with short lifetimes and at low concentrations.[13,26,27] Figure 2.6 (top solid symbols) shows the CH_3CHOO depletion signal ($\Delta N/N_0$) at 308 nm at a variety of laser pulse energies, and the fit to Equation (1). The good fit indicates that a single species is being measured (or multiple species that have similar cross sections). At high laser energy the CH_3CHOO signal approaches 100% depletion, consistent with $\phi = 1$. The relative depletion of CH_3CHI_2 was also measured under similar conditions, shown in Figure 2.6 (top open symbols) with the fit to equation (1). Saturation of the CH_3CHOO depletion signal occurs at a lower laser pulse energy than that of CH_3CHI_2, indicating the cross section of CH_3CHOO is larger.

Because the temperature in a molecular beam (e.g., $T_{rot} \approx 10$ K) is much lower than room temperature, one must consider the effect of temperature on the absorption cross section. 308 nm is near the peak of the CH_3CHI_2 UV absorption band[25] and is therefore likely to have a negligible temperature dependence, as observed for CH_2I_2.[25,28] Assuming the low temperature cross section at 308 nm is the same as that at 298 K for CH_3CHI_2, one may use the laser depletion of CH_3CHI_2 to calibrate the laser fluence. In other words, since the relative laser fluence is known for both the CH_3CHOO and CH_3CHI_2 experiments, the cross section ratio of $\sigma(CH_3CHOO)/\sigma(CH_3CHI_2)$ can be deduced, and subsequently, $\sigma(CH_3CHOO)$ based on the literature value of $\sigma(CH_3CHI_2)$ at 298 K. (The uncertainty in $\sigma(CH_3CHI_2)$ was estimated by assuming its fractional error is similar in magnitude to the error in $\sigma(CH_2I_2)$ reported by the same work.[25,29] This work reported a peak cross section of CH_2I_2 that is 7% higher than the corresponding JPL recommended value.)

However, the unknown temperature effect at 352 nm, which is on the weak tail of the CH_3CHI_2 UV absorption band, may introduce error. This complication was circumvented by measuring the absolute laser fluence I directly, as discussed above. Figure 2.6 (bottom) shows the CH_3CHOO depletion at different laser fluences and the fit to Equation (1), from which $\sigma(CH_3CHOO)$ can be determined. In order to compare the CH_3CHOO cross section results from the two methods (i.e., the CH_3CHI_2 reference and the absolute laser fluence methods), the laser intensity profile at 308 nm was also measured and used to determine the absolute CH_3CHOO cross section.

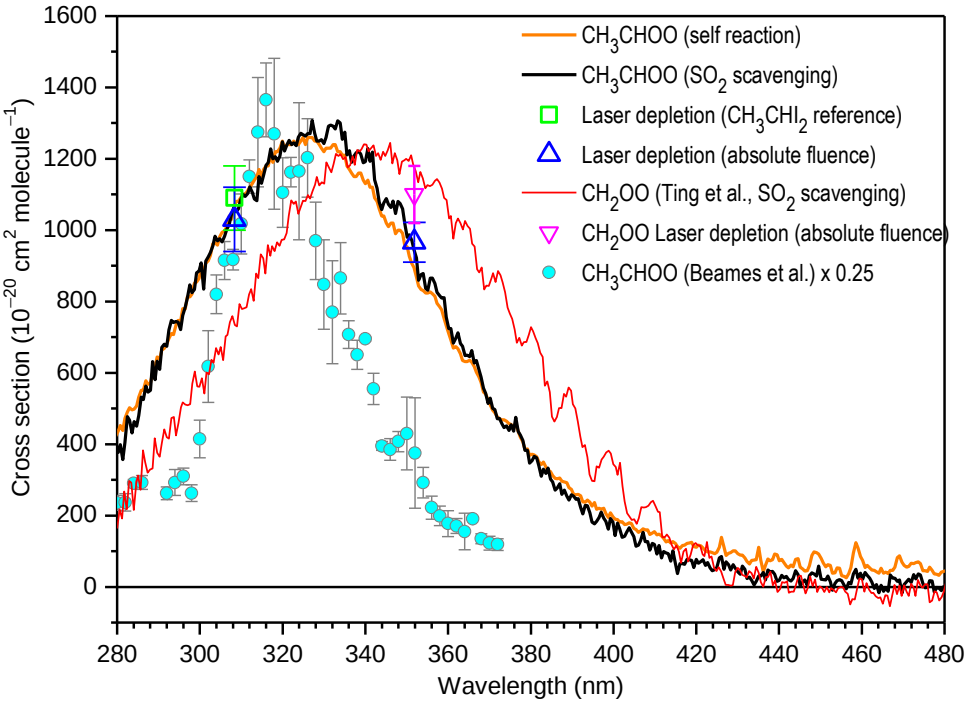

Figure 2.5. Comparison of CH_3CHOO and CH_2OO absorption spectra. Black and orange lines are the CH_3CHOO spectra obtained here using the SO_2 scavenger and self-reaction methods. Square and triangle symbols indicate cross section measurements from laser depletion. Blue filled circles are the CH_3CHOO absorption measurements of Beames *et al.*,[23] scaled by a factor of 0.25 to roughly match the absolute absorption cross section at 308 nm measured in this work. The thin red line is the spectrum of CH_2OO measured by Ting *et al.*[13]

The absorption cross sections of CH_3CHOO at both 308 nm and 352 nm are near the maximum CH_3CHOO absorption at 328 nm. In the case of CH_2OO, UV absorption arises from the B ← X transition analogous to the Hartley band of O_3, which has weak or no temperature dependence near its absorption maximum.[13,25,30] It can thus be expected that the cross section of CH_3CHI_2 at wavelengths near the absorption maximum at 328 nm (such as at 308 nm) should not be affected by temperature, as has been found for CH_2I_2.[25,28] The known CH_3CHI_2 absorption cross section at 298 K[25] can therefore be used as a reference to calculate the CH_3CHOO absorption cross section at 308 nm in the molecular beam (with a rotational temperature of ~10 K), which should not differ greatly from its value at 298 K given the arguments above.

In contrast, 352 nm is far from the peak of the CH_3CHI_2 absorption band. If the temperature dependence of the CH_3CHI_2 absorption cross section in this region of the spectrum is significant, as is the case for CH_2I_2, then the CH_3CHI_2 cross section at 298 K may differ from that under the low temperatures in a molecular beam. For 352 nm, then, using the reported room temperature CH_3CHI_2 absorption cross section as a reference may introduce error into the cross section determination for CH_3CHOO, so a method was developed instead to estimate the absolute fluence of the excimer laser.

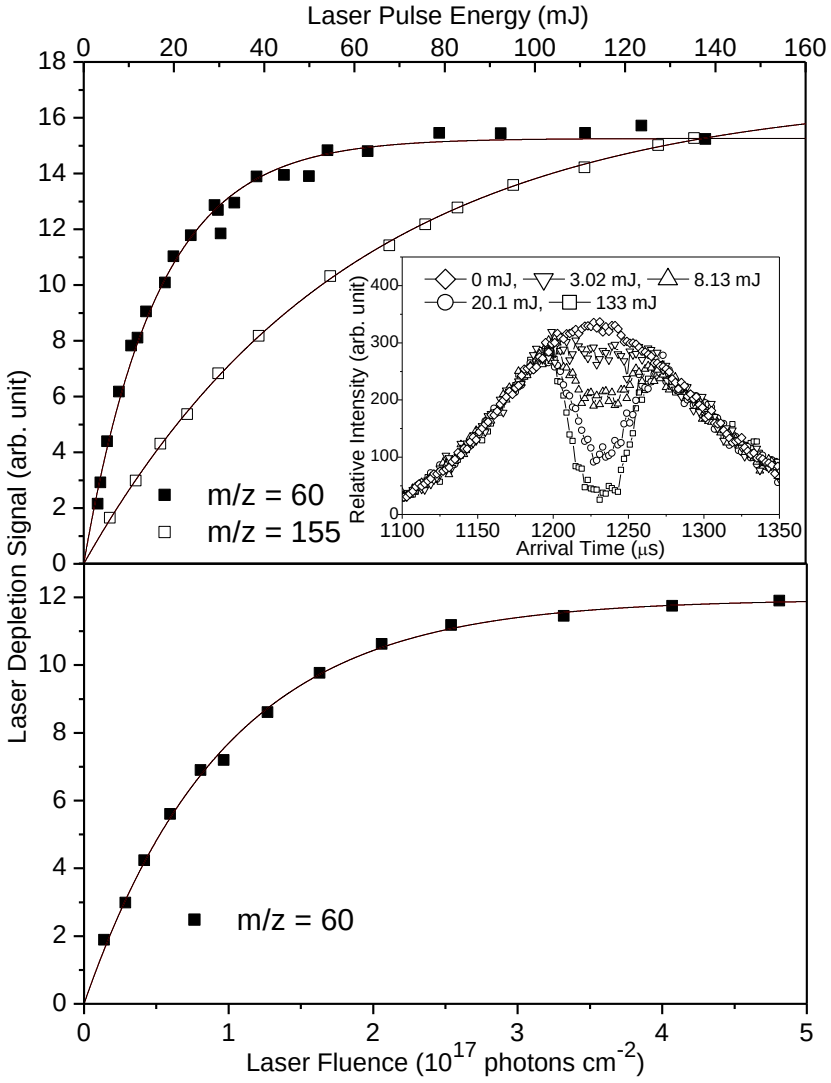

Figure 2.6. Top: Saturation curves for laser depletion of CH_3CHOO (*m/z* = 60) and CH_3CHI_2 (*m/z* = 155, CH_3CHI^+, a daughter ion of CH_3CHI_2) at 308.4 nm. The x-axis is the laser pulse energy, which is proportional to the laser fluence. The lines are fits to equation (1). Top inset: Arrival time profiles of CH_3CHOO at different laser fluences at 308.4 nm. Bottom: Saturation curve for laser depletion of CH_3CHOO (*m/z* = 60) at 351.8 nm. The x-axis is the absolute laser fluence, deduced from the laser pulse energy and the measured laser beam profile. The line is the fit to equation (1).

Appendix 2C shows a schematic representation of the fluence measurement procedure. In brief, a slit was placed in the path of the depletion laser, and the resulting laser beam intensity profile was measured using a digital camera. Images of the beam profile before and after the addition of the slit are shown in Figure 2.7.

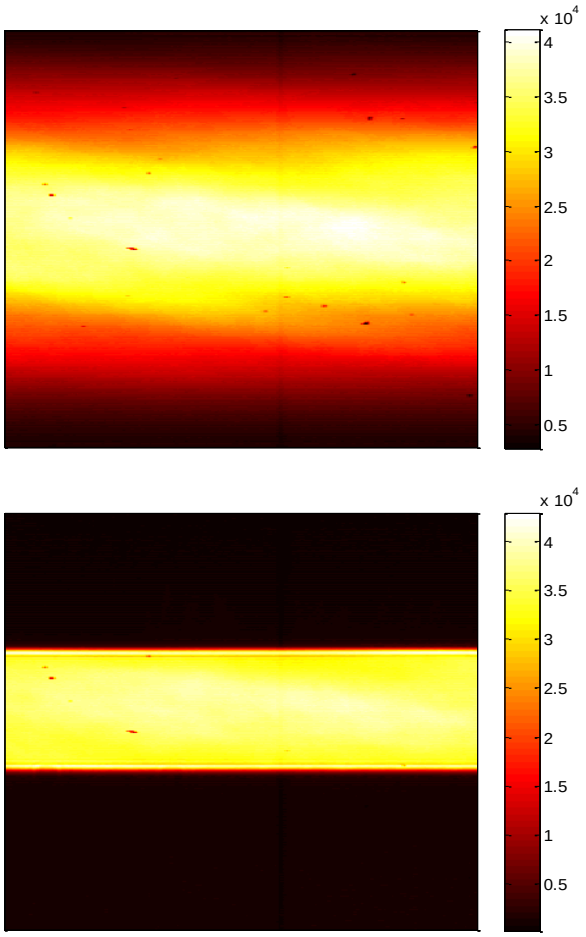

Figure 2.7. Two-dimensional laser beam profiles. The scale on the color bars refers to the ADC value from the digital camera. Both profiles were obtained outside the molecular beam chamber at a location corresponding to point X in Appendix 2C. Top: Beam profile without slit. Bottom: Beam profile with slit.

Equation (2) was used to convert the laser pulse energy measured outside the chamber exit, E_{out}, to the effective pulse energy experienced by the molecular beam, E_{eff}.

(2) $$E_{eff} = \frac{\int_{y_3}^{y_4} S(y)dy}{\int_{y_1}^{y_2} S(y)dy} \frac{1}{T_{exit}} E_{out}$$

In equation (2), T_{exit} is the transmittance of the chamber exit window (92.0%), $S(y)$ is the ADC signal from the camera at vertical position y, the integration limits y_1 and y_2 contain the entire laser beam profile, and the integration limits y_3 and y_4 contain the approximate laser beam-molecular beam overlap region ($y_3 - y_4 = 0.50$ mm) (see Figure 2.8). The absolute laser fluence, I, was calculated using equation (3).

(3) $$I = \frac{E_{eff}\left(\frac{hc}{\lambda}\right)^{-1}}{A_{overlap}}$$

In equation (3), λ is the average wavelength of the laser (351.8 nm) and $A_{overlap}$ is the area of the laser-molecular beam overlap region (19.0 mm x 0.5 mm). An example calculation is shown in Table 2.1.

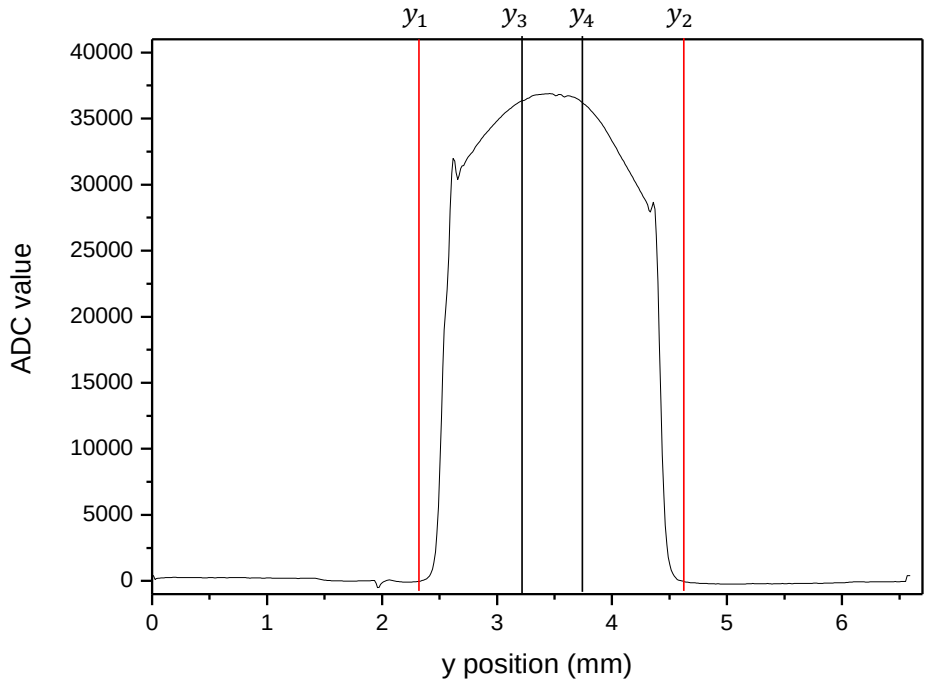

Figure 2.8. Vertical profile of the laser beam (averaged over the horizontal axis). The red vertical lines (y_1 and y_2) indicate the range of integration over the laser beam profile, and the black vertical lines (y_3 and y_4) indicate the range of integration over the laser beam-molecular beam overlap region.

Table 2.1. Example of a laser fluence calculation.

E_{out} (mJ)	T_{exit}	$\frac{\int_{y_3}^{y_4} S(y)dy}{\int_{y_1}^{y_2} S(y)dy}^{a}$	E_{eff} (mJ)	λ (nm)	$A_{overlap}$ (cm^2)	I (photons cm^{-2})
82.94±2.00	92.8±1.5%	$0.291^{+0.002}_{-0.014}$	25.96±1.53	351.8	0.0956	4.81±0.28×10^{17}

[a]The stated error represents uncertainty in the slit-focusing lens distance, the slit-molecular beam distance, and the positions of y_3 and y_4 integration limits.

For comparison of this method with the reference method, measurements of the laser beam profile at 308 nm were also performed using a digital CCD camera (PCO, Pixelfly VGA, 12-bit) and an analog CCD camera (Sony XC-EU50).

2.3.3 UV absorption spectrum of CH_3CHOO

Table 2.2 summarizes the laser depletion results for CH_3CHOO at 308 and 352 nm as well as for CH_2OO at 352 nm. These absolute cross sections are also plotted in Figure 2.5. The CH_3CHOO spectra obtained with the methods outlined above were scaled to the average cross section at 308 nm obtained from laser depletion. Here it is assumed that the temperature effect on the cross sections of CH_3CHOO is negligible at 308 nm. This assumption is reasonable since 308 and 352 nm are near the peak of the UV absorption band, as in the case of CH_2OO.[13] For both CH_3CHOO and CH_2OO, the scaled room-temperature cross sections at 352 nm are consistent with the absolute cross sections measured in the jet-cooled molecular beams (see Figure 2.5), further supporting the validity of the assumption that temperature has little effect near the absorption peaks. The peak cross section of CH_3CHOO is $(1.27\pm0.11)\times10^{-17}$ cm^2 $molecule^{-1}$ at 328 nm. Numerical values of the CH_3CHOO absorption cross sections can be found in Appendix 2D.

The CH_3CHOO spectra obtained in this work are compared in Figure 2.5 with the CH_2OO spectrum reported by Ting *et al.*[13] The peak wavelength of CH_3CHOO, 328 nm, is blue shifted by 14 nm from the CH_2OO peak at 342 nm. Previous theoretical calculations attributed this wavelength shift to stabilization of the ground electronic state and destabilization of the excited electronic state of the *syn* conformer of CH_3CHOO, which dominates CH_3CHOO populations over the *anti* conformer at 298 K.[23] While clear vibronic structure on the long wavelength side was observed for CH_2OO, the CH_3CHOO absorption shows similar but much weaker structure (step-like oscillation). This smearing of the vibronic structure may be expected for a molecule with more degrees of freedom.

Measurements of the CH_3CHOO spectrum by Beames *et al.*[23] are also plotted in Figure 2.5, scaled by a factor of 0.25 to roughly match the 308 nm cross section reported here for easier comparison. The discrepancies are surprising, especially since both studies used laser depletion in a molecular beam to determine the cross sections. In particular, their scaled cross section value at 352 nm is significantly smaller or, alternatively, their unscaled cross section is significantly larger than the data from 300 to 350 nm in the present work. For the earlier CH_2OO studies, the inconsistencies between the CH_2OO laser depletion data from Beames *et al.*[11] and from Ting *et al.* (who used the same apparatus and similar methods to the present work)[13] were primarily at wavelengths longer than 352 nm and might therefore be explained by a possible temperature effect around 380 nm.[13] However, such a possibility is ruled out for CH_3CHOO in this work by the use of the absolute laser fluence to determine the cross section of CH_3CHOO in the molecular beam at 352 nm directly. Differences in the methods used to quantify the laser fluence might be one possible cause of the discrepancies between this work and that of Beames *et al.*[23]

Isomer interference could also cause the observed discrepancies. Beames *et al.*[23] detected CH_3CHOO with photoionization at 10.5 eV. This method provides isomer selectivity because the ionization energies of *syn*- and *anti*-CH_3CHOO are about 9.4 and 9.3 eV, respectively[22] and other isomers have higher ionization energies.[22] In this work electron impact ionization at 45 eV was used to detect CH_3CHOO and CH_3CHI_2. Electron impact ionization at 45 eV would not discriminate isomers. To determine the potential impact of isomer interference, we compared our results with the oscillator strengths of relevant UV transitions for the possible isomers of CH_3CHOO calculated with the CCSD-EOM method (see the published version of this chapter for calculation details). The Criegee intermediates *syn*- and *anti*-CH_3CHOO absorb very

strongly in the near UV range, while other isomers like acetic acid, dioxirane, bisoxy, etc. absorb rather weakly or at much shorter wavelengths. Hence, it is unlikely that isomer absorption contributes significantly to the spectrum.

Table 2.2. Absolute absorption cross sections of CH_3CHOO and CH_2OO measured by laser depletion in a jet-cooled molecular beam.

Molecule	Wavelength (nm)	Method	Cross Section (cm^2)
CH_3CHOO	308.4	CH_3CHI_2 reference	$(10.9^{a}\pm0.9^{b})\times10^{-18}$
		Absolute laser fluence	$(10.3\pm0.9^{b})\times10^{-18}$
	351.8	Absolute laser fluence	$(9.7\pm0.6^{b})\times10^{-18}$
CH_2OO	351.8	Absolute laser fluence	$(11.0\pm0.8^{b})\times10^{-18}$

[a] Calculated using the measured value of 3.85±0.19 for the ratio $\sigma\phi(CH_3CHOO)/\sigma\phi(CH_3CHI_2)$ and $\sigma(CH_3CHI_2) = (2.83\pm0.20)\times10^{-18}$ cm^2 $molecule^{-1}$;[25] $\phi(CH_3CHI_2)$ and $\phi(CH_3CHOO)$ are assumed to be unity. See Section 2.3.2 for error estimation. [b] 1σ uncertainty.

While the results from our experimental methods are consistent with each other, there are subtle differences between the absorption of CH_3CHOO at room temperature and in a jet-cooled molecular beam. Theoretical calculations show that the *anti* form of CH_3CHOO is less stable than the *syn* form and absorbs at longer wavelengths (specifically, the peak of *anti*-CH_3CHOO is red-shifted by 15 nm relative to *syn*-CH_3CHOO).[23] As stated earlier, Taatjes *et al.*[22] estimated the relative thermal population of the *syn* conformer over the *anti* conformer to be 90:10 at 298 K by assuming similar photoionization cross sections for both conformers. Therefore, the room-temperature spectrum of CH_3CHOO would consist mainly of the contribution of the *syn* conformer with only a minor contribution from the *anti* conformer. In the jet-cooled molecular beam of CH_3CHOO, it might be expected that the *anti* conformer has an even smaller population than in room temperature CH_3CHOO. However, the barrier to interconversion of these conformers is about 38 kcal mol^{-1}.[31] Because of this high barrier, the rapid cooling process in the supersonic expansion may not reach thermal equilibrium, resulting in similar conformer populations as before expansion.

In addition, CH_3CHOO has low frequency vibrational modes which could be effectively cooled by the supersonic expansion in a molecular beam. As a result, there would be more hot bands in a room-temperature spectrum than in a jet-cooled spectrum. This may partly explain the longer wavelength tail in the UV spectrum at 295 K in this work as compared to the jet-cooled spectrum reported by Beames *et al.*[23]

2.3.4 Implications for atmospheric chemistry

With regard to the role of CH_3CHOO in atmospheric photochemistry, we estimated its photolysis rates (*J*-values) based on the absorption spectrum obtained in this work and the reported solar flux.[32] The *J*-value (*i.e.*, the first-order rate coefficient for photolysis) can be calculated using equation (4), in which (λ) is the absorption cross section, (λ) is the quantum yield, and $F(\lambda)$ is the solar (or actinic) flux.

(4) $$J = \int_{\lambda_i}^{\lambda_f} \sigma(\lambda)\Phi(\lambda)F(\lambda)d\lambda$$

The photolysis lifetime is the reciprocal of the *J*-value. Estimated photolysis lifetimes for CH_2OO and CH_3CHOO are shown in Table 2.3. The values in Table 2.3 were calculated assuming $\Phi(\lambda)$=1 and using the actinic flux values, $F(\lambda)$, at Earth's surface given in Ref 32 and plotted in Figure 2.9. The same method and values for $F(\lambda)$ yielded a *J*-value for the photolysis of formaldehyde to molecular hydrogen ($CH_2O + h\nu \rightarrow H_2 + CO$) of 4.57×10^{-5} s^{-1} (SZA = 0°), consistent with a recommended value of 4.79×10^{-5} s^{-1}.[25,33] The solar flux from Ref. 32 is consistent with that from NCAR Tropospheric Ultraviolet and Visible (TUV) Calculator (available at http://cprm.acd.ucar.edu/Models/TUV/Interactive_TUV/). Using the published cross sections[25] of Cl_2 and the solar flux from the TUV calculator at a solar zenith angle of 0 degree, the calculation yields a *J*-value of 2.19×10^{-3} s^{-1}, consistent with the value of 2.17×10^{-3} s^{-1} directly given by the TUV calculator.

Figure 2.9 compares the cross section spectra for CH_2OO and CH_3CHOO with the solar actinic flux and with the spectra reported by Beames *et al.*[11,23] The maximum cross section for CH_3CHOO of 1.27×10^{-17} cm^2 is similar to that for CH_2OO (1.23×10^{-17} cm^2 reported by Ting *et al.*).[13] However, the blue shift of the CH_3CHOO spectrum reduces overlap with the solar flux at the Earth's surface. A comparison of photolysis lifetimes in Table 2.3 shows that a somewhat longer photolysis lifetime is expected for CH_3CHOO relative to CH_2OO (7.24 and 6.07 seconds, respectively, at a solar zenith angle of 0°; 169 and 132 seconds respectively at zenith angle 86°).

Table 2.3. Photolysis lifetimes of CH_2OO and CH_3CHOO calculated from previously reported UV absorption cross sections and from this work.

SZA (degrees)	Photolysis Lifetime (seconds)[a]			
	CH_2OO (Ting *et al.*)[b]	CH_3CHOO (this work)	CH_2OO (Beames *et al.*)[c]	CH_3CHOO (Beames *et al.*)[d]
0	6.07	7.24	2.45	4.73
30	6.61	7.95	3.30	5.33
60	10.6	13.1	5.67	9.77
86	132	169	77.7	154

SZA = Solar zenith angle. [a] Calculated using solar actinic flux values at Earth's surface from Table 3.7 of Ref. 32 and using equation (4). [b] Ref. 13. [c] Ref. 11. [d] Ref. 23.

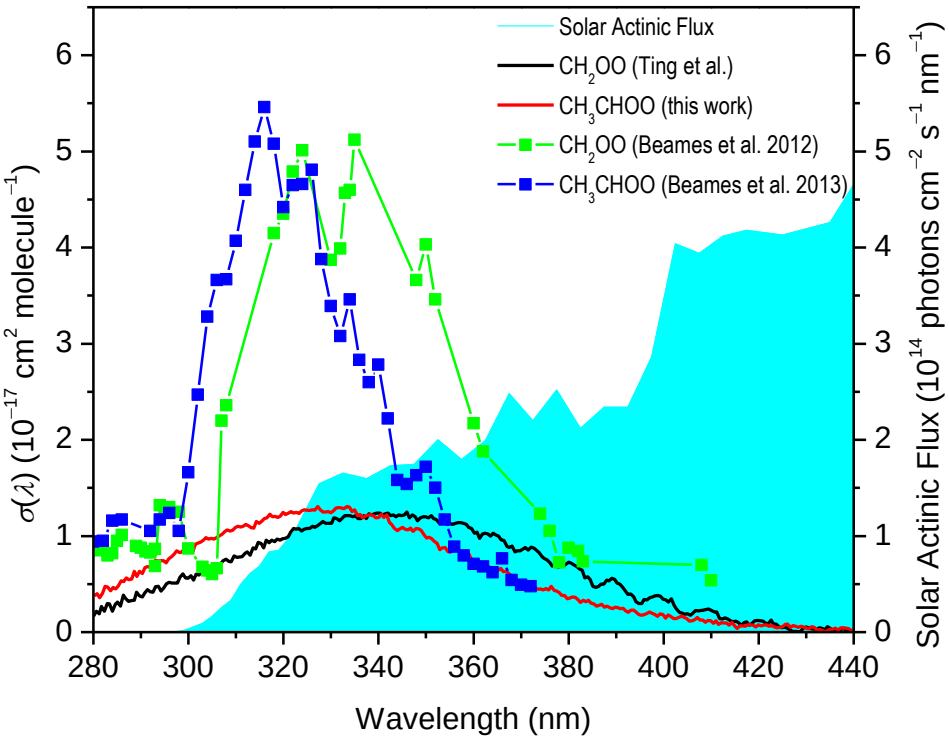

Figure 2.9. Absorption cross sections, $\sigma(\lambda)$, for CH_2OO and CH_3CHOO from this work and others[11,13,23] compared with the solar actinic flux, $F(\lambda)$, at the Earth's surface for a solar zenith angle of 0°.[32]

2.4 Conclusion

The CH_3CHOO UV absorption spectrum was measured by transient absorption spectroscopy and absolute absorption cross sections were determined at 308 and 352 nm by laser depletion. In the transient absorption measurements, SO_2 scavenging and self-reaction of CH_3CHOO were used to extract the spectrum of CH_3CHOO. In the laser depletion experiments, two methods were used to calibrate the laser fluence: CH_3CHI_2 as a reference molecule and a laser beam profiler measurement. The cross sections presented here may facilitate analysis of the impact of CH_3CHOO photolysis in the atmosphere, and may also provide a useful spectral signature for detection of this Criegee intermediate in laboratory investigations.

Appendix 2A. Absorption spectra of CH_3CHI_2/IO/CH_3CHI/I_2

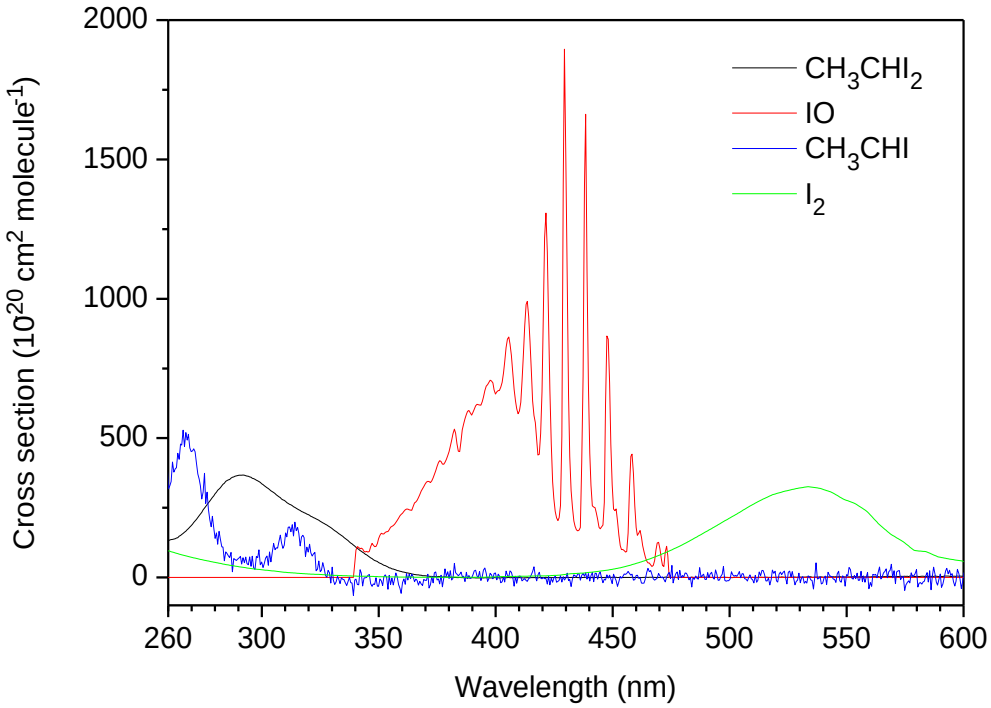

Figure 2A.1. Absorption cross sections of CH_3CHI_2, IO, CH_3CHI, and I_2. The CH_3CHI spectrum was obtained from the transient absorption following photolysis of CH_3CHI_2 with no O_2 present (N_2 buffer gas only), assuming a photodissociation quantum yield of unity and subtracting the contribution of CH_3CHI_2 to the spectrum. The other spectra are derived from published sources.[25]

Appendix 2B. Averaged spectra of CH_3CHOO obtained from SO_2 scavenging and CH_3CHOO self reaction

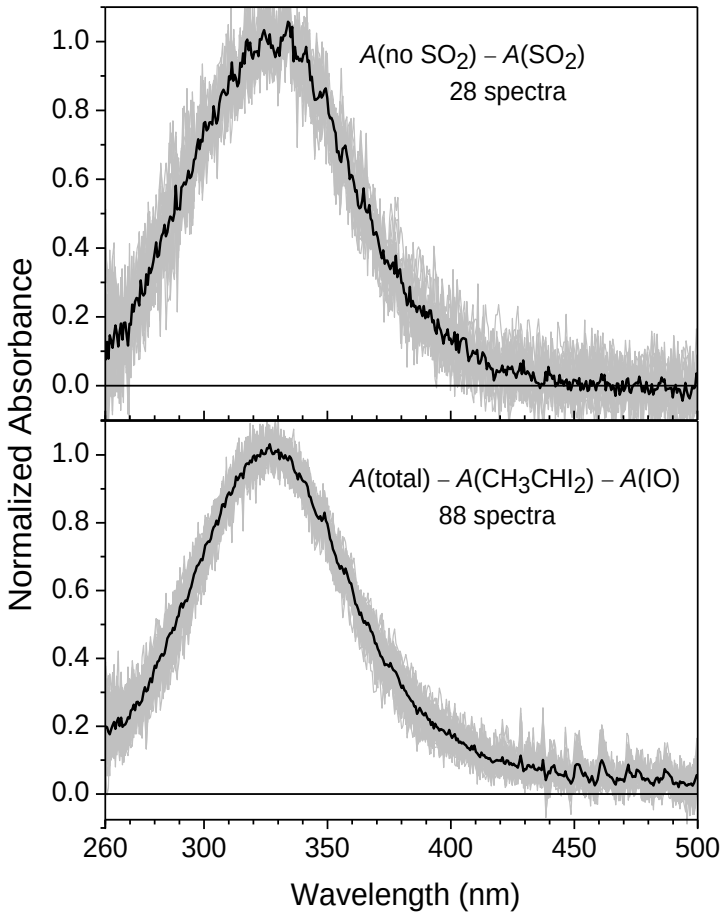

Figure 2B.1. Absorption spectra of CH_3CHOO under various experimental conditions determined with SO_2 scavenging (top) and from CH_3CHOO self-reaction with no SO_2 (bottom). A total of 28 and 88 spectra, respectively, are plotted in gray. The averages are plotted as black lines.

Appendix 2C. Calibration of laser fluence for laser depletion measurements

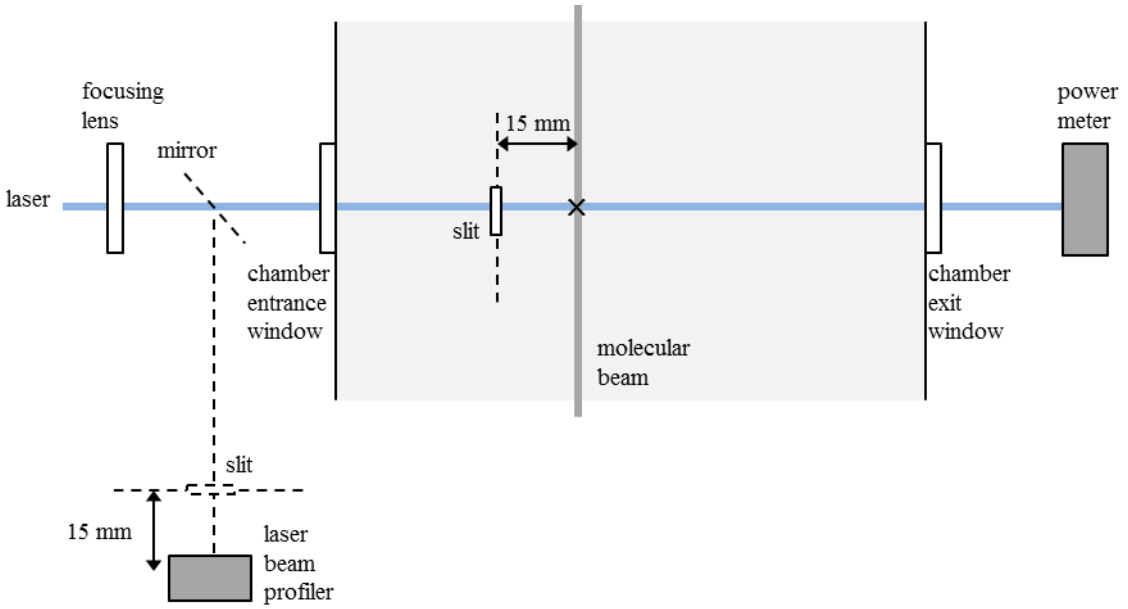

Figure 2C.1. Schematic overhead view (not to scale) of the molecular beam main chamber. The laser was focused by a cylindrical lens (f = 1 m), entered the chamber through a window and passed through a slit before crossing the molecular beam in the region marked X. The average laser power (with a pulse repetition rate of 25 Hz) was measured with a power meter (Gentec-EO, UP25N + Solo 2) outside the chamber. For the laser beam profile measurements, a mirror directed the laser to pass through a similar slit to the profiler (shown by dotted lines), positioned at the same distance from the lens as point X.

Appendix 2D. Cross section values of CH_3CHOO

Table 2D.1. Cross sections of CH_3CHOO from 280 to 440 nm (obtained with SO_2 scavenging). Wavelengths λ are in nm and absorption cross section values σ are in 10^{-20} cm^2.

λ	σ	λ	σ	λ	σ	λ	σ	λ	σ	λ	σ
280.2	377	293.6	741	307.1	1016	320.5	1222	333.9	1301	347.3	1047
280.8	399	294.2	744	307.6	1043	321.0	1240	334.4	1255	347.9	1080
281.3	357	294.8	742	308.2	1063	321.6	1252	335.0	1274	348.4	1074
281.9	404	295.3	721	308.7	1052	322.1	1240	335.6	1211	349.0	1060
282.5	478	295.9	761	309.3	1059	322.7	1245	336.1	1223	349.5	1019
283.0	468	296.4	784	309.8	1085	323.3	1236	336.7	1189	350.1	980
283.6	431	297.0	810	310.4	1100	323.8	1260	337.2	1208	350.6	987
284.1	463	297.5	846	311.0	1094	324.4	1272	337.8	1216	351.2	971
284.7	450	298.1	825	311.5	1102	324.9	1267	338.4	1222	351.8	945
285.3	480	298.7	833	312.1	1121	325.5	1263	338.9	1213	352.3	922
285.8	532	299.2	881	312.6	1106	326.1	1271	339.5	1189	352.9	859
286.4	525	299.8	886	313.2	1088	326.6	1270	340.0	1192	353.4	875
286.9	562	300.3	908	313.8	1082	327.2	1307	340.6	1229	354.0	878
287.5	546	300.9	834	314.3	1150	327.7	1271	341.1	1193	354.6	837
288.0	551	301.5	913	314.9	1131	328.3	1250	341.7	1219	355.1	831
288.6	632	302.0	925	315.4	1154	328.9	1250	342.3	1141	355.7	866
289.2	581	302.6	937	316.0	1182	329.4	1253	342.8	1118	356.2	866
289.7	632	303.1	956	316.6	1189	330.0	1242	343.4	1079	356.8	850
290.3	610	303.7	983	317.1	1228	330.5	1260	343.9	1057	357.4	826
290.8	672	304.3	970	317.7	1200	331.1	1291	344.5	1076	357.9	817
291.4	680	304.8	976	318.2	1206	331.6	1295	345.1	1088	358.5	810
292.0	674	305.4	967	318.8	1192	332.2	1292	345.6	1072	359.0	811
292.5	721	305.9	983	319.3	1208	332.8	1283	346.2	1064	359.6	756
293.1	747	306.5	1001	319.9	1248	333.3	1306	346.7	1081	360.2	724

λ	σ	λ	σ	λ	σ	λ	σ	λ	σ	λ	σ
360.7	724	374.1	451	387.5	260	401.0	178	414.4	101	427.8	62
361.3	683	374.7	438	388.1	272	401.5	163	414.9	66	428.3	48
361.8	697	375.2	455	388.7	255	402.1	139	415.5	38	428.9	62
362.4	712	375.8	437	389.2	243	402.6	142	416.0	65	429.5	52
362.9	682	376.4	476	389.8	258	403.2	154	416.6	65	430.0	43
363.5	674	376.9	436	390.3	254	403.8	166	417.2	63	430.6	35
364.1	648	377.5	426	390.9	245	404.3	154	417.7	77	431.1	58
364.6	649	378.0	411	391.5	247	404.9	141	418.3	76	431.7	49
365.2	645	378.6	382	392.0	223	405.4	114	418.8	74	432.3	24
365.7	662	379.2	383	392.6	204	406.0	117	419.4	55	432.8	28
366.3	627	379.7	347	393.1	229	406.5	130	420.0	77	433.4	19
366.9	634	380.3	354	393.7	227	407.1	152	420.5	66	433.9	5
367.4	610	380.8	366	394.2	207	407.7	127	421.1	71	434.5	15
368.0	588	381.4	361	394.8	182	408.2	126	421.6	76	435.1	31
368.5	557	382.0	340	395.4	177	408.8	103	422.2	60	435.6	30
369.1	543	382.5	310	395.9	184	409.3	122	422.8	68	436.2	41
369.7	514	383.1	330	396.5	194	409.9	119	423.3	53	436.7	19
370.2	529	383.6	318	397.0	210	410.5	92	423.9	46	437.3	47
370.8	501	384.2	333	397.6	193	411.0	116	424.4	48	437.8	43
371.3	497	384.7	303	398.2	183	411.6	81	425.0	54	438.4	44
371.9	472	385.3	294	398.7	162	412.1	99	425.5	82	439.0	35
372.4	472	385.9	271	399.3	191	412.7	95	426.1	85	439.5	16
373.0	457	386.4	277	399.8	182	413.3	93	426.7	49	440.1	18
373.6	446	387.0	289	400.4	144	413.8	72	427.2	70	440.6	32

References

1. W. H. Bunnelle, Chem. Rev. **91**, 335-362 (1991).
2. C. A. Taatjes, D. E. Shallcross and C. J. Percival, *Phys. Chem. Chem. Phys.* **16**, 1704-1718 (2014).
3. R. Criegee, *Angew. Chem. Internat. Edit.* **14**, 745-752 (1975).
4. R. Criegee and G. Wenner, *Liebigs Ann. Chem.* **564**, 9-15 (1949).
5. M. Olzmann, E. Kraka, D. Cremer, R. Gutbrod and S. Andersson, *J. Phys. Chem. A* **101**, 9421-9429 (1997).
6. J. H. Kroll, S. R. Sahay, J. G. Anderson, K. L. Demerjian and N. M. Donahue, *J. Phys. Chem. A* **105**, 4446-4457 (2001).
7. C. A. Taatjes, G. Meloni, T. M. Selby, A. J. Trevitt, D. L. Osborn, C. J. Percival and D. E. Shallcross, *J. Am. Chem. Soc.* **130**, 11883-11885 (2008).
8. O. Welz, J. D. Savee, D. L. Osborn, S. S. Vasu, C. J. Percival, D. E. Shallcross and C. A. Taatjes, *Science* **13**, 204-207 (2012).
9. Y.-T. Su, Y.-H. Huang, H. A. Witek and Y.-P. Lee, *Science* **340**, 174-176 (2013).
10. M. Nakajima and Y. Endo, *J. Chem. Phys.* **139**, 101103 (2013).
11. J. M. Beames, F. Liu, L. Lu and M. I. Lester, *J. Am. Chem. Soc.* **134**, 20045-20048 (2012).
12. L. Sheps, *J. Phys. Chem. Lett.* **4**, 4201-4205 (2013).
13. W.-L. Ting, Y.-H. Chen, W. Chao, M. C. Smith and J. J.-M. Lin, *Phys. Chem. Chem. Phys.* **16**, 10438-10443 (2014).
14. J. H. Lehman, H. Li, J. M. Beames and M. I. Lester, *J. Chem. Phys.* **139**, 141103 (2013).
15. B. Ouyang, M. W. McLeod, R. L. Jones and W. J. Bloss, *Phys. Chem. Chem. Phys.* **15**, 17070-17075 (2013).
16. Z. J. Buras, R. M. I. Elsamra, A. Jalan, J. E. Middaugh and W. H. Green, *J. Phys. Chem. A* **118**, 1997-2006 (2014).
17. D. Stone, M. Blitz, L. Daubney, N. U. M. Howes and P. Seakins, *Phys. Chem. Chem. Phys.* **16**, 1139-1149 (2013).
18. Y. Liu, K. D. Bayes and S. P. Sander, *J. Phys. Chem. A* **118**, 741-747 (2014).
19. O. Welz, A. J. Eskola, L. Sheps, B. Rotavera, J. D. Savee, A. M. Scheer, D. L. Osborn, D. Lowe, A. M. Booth, P. Xiao, M. A. H. Khan, C. J. Percival, D. E. Shallcross and C. A. Taatjes, *Angew. Chem.* **126**, 4635-4638 (2014).
20. Y.-T. Su, H.-Y. Lin, R. Putikam, H. Matsui, M. C. Lin and Y.-P. Lee, *Nature Chemistry* **6**, 477-483 (2014).
21. M. Boy, D. Mogensen, S. Smolander, L. Zhou, T. Nieminen, P. Paasonen, C. Plass-Dülmer, M. Sipilä, T. Petäjä, L. Mauldin, H. Berresheim and M. Kulmala, *Atmos. Chem. Phys.* **13**, 3865-3879 (2013).
22. C. A. Taatjes, O. Welz, A. J. Eskola, J. D. Savee, A. M. Scheer, D. E. Schallcross, B. Rotavera, E. P. F. Lee, J. M. Dyke, D. K. W. Mok, D. L. Osborn and C. J. Percival, *Science* **340**, 177-180 (2013).
23. J. M. Beames, F. Liu, L. Lu and M. I. Lester, *J. Chem. Phys.* **138**, 244307 (2013).
24. M.-N. Su and J. J.-M. Lin, *Rev. Sci. Instrum.* **84**, 086106 (2013).
25. S. P. Sander, J. P. D. Abbatt, J. R. Barker, J. B. Burkholder, R. R. Friedl, D. M. Golden, R. E. Huie, C. E. Kolb, M. J. Kurylo, G. K. Moortgat, V. L. Orkin and P. H. Wine, (Jet Propulsion Laboratory, Pasadena, 2011).
26. J. J.-M. Lin, D. W. Hwang, S. Harich, Y. T. Lee and X. Yang, *Rev. Sci. Instrum.* **69**, 1642-1646 (1998).
27. H.-Y. Chen, C.-Y. Lien, W.-Y. Lin, Y. T. Lee and J. J.-M. Lin, *Science* **324**, 781-784 (2009).
28. J. C. Mossinger, D. E. Shallcross and R. A. Cox, *J. Chem. Soc. Faraday Trans.* **94**, 1391-

1396 (1998).
29. G. Schmitt and F.J. Comes, *J. Photochem.* **14**, 107-123 (1980).
30. W. Chehade, B. Gür, P. Spietz, V. Gorshelev, A. Serdyuchenko, J. P. Burrows and M. Weber, *Atmos. Meas. Tech.* **6**, 1623-1632 (2013).
31. K. T. Kuwata, M. R. Hermes, M. J. Carlson and C. K. Zogg, *J. Phys. Chem. A* **114**, 9192 (2010).
32. B. J. Finlayson-Pitts and J. N. Pitts, *Chemistry of the Upper and Lower Atmosphere*. (Academic Press, San Diego, 2000).
33. J. Rogers, *J. Phys. Chem.* **94**, 4011-4015 (1990).

Chapter 3

Strong negative temperature dependence of the simplest Criegee intermediate CH_2OO reaction with water dimer

Adapted with permission of all coauthors from Smith, M. C.; Chang, C.-H.; Chao, W.; Lin, L.-C.; Takahashi, K.; Boering, K. A.; Lin, J. J.-M.; *J. Phys. Chem. Lett*. **2015**, *6*, 2708-2713, DOI: 10.1021/acs.jpclett.5b01109.

3.1 Introduction

Criegee intermediates (CIs), including CH_2OO and other substituted carbonyl oxides, form in the atmosphere primarily via reactions between ozone and unsaturated hydrocarbons (ozonolysis). CIs are thought to play a significant role in the oxidizing capacity of the atmosphere, as evidenced by studies connecting ozonolysis products to OH and H_2SO_4 formation as well as aerosol growth.[1–6] Determining the rates and mechanisms of the reactions of CIs with water vapor is necessary to evaluate the relative influence of various CIs on the production of atmospheric oxidants and aerosol precursors, *e.g.*, from reactions with SO_2 and NO_2, since the reactions of CIs with water compete with these other processes.

Investigations of CH_2OO formed by C_2H_4 ozonolysis typically use indirect methods to measure the reaction kinetics (*i.e.*, rate determinations are made relative to a reaction with a known rate or by detection of the product of another CH_2OO reaction). These methods have yielded a wide range of values for the rate coefficient of CH_2OO reaction with water, from 1.6×10^{-17} to 1.5×10^{-12} $cm^3\ s^{-1}$.[7–10] Recently, Berndt *et al.*[11] measured competing reactions for CH_2OO from C_2H_4 ozonolysis at high water concentrations and observed second order kinetics with regard to $[H_2O]$ for CH_2OO loss, signifying a fast rate of CH_2OO reaction with $(H_2O)_2$. They estimated the $CH_2OO + (H_2O)_2$ rate coefficient, k_{dimer}, to be $\sim1.1\times10^{-11}$ $cm^3\ s^{-1}$, and suggested that discrepancies among experiments may be due to differences in the water vapor concentrations, since the effect of $(H_2O)_2$ on the reaction rates will depend on the $[H_2O]$ used in the experiments.[11]

The method introduced by Welz *et al.*[12] to produce detectable levels of stabilized CIs (from photolysis of diiodoalkanes in O_2) has prompted many studies reporting direct measurements of CIs, leading to new insights into their structures and reactivities.[13–21] CH_2OO, the simplest CI, has been investigated extensively using the reaction scheme $CH_2I_2 + h\nu \rightarrow CH_2I + I$ and $CH_2I + O_2 \rightarrow CH_2OO + I$. Investigations of the CH_2I_2/O_2 photolysis system, utilizing photoionization mass spectrometry[12] and UV, IR, and microwave spectroscopy,[16,17,22] indicate that CH_2OO is the predominant isomer formed. Studies of CH_2OO reaction kinetics using this scheme show that CH_2OO reacts rapidly with SO_2, NO_2, and some atmospheric organic compounds.[12,23–26] Notably, the reaction of CH_2OO with SO_2 has a large rate coefficient of $(3.9 \pm0.7)\times10^{-11}$ $cm^3\ s^{-1}$ determined by Welz *et al.*[12] In contrast, the reaction of CH_2OO with H_2O was not detectable in that study, and an upper limit of 4×10^{-15} $cm^3\ s^{-1}$ was given for the rate coefficient.[12] As stated by Berndt *et al.*,[11] the H_2O concentrations in the Welz *et al.* experiment were too low ($\leq 3\times10^{16}$ cm^{-3}) to reveal the effect of water dimer on the CH_2OO loss rates. However, relative rate studies of CH_2OO from CH_2I_2 photolysis performed by Stone *et al.*[23] and by Ouyang *et al.*[26] at higher H_2O concentrations also yielded small rate coefficients below 1×10^{-16} $cm^3\ s^{-1}$, a discrepancy that could not be explained by Berndt and coworkers.[11]

Very recently, Chao *et al.*[27] used the strong UV absorption of CH_2OO at 340 nm[17] to measure the kinetics of CH_2OO reaction with water vapor at high water concentrations. Clear second-order kinetics with respect to $[H_2O]$ were observed, providing direct evidence for the fast reaction with water dimer. The value reported by Chao *et al.*[27] for k_{dimer} at 298 K, $(6.5\pm0.8)\times10^{-12}$ cm^3 s^{-1}, is about half the value from the Berndt *et al.* study (which used a slightly different temperature of 293 K and a different source for the water dimer equilibrium constants)[11] but within 2σ of $k_{dimer}(298\ K) = (4.0\pm1.2)\times10^{-12}$ cm^3s^{-1} determined by Lewis *et al.* using a similar direct CH_2OO UV absorption method.[28] Chao *et al.*[27] proposed that interferences to the detected signal from products of the reaction of CH_2OO with water could account for the slower apparent rates reported by Stone *et al.*[23] and Ouyang *et al.*[26]

Given that the k_{dimer} value is in the order of 10^{-12} cm^3 s^{-1}, the reaction with water dimer would be the main pathway for atmospheric CH_2OO loss since the concentration of $(H_2O)_2$ in the troposphere is on the order of 10^{14} cm^{-3}, much higher than those of other potential reactants like SO_2, NO_2 and organic compounds. The fast reaction rate of CH_2OO with water dimer will lead to a low steady state concentration of CH_2OO in the troposphere. However, because temperature and humidity can vary widely both regionally and seasonally, the actual loss rate of CH_2OO due to reaction with water vapor could potentially depend strongly on atmospheric conditions. To better understand the atmospheric impact and mechanism of the CH_2OO reaction with water dimer, we measured the transient absorption of CH_2OO as a function of temperature and H_2O concentration and compared the temperature-dependent rate coefficient with quantum chemical calculations.

3.2 Experimental methods

The experimental apparatus has been described previously.[17,20,27,29] In brief, the N_2 carrier gas is premixed with O_2, CH_2I_2 and water vapor in Teflon tubes and enters a ~76 cm long photolysis reactor; 248 nm light from an excimer laser photodissociates CH_2I_2 and induces formation of CH_2OO, which is monitored continuously in real time by its strong absorption at 340 nm. A broadband plasma light source (Energetic, EQ99) is directed through the reactor in a multiple-pass configuration (6 or 8 passes) to increase the absorption signal, which is measured by a balanced photodiode detector (Thorlabs, PDB450A) through a 335-345 nm bandpass filter. For this work, the photolysis reactor was immersed in a temperature-controlled circulating water bath. The measured temperature stability was better than ±0.3 K (with accuracy better than ±0.6 K) for all experiments.

For the experiments in this work, CH_2OO was produced and detected in a cylindrical glass reactor (75.9 cm long, 25 mm inner diameter) with anti-reflection coated fused SiO_2 windows. The reactor was suspended in a plastic container connected to a temperature-controlled water circulator (Yih Der BL-730, stability ±0.1 K). The temperature of the reactor was measured with 3 resistance temperature detectors (RTDs, Newport Omega, F2020-1000-A) located in glass wells near the center and the two ends of the reactor. Prior to experiments, the reactor gas temperature under typical experimental conditions was calibrated against the RTD readings with a Rotronic temperature and humidity sensor (Rotronic, HC2-S; 0.1-0.2 K temperature accuracy; 0.8% relative humidity accuracy at 298 K, 1.3% at 273 K and 313 K, 1.8% at 333 K) placed inside the reactor at different water bath temperatures and different sensor locations. (This Rotronic sensor was removed for the kinetic measurements.) The error in temperature estimated from this calibration is less than 0.3 K. The temperature stability throughout each

experiment was typically better than 0.3 K, leading to an upper limit of 0.6 K for the overall temperature uncertainty.

The carrier gas N_2 was mixed with water vapor, O_2, and CH_2I_2 in Teflon tubes upstream of the reactor. Water vapor was introduced into the gas mixture by passing a portion of the carrier gas over a heated water surface to produce the desired relative humidity in the photolysis reactor. For Experiments #1, 4, and 5 (see Table 3.1), water vapor was introduced to the gas mixture by passing N_2 over a water surface heated ~5 K above room temperature. For Experiments #2, 3, and 6, a different water reservoir was used that could be heated to temperatures close to the reactor temperature to obtain higher [H_2O]. The CH_2I_2 liquid was also slightly heated (~5 K above room temperature) to improve the stability of the vapor concentration in the reactor. The gas mixing ratios were adjusted with mass flow controllers (Brooks, 5850E or 5800E). For Experiments #1, 4, and 5, the gas mixture passed through a smaller absorption cell (75.3 cm long) upstream of the reactor in which the concentration of CH_2I_2 was monitored continuously during each experiment. For Experiments #2, 3, and 6, this smaller cell was removed and CH_2I_2 absorption was monitored in the reactor before and after each kinetic experiment. The gas mixture entered the reactor through an inlet in the center and exited to the vacuum pump through outlets at each end of the reactor. Small streams of N_2 gas (~5% of the total flow) were used to purge the windows; both the purge gas and the sample gas mixture were preheated to the water bath temperature in copper tubes upstream of the reactor. Flow rates were adjusted to fully refresh the gas in the reactor between 1 Hz photolysis pulses.

The relative humidity inside the reactor was calibrated at different temperatures and H_2O concentrations, using the same Rotronic sensor described above against a second Rotronic sensor located upstream of the reactor before the CH_2I_2 vapor was added into the gas mixture (to protect the sensor from CH_2I_2 contamination). The reactor relative humidity differs by 2% or less from the value predicted by the upstream measurement; this uncertainty, denoted $\varepsilon_{\mathrm{mix}}$, is likely attributed to effects from gas mixing, temperature fluctuations and water adsorption/desorption from the reactor walls (since there is no humidity sensor inside the reactor during the kinetic measurements). The accuracy range of the relative humidity sensor (0.8-1.8%, see above) leads to another source of uncertainty, denoted $\varepsilon_{\mathrm{Rotronic}}$. The uncertainty in the temperature above the heated water surface T_{up} (0.3-0.6 K) causes up to 4% error, denoted ε_{T}, in the water vapor pressure $P_{\mathrm{sat}}(T_{\mathrm{up}})$ (assume 7% per Kelvin[27]). The water concentration [H_2O] is calculated as in equations (1) and (2).

(1) $$[\mathrm{H_2O}]_{\mathrm{sat}}^{\mathrm{up}} = \frac{P_{\mathrm{sat}}(T_{\mathrm{up}})}{k_{\mathrm{b}} T_{\mathrm{up}}}$$

(2) $$[\mathrm{H_2O}] = RH[\mathrm{H_2O}]_{\mathrm{sat}} \frac{P}{P_{\mathrm{up}}} \frac{T_{\mathrm{up}}}{T}$$

In equations (1) and (2), *RH* is the relative humidity measured with the upstream Rotronic sensor, $[H_2O]_{sat}$ is the water concentration at the saturation pressure, P_{up} is the pressure at the upstream sensor, *P* and *T* are the pressure and temperature in the reactor, and k_b is Boltzmann's constant. The main uncertainty in [H_2O], denoted $\varepsilon_{\mathrm{H_2O}}$, can be estimated with equation (3).

(3) $$\varepsilon_{\mathrm{H_2O}} = \sqrt{(\varepsilon_{\mathrm{mix}}\,[\mathrm{H_2O}])^2 + (\varepsilon_{\mathrm{Rotronic}}\,[\mathrm{H_2O}]_{\mathrm{sat}})^2 + (\varepsilon_{\mathrm{T}}\,[\mathrm{H_2O}])^2}$$

Appendix 3A shows the dependence of $\varepsilon_{\mathrm{H_2O}}$ on temperature and water concentration for Experiment #2 as an example. The absolute error in [H_2O] increases with [H_2O] and with

upstream temperature (due primarily to higher $P_{sat}(T)$ used for high temperature experiments – see Table 3.1).

For the concentration of $(H_2O)_2$, the reported percentage error $\varepsilon_{K_{eq}}$ in the dimerization equilibrium constant K_{eq} ranges from 2.9% at 325 K to 3.3% at 285 K.[30] Additionally, the error in $[H_2O]$ described above contributes to the error in $[(H_2O)_2]$, $\varepsilon_{(H_2O)_2}$. (The direct contribution to $\varepsilon_{(H_2O)_2}$ of the uncertainty in reactor temperature is relatively minor.) We estimated the water dimer concentration and its error with equations (4) and (5).

(4) $[(H_2O)_2] = K_{eq}[H_2O]^2$

(5) $\varepsilon_{(H_2O)_2} = \sqrt{\left(2\frac{\varepsilon_{H_2O}}{[H_2O]}\right)^2 + \varepsilon_{K_{eq}}{}^2}\ [(H_2O)_2]$

Appendix 3A shows the dependence of $\varepsilon_{(H_2O)_2}$ on temperature and water dimer concentration for Experiment #2 as an example. The error in $[(H_2O)_2]$ increases rapidly with $[(H_2O)_2]$ due mainly to the dependence on ε_{H_2O}.

The transient absorption setup in this work is similar to that described by Chao *et al.* and previous studies.[17,20,27,29] Light from an excimer laser (Coherent, CompExPro 205, KrF 248 nm) collimated by a cylindrical lens (f = 1 m) passed collinearly through the reactor by reflection from two ultra-steep long pass filters at 257 nm (Semrock, LP02-257RU-25) to photolyze CH_2I_2 and produce CH_2OO. A thermal pile power meter (Gentec EO, UP19K-30H-VM-D0) was used to measure the average laser power (~12-20 mJ/pulse) throughout each experiment. To measure absorption, a broadband plasma light source (Energetiq, EQ-99) was directed through the reactor with a spherical mirror and SiO_2 prism to achieve either 6 or 8 passes. Light at 335-345 nm (corresponding to absorption by CH_2OO) was detected with a balanced photodiode detector (Thorlabs, PDB450A) through a band pass filter (Edmund Optics, 65129, 10 nm OD4 band pass filter at 340 nm). To minimize fluctuation of the light source intensity, a reference signal (originating from the same light source but bypassing the reactor) was measured simultaneously and subtracted from the absorption signal. A ~1% transmittance change was observed after the laser pulse even without adding CH_2I_2 in the gas mixture; this signal was also subtracted from the CH_2OO absorption signal at each H_2O concentration. A digital oscilloscope (LeCroy, HDO4034) recorded the photodiode output and averaged the signals over 120 laser pulses.

3.3 Results and discussion

3.3.1 Temperature dependence of CH_2OO loss due to water reaction

Table 3.1 lists the experiments performed in this work and the corresponding conditions. Representative difference transient absorption traces under dry (without adding water) and wet (with water vapor added) conditions at 283 K, 298 K, 311 K and 324 K are shown in Figure 3.1. (See Appendix 3B for difference absorption traces for all experiments.) The rapid increase in absorption after the photolysis laser pulse at time = 0 (photolyzing CH_2I_2 in the reactor to generate CH_2I) corresponds to CH_2OO formation from $CH_2I + O_2$, and the subsequent decrease in absorption over several milliseconds is attributed to CH_2OO loss.

Under dry conditions, the decay in CH_2OO absorption is due primarily to CH_2OO reactions with radical species, including I atoms, CH_2IOO, and CH_2OO,[31] while under wet conditions CH_2OO reaction with water dominates the observed decay. The change in CH_2OO concentration with time t can be described by the kinetic expression in equations (6) and (7) in which k_{obs} is the sum of the dry loss rate, k_0, and the loss rate due to reaction with water vapor, k'_w, similar to Chao *et al.*;[27] the transient absorption traces were fit to a single exponential decay to yield the decay constant k_{obs}.

(6) $$-\frac{d[CH_2OO]}{dt} = k_0[CH_2OO] + k'_w[CH_2OO] = k_{obs}[CH_2OO]$$

(7) $$[CH_2OO]_t = [CH_2OO]_0 exp(-k_{obs}t)$$

The reaction kinetics of CH_2OO in the $CH_2I + O_2$ reaction system has been investigated by Ting *et al.*[31] In equation (6), the $k_0[CH_2OO]$ term includes contributions from several reactions including $CH_2OO + CH_2OO \rightarrow$ products; $CH_2OO + I + M \rightarrow CH_2IO_2 + M$; $CH_2OO + I \rightarrow IO + CH_2O$; and $CH_2OO + CH_2IO_2 \rightarrow$ products. Under the experimental conditions of high pressures and low CH_2OO concentrations, the self-reaction of CH_2OO is not expected to dominate in the $[CH_2OO]$ decay;[31] this assumption is supported by the pseudo-first-order kinetics of the observed decay. Furthermore, there is no evidence that the contributions of the above reactions depend on water concentration. Sheps *et al.*[32] measured the kinetics of the reaction of *syn*-CH_3CHOO with water, which was found to be very slow; their plot of k_{obs} as a function of $[H_2O]$ has a zero slope, suggesting that k_0 for the syn-CH_3CHOO reaction with water does not depend on $[H_2O]$. Here it was assumed that k_0 for CH_2OO reaction with water is also independent of $[H_2O]$ and that equation (6) is valid under the present conditions.

Under dry conditions $k_{obs} = k_0$; subtracting k_0 from k_{obs} yields k'_w at different water concentrations, which are plotted in Figure 3.2. The relationship between k'_w and $[H_2O]$ at all studied temperatures is second order, suggesting the observed CH_2OO loss is dominated by reaction with water dimer.[27] It is clear that the CH_2OO decay rates at higher temperatures are significantly slower for a given H_2O concentration.

The second-order kinetics with regard to $[H_2O]$ indicates that k'_w can be fit to a linear relationship with $[(H_2O)_2]$ as shown in Figure 3.2, in which the slope corresponds to $k_{dimer}(T)$ (see equation (8)). Equation (9) is used to determine $[(H_2O)_2]$ at a given temperature, in which $K_{eq}(T)$ is the temperature-dependent equilibrium constant for water dimerization. We used the $K_{eq}(T)$ values reported by Ruscic,[30] who utilized the Active Thermochemical Tables approach; the reported uncertainties range from 2.9-3.3% in the temperature range studied here. The following k_{dimer} values were obtained by averaging the slopes from all experiments at each temperature: $k_{dimer}/(10^{-12}\ cm^3\ s^{-1})$ = 12.1±1.7, 7.4±0.6, 4.8±0.5, 3.3±0.7 for 283, 298, 311, 324 K, respectively.

(8) $$(k_{obs} - k_0) = k'_w = k_{dimer}(T)[(H_2O)_2]$$

(9) $$K_{eq}(T) = \frac{[(H_2O)_2]}{[H_2O]^2}$$

Table 3.1. Summary of experiments for the temperature dependence of the CH_2OO reaction with water vapor.

Exp. #	# passes	Laser fluence[a] /mJ cm^{-2}	$[CH_2I_2]$ /10^{14} cm^{-3}	$P_{CH_2I_2}$ (298 K) / 10^{-3} Torr	$[CH_2OO]_0$ /10^{12} cm^{-3}	P_{O_2} /Torr	$P_{CH_2I_2}$ /Torr	T_{up}[b] / K	T_{cell} / K	k_0 / s^{-1}	k_{dimer} / 10^{-12} cm^3s^{-1}
1a	6	4.9	1.06	3.26	0.78	12.0	527.4	~ 303	298.9	284	6.5±0.6
1b	6	4.8	1.04	3.21	0.79	11.2	499.2	~ 303	282.8	308	12.1±1.7
2a	8	5.7	2.35	7.24	1.47	12.0	526.5	~ 308	298.1	595	7.4±0.9
2b	8	9.9	2.35	7.24	1.56	12.6	547.5	~ 308	310.6	600	4.5±0.5
2c	8	5.8	2.35	7.24	2.23	4.5	204.4	~ 328	323.8	663	3.2±0.4
3a	8	9.1	1.12	3.47	1.77	11.7	204.5	~ 308	299	587	7.5±0.7
3b	8	9.1	1.12	3.47	1.76	11.8	204.6	~ 314	310.3	549	5.0±0.5
3c	8	10.5	1.12	3.47	1.23	12.9	573.3	~ 328	323.8	448	3.2±0.7
4	8	11.3	2.15	6.64	2.66	12.5-14.4	525-605[c]	~ 303	298-323	982	2.6±0.3 – 8.2±0.8[d]
5	8	10.8	1.85	5.70	2.28	12.5-14.4	525-605[c]	~ 303	298-323	841	2.1±0.2 – 8.5±0.7[d]
6	8	8.5	1.20	3.80	2.05	12.3	250.1	~ 308	298-324	630	2.3±0.2 – 8.0±0.7[d]

[a] Typical uncertainty in laser fluence ~ 2-5%; uncertainty in $[CH_2I_2]$ ~ 1-3% (Experiments #1, 4, and 5) and ~ 5-13% (Experiments #2, 3, and 6); uncertainty in $[CH_2OO]_0$ ~ 5-11%. Variation in k_0 for a given experiment ranges from ~ 2-8% (see Appendix 3C). [b] T_{up} refers to the temperature of the heated water surface upstream of the reactor, which determines the H_2O saturation vapor pressure and therefore the range of H_2O concentrations possible in the reactor. [c] Pressure adjusted to maintain the same total number density [M] at different temperatures for Experiments #4 and 5. [d] See Appendix 3D for temperature dependence of k_{dimer} in Experiments #4-6.

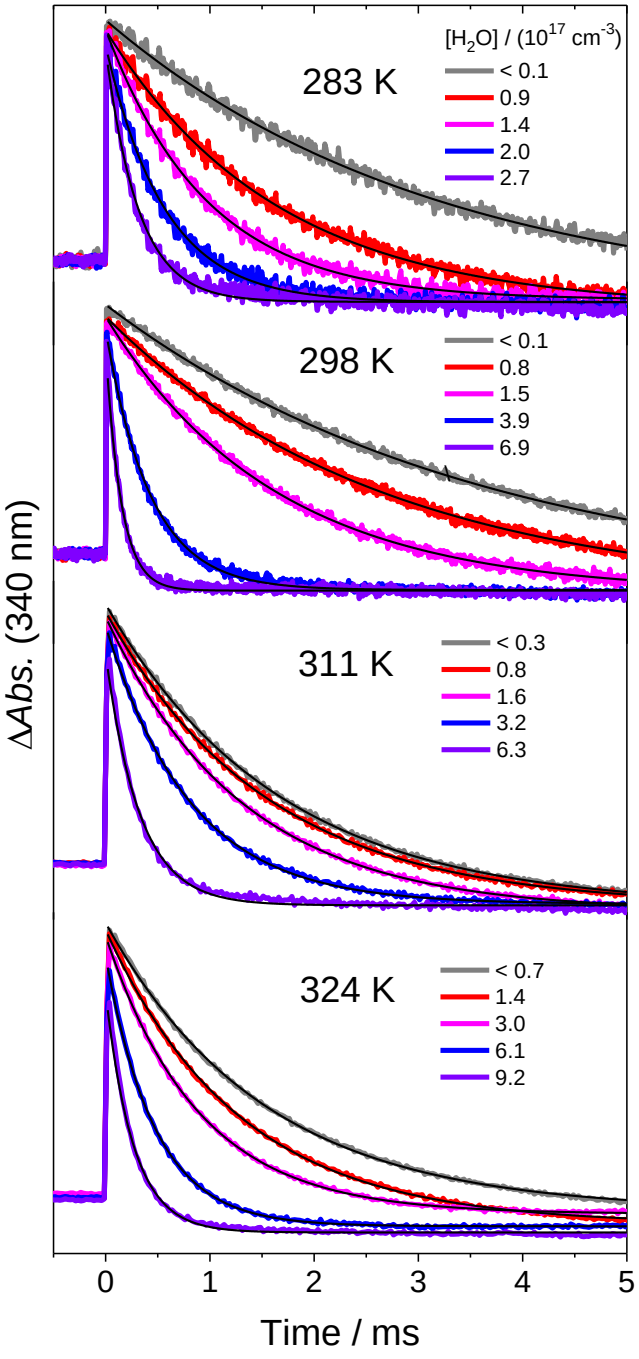

Figure 3.1. Difference transient absorbance traces at 340 nm showing CH_2OO formation and decay at four temperatures, with total pressure P_{total} = 500-600 Torr. Gray traces correspond to dry conditions (no H_2O added) and colored traces correspond to absorbance at different H_2O concentrations. Note that different water concentrations were used for experiments at different temperatures. Black lines are the single exponential fits. The negative baseline at long delay times is attributed to the depletion of the CH_2I_2 precursor, which absorbs weakly at 340 nm. The depletion of CH_2I_2 is a step function[31] and does not affect the rate analysis.

CH_2OO transient absorption was also measured at constant $[H_2O] = (5.4 \pm 0.3) \times 10^{17}$ cm^{-3} at a series of temperatures from 298-324 K, and at total pressures ranging from 200-600 Torr. Measurements of k'_w at different pressures presented in Figure 3.3 show that no pressure dependence was observed. The results from the constant $[H_2O]$ measurements (Experiments #4-6) are shown in Figure 3.4.

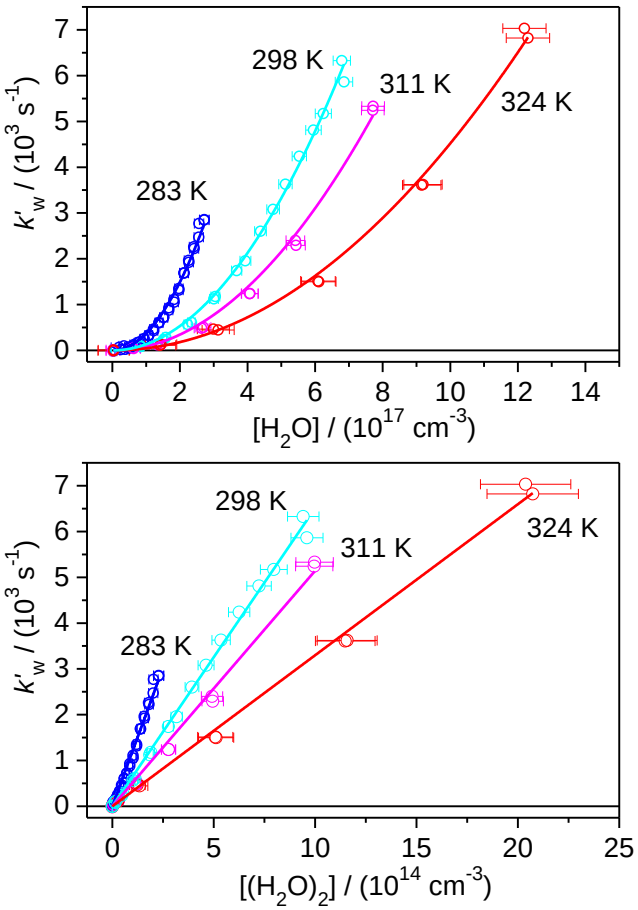

Figure 3.2. Pseudo-first-order CH_2OO loss rate coefficients k'_w plotted against H_2O concentration (top) and $(H_2O)_2$ concentration (bottom). The curves and lines are quadratic and linear fits to the data, respectively.

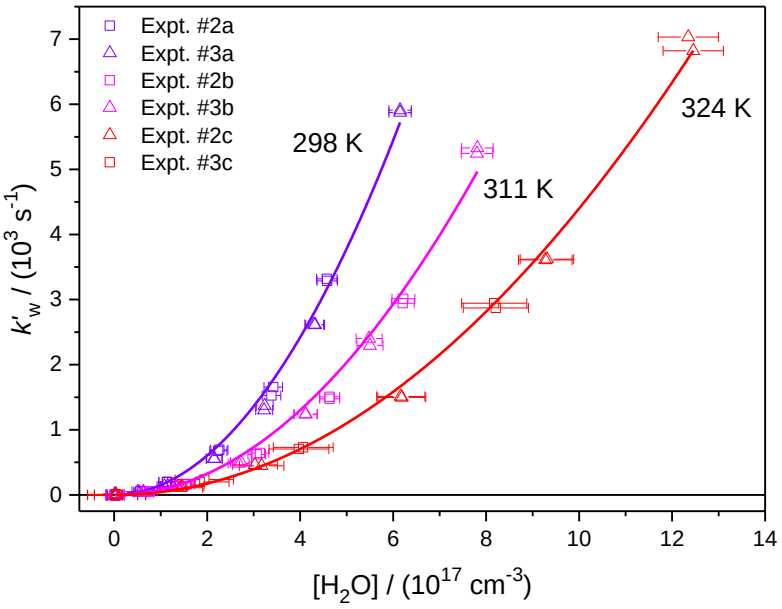

Figure 3.3. Plots of k'_w versus water concentration at different temperatures and total reactor pressures. Squares represent data obtained at high pressure (~ 500-600 Torr), and triangles represent low pressure (~ 200 Torr). Lines are quadratic fits to all the data at each temperature.

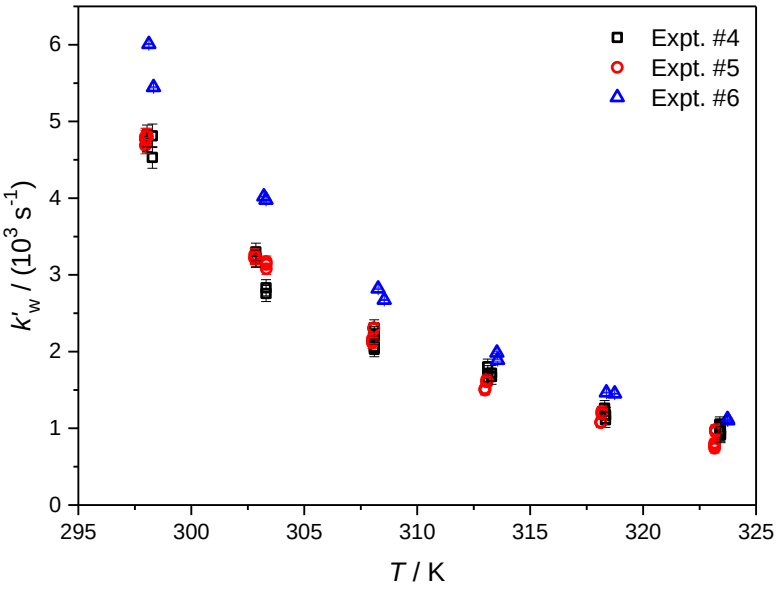

Figure 3.4. Plot of k'_w against reactor temperature for Experiments #4, 5, and 6. (The error in k'_w comes mainly from the uncertainty in k_0 – see Appendix 3C.)

The $k_{dimer}(T)$ values obtained from each experiment with varied [H_2O] (Experiments #1-3) are plotted (triangles) in the Arrhenius plot in Figure 3.5. For the experiments with constant [H_2O], dividing $k'_w(T)$ by [$(H_2O)_2$] yields k_{dimer} as a function of temperature; these values are plotted (squares) for Experiment #6 in Figure 3.5. (See Appendix 3D for an Arrhenius plot of all constant [H_2O] experiments including Experiments #4 and #5.) Fitting the data from this experiment to the Arrhenius form $k(T) = A\,exp(-E_a/RT)$ gives a value of -8.1±0.3 kcal mol^{-1} for E_a.

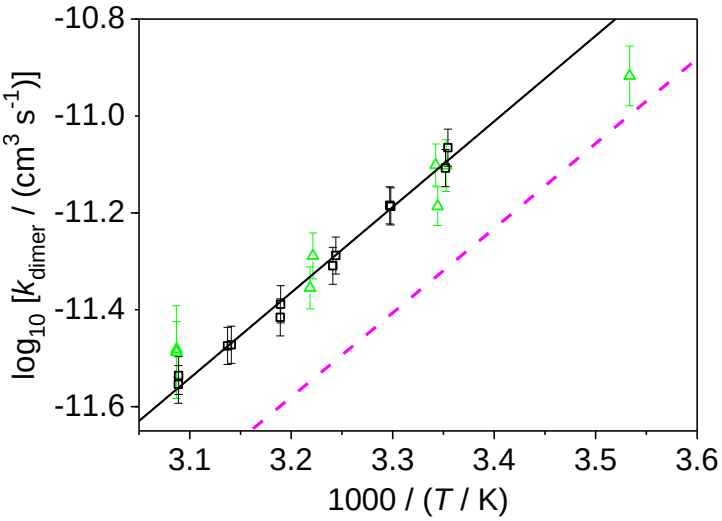

Figure 3.5. Arrhenius plot of k_{dimer}. Green triangles represent k_{dimer} obtained by varying the water dimer concentrations at fixed temperatures (Experiments #1-3; see Table 3.1). Black squares represent k_{dimer} obtained by varying T (298-324 K) at constant [H_2O] (Experiment #6). Solid line is a linear fit to data from Experiment #6. Dashed pink line shows the calculated $k_{dimer}(T)$.

3.3.2 Mechanistic and atmospheric implications

This negative temperature dependence may be explained by a complex-formation reaction mechanism. A previous theoretical analysis[33] predicted that at thermal equilibrium the observed temperature dependence of k_{dimer} should be influenced by the temperature dependence of the equilibrium between reactants and pre-reactive complexes as well as the temperature dependence of the rate coefficient for the complex crossing the transition state to products. The value of k_{dimer} does not show any pressure dependence from 100 to 600 Torr (see Figure 3.3 and Ref. 27), signifying that the experimental conditions are at the high pressure limit and that reactants and pre-reactive complexes have reached thermal equilibrium before the reaction takes place.

Figure 3.5 shows that the calculated $k_{dimer}(T)$ (see the published version of this chapter for calculation details) exhibits a negative temperature dependence with a slope that is similar to the experiment, though the calculation slightly underestimates (by ~30%) the absolute magnitude of the rate coefficients. This slope is attributed to 1) the large dipole moment of

CH_2OO which causes strong interaction with water dimer; and 2) the small geometry change between the complex and the transition state. The former leads to a large binding energy of the pre-reactive complex $CH_2OO\cdot(H_2O)_2$, around 11 kcal mol^{-1}, while the latter causes the reaction barrier to be very low, around 5 kcal mol^{-1}. As a result, the transition state energy lies below the energy of the reactants $CH_2OO+(H_2O)_2$ by about 6 kcal mol^{-1}. Note that the $CH_2OO\cdot(H_2O)_2$ complex may also form via $CH_2OO\cdot H_2O + H_2O$, but this pathway would not change the theoretical results as long as $CH_2OO\cdot(H_2O)_2$ and the reactants are in thermal equilibrium.

Few other examples exist for such a large negative E_a in a gas-phase reaction near room temperature. An activation energy around -13 kcal mol^{-1} has been observed in the reaction of SO_3 with H_2O, attributed primarily to the formation of stable pre-reactive complexes involving $(H_2O)_2$.[34–37] The results presented here for CH_2OO reaction with water dimer imply that the stability of pre-reactive complexes between larger CIs and $(H_2O)_2$ may be a key factor controlling the temperature dependences of their reactions with water vapor.

The temperature dependence of k_{dimer} indicates that CH_2OO loss due to reaction with water vapor will be sensitive to ambient temperatures in the atmosphere. Indeed, the effective first-order CH_2OO loss rate coefficient, $k_{eff} = k_{dimer}(T)[(H_2O)_2]$, depends strongly on atmospheric temperature and relative humidity *RH*; this will influence the steady state concentrations of CH_2OO predicted by atmospheric chemistry models, which in turn influence CH_2OO reaction rates with other species such as SO_2.[27] For example, using the temperature dependence of k_{dimer} obtained in this work gives k_{eff}(*T*=278 K, *RH*=70%)=1570 s^{-1} ($[(H_2O)_2] = 7.5\text{x}10^{13}$ cm^{-3}) and k_{eff}(313 K, 30%)=1900 s^{-1} ($[(H_2O)_2] = 4.2\text{x}10^{14}$ cm^{-3}), while ignoring the temperature dependence would lead to k_{eff}(278 K, 70%)=590 s^{-1} and k_{eff}(313 K, 30%)=3670 s^{-1}.

3.4 Conclusion

In summary, transient absorption measurements of CH_2OO at high concentrations of water vapor from 283 to 324 K reveal a pronounced negative temperature dependence of the rate coefficient for the reaction of CH_2OO with water dimer, and are consistent with theoretical calculations which predict pre-reactive complexes in the reaction mechanism. The strong dependence of the reaction of the simplest CI CH_2OO with water vapor on atmospheric temperature and humidity emphasizes the importance of investigating the reactions of larger CIs with water. Different CIs are likely to display different degrees of temperature dependence, and accurate knowledge of these differences will help constrain the relative importance of various decay pathways of CIs and their influence on atmospheric composition. Since there is currently no method available to measure the concentrations of CIs in the atmosphere, the concentration of atmospheric CH_2OO (as well as concentrations of other CIs) must be estimated from known rates of production and removal. While the rates of production of some CIs can be determined from available ozonolysis rates and CI yields, the rates of CI removal remain highly uncertain. The results presented here will help to constrain CH_2OO removal rates under different atmospheric conditions, an important step toward understanding the impact of CIs on the atmosphere's oxidizing capacity.

Appendix 3A. Absolute errors in H_2O and $(H_2O)_2$ concentrations

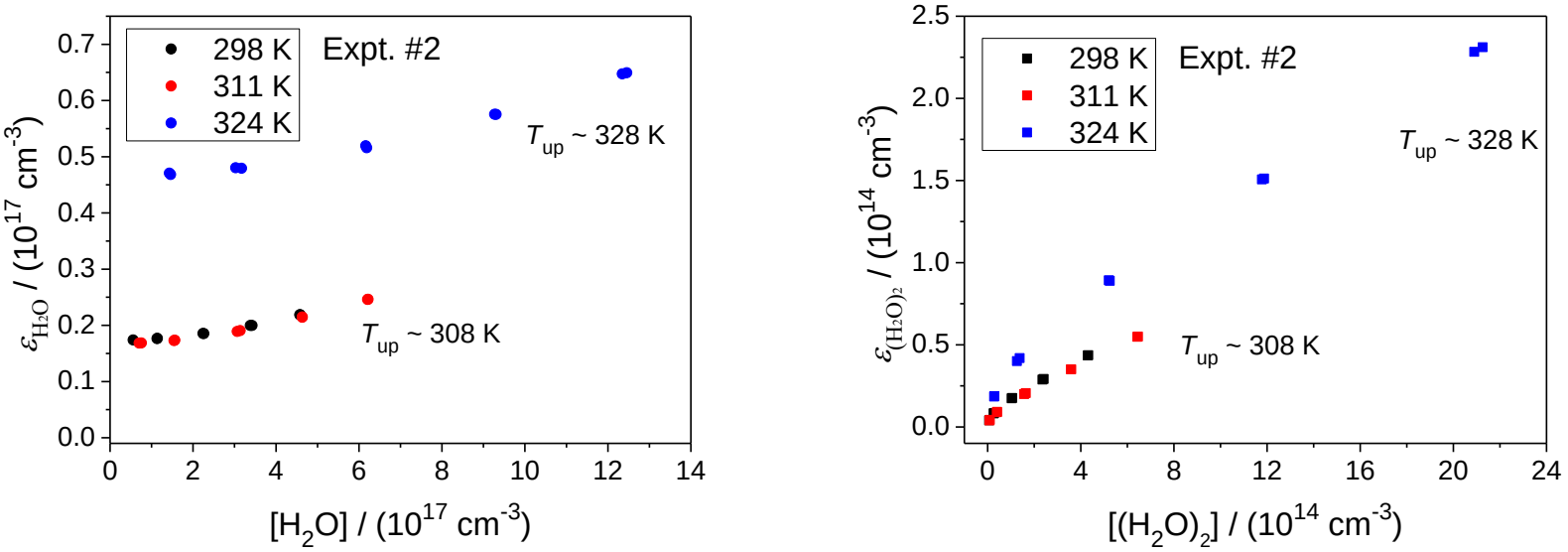

Figure 3A.1. Left: Plot of the absolute error in H_2O concentration, ε_{H_2O}, against [H_2O] for representative data sets at three temperatures. Right: Plot of the absolute error in $(H_2O)_2$ concentration, $\varepsilon_{(H_2O)_2}$, against [$(H_2O)_2$] for representative data sets at three temperatures.

Appendix 3B. Difference absorbance traces and single exponential fits for Experiments #1-6

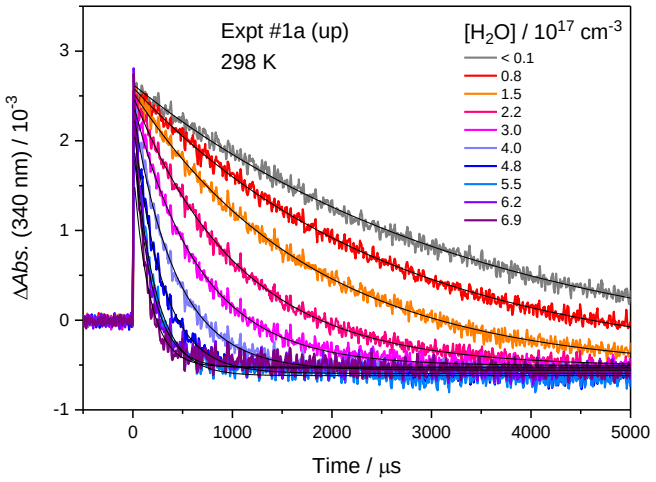

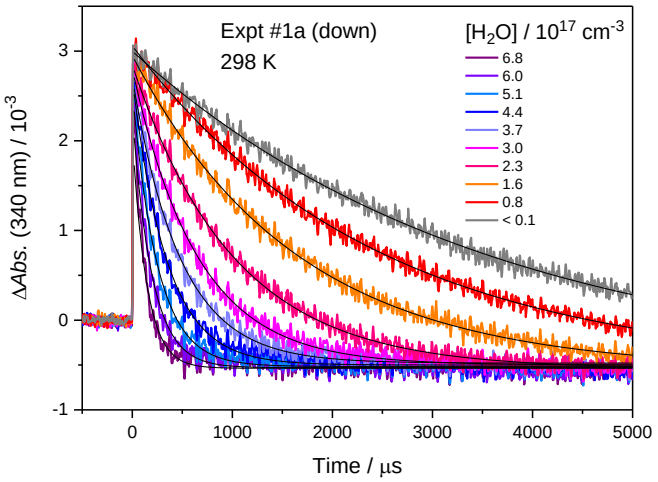

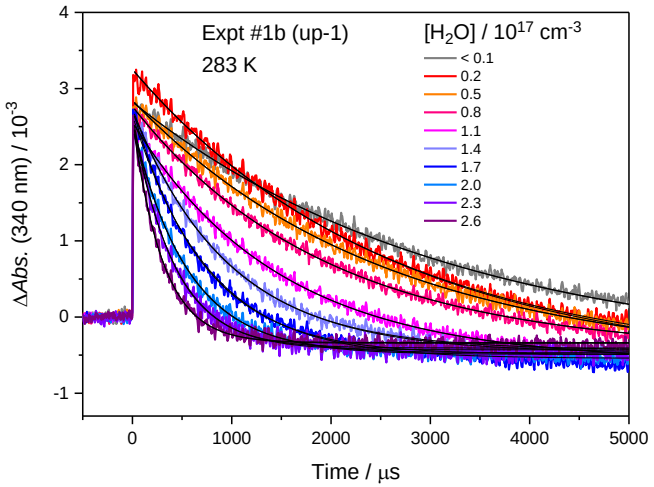

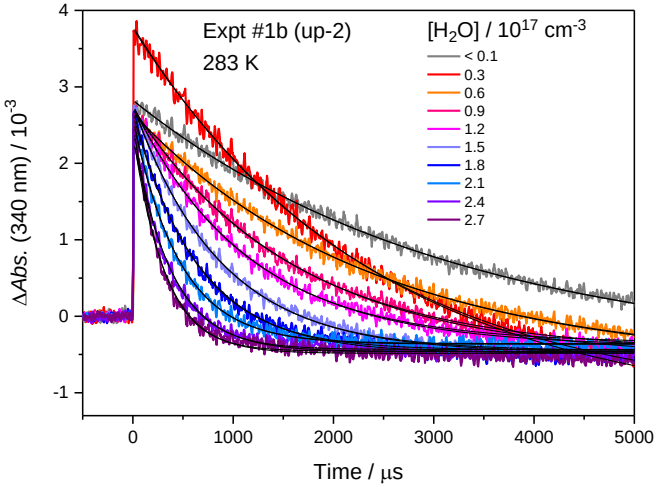

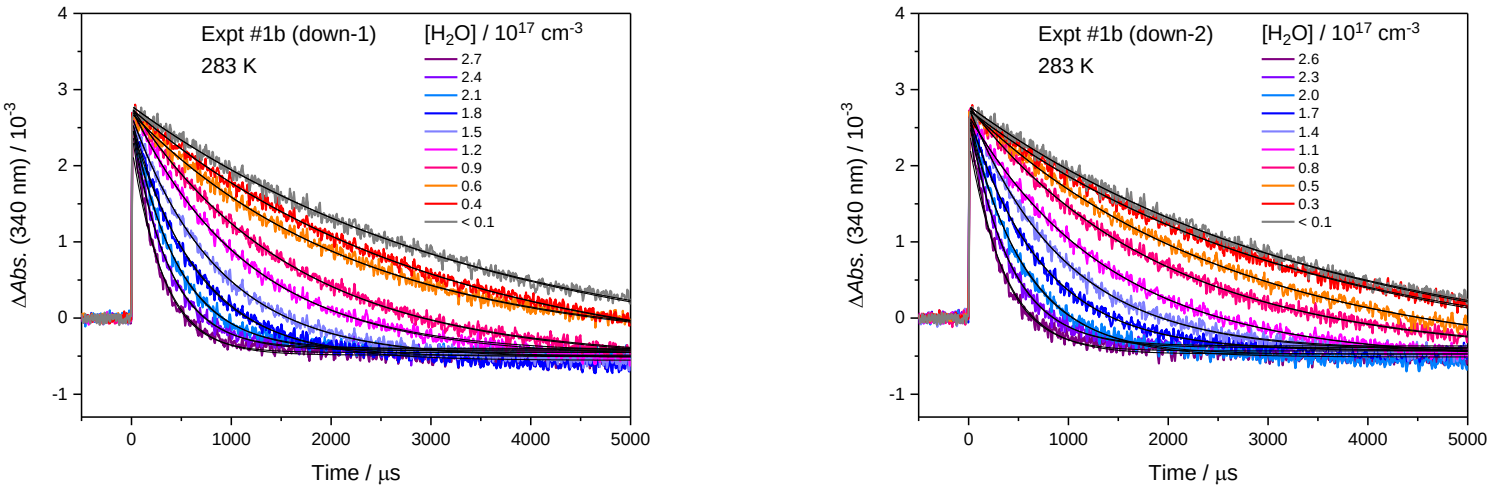

Figure 3B.1. Difference transient absorption traces for Experiments #1a and 1b (298 K and 283 K) at different H_2O concentrations. Plots labeled "up" were obtained by collecting traces at successively higher relative humidities; plots labeled "down" show traces collected at successively lower humidities. The "up" and "down" scans for Experiment #1b are each split into two plots to clearly show the traces. Black lines are single exponential fits. The average R-squared values of the exponential fits are 0.989 and 0.994 for Experiments #1a and 1b respectively.

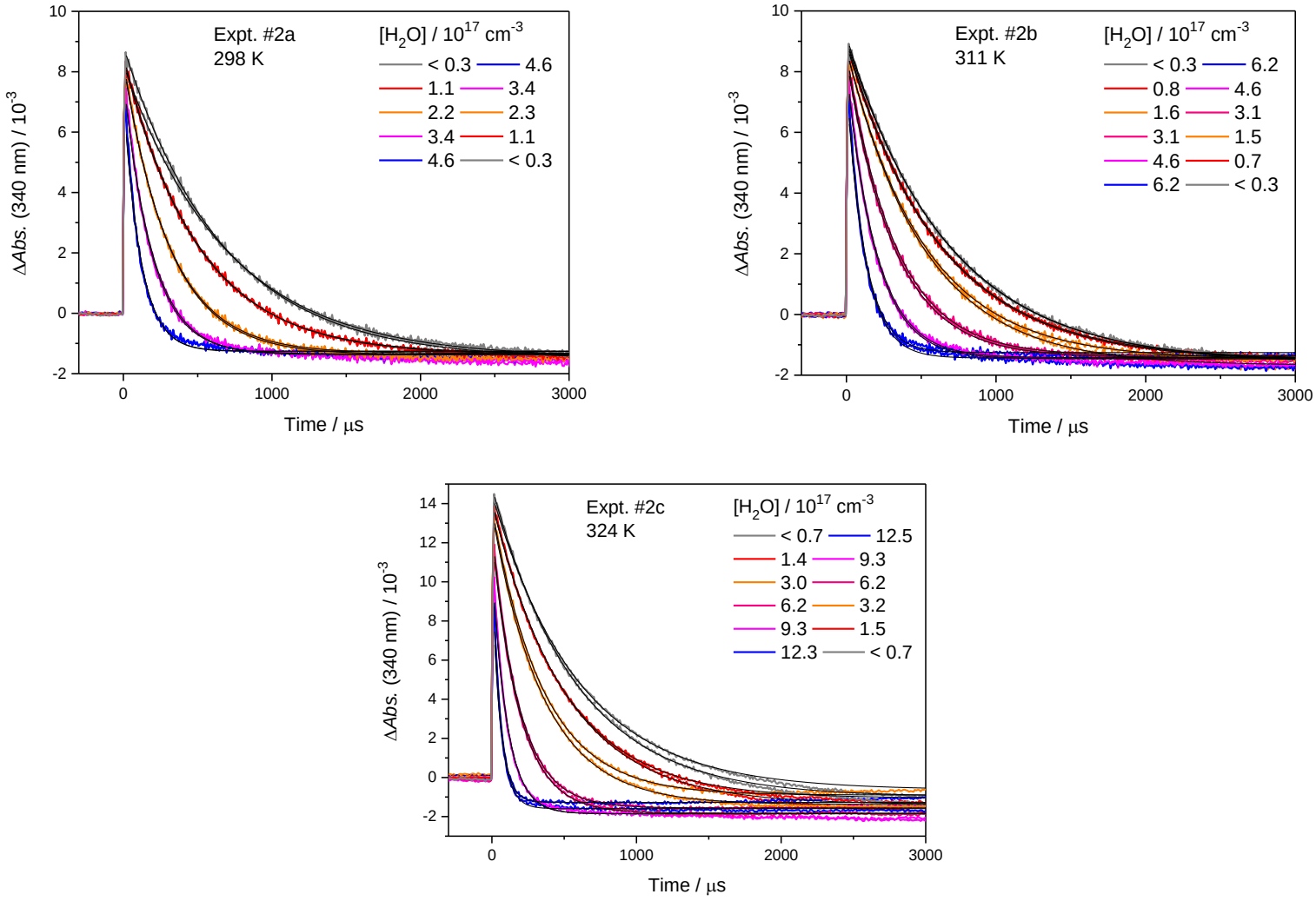

Figure 3B.2. Difference transient absorption traces for Experiments #2a-2c (298 K, 311 K, and 324 K) at different H_2O concentrations. Black lines are single exponential fits. The average R-squared values of the exponential fits are 0.998, 0.998, and 0.999 for Experiments #2a–2c respectively.

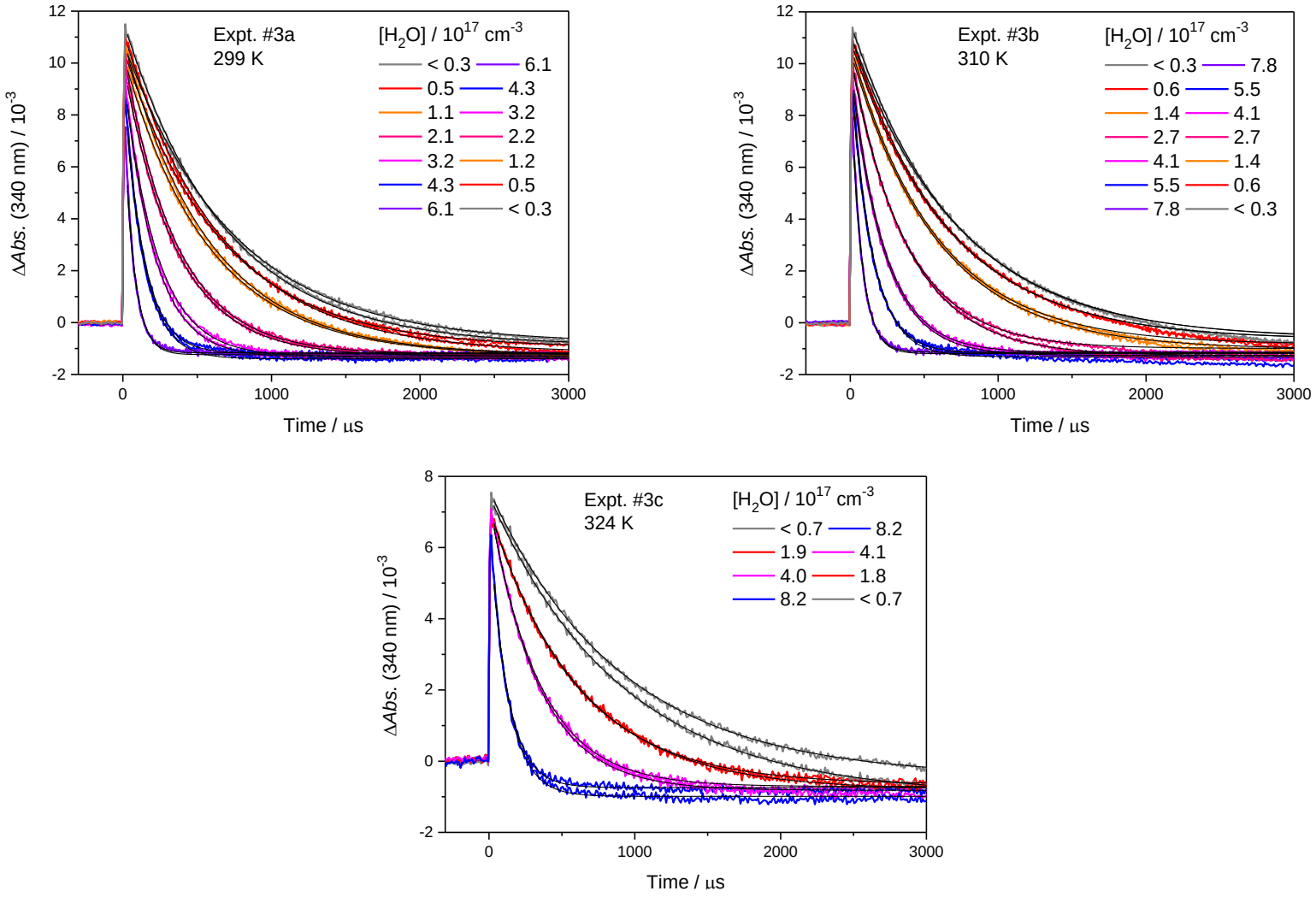

Figure 3B.3. Difference transient absorption traces for Experiments #3a-3c (299 K, 310 K, and 324 K) at different H_2O concentrations. Black lines are single exponential fits. The average R-squared values of the exponential fits are 0.999, 0.999, and 0.987 for Experiments #2a–2c respectively.

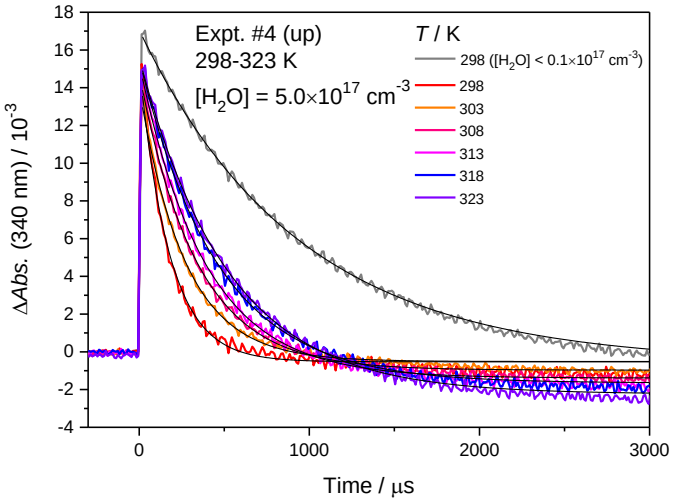
Expt. #4 (up)
298-323 K
[H2O] = 5.0×10^17 cm^-3
T / K
298 ([H2O] < 0.1×10^17 cm^-3)
298
303
308
313
318
323
ΔAbs. (340 nm) / 10^-3
Time / μs

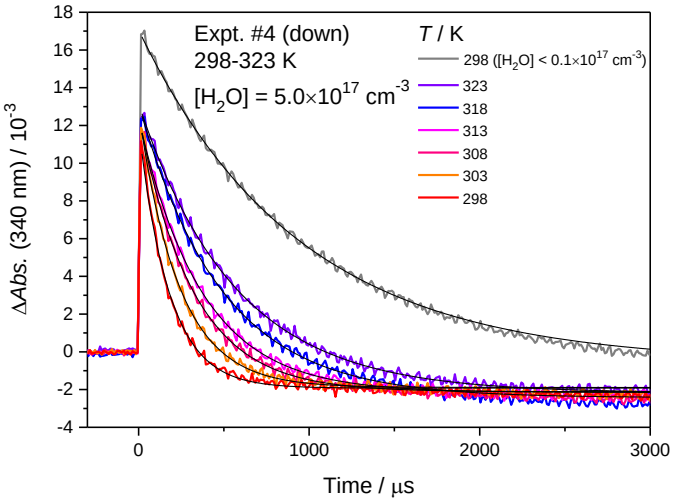
Expt. #4 (down)
298-323 K
[H2O] = 5.0×10^17 cm^-3
T / K
298 ([H2O] < 0.1×10^17 cm^-3)
323
318
313
308
303
298
ΔAbs. (340 nm) / 10^-3
Time / μs

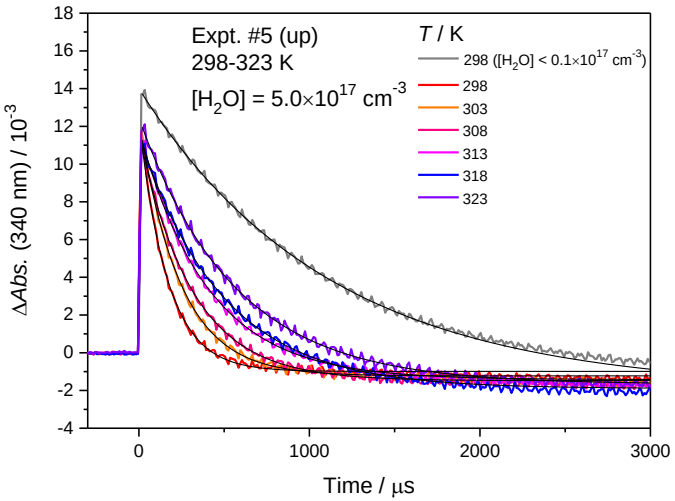
Expt. #5 (up)
298-323 K
[H2O] = 5.0×10^17 cm^-3
T / K
298 ([H2O] < 0.1×10^17 cm^-3)
298
303
308
313
318
323
ΔAbs. (340 nm) / 10^-3
Time / μs

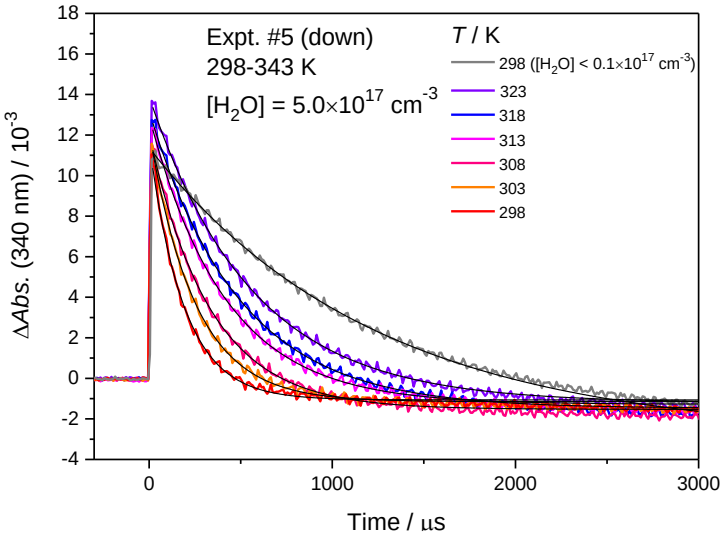
Expt. #5 (down)
298-343 K
[H2O] = 5.0×10^17 cm^-3
T / K
298 ([H2O] < 0.1×10^17 cm^-3)
323
318
313
308
303
298
ΔAbs. (340 nm) / 10^-3
Time / μs

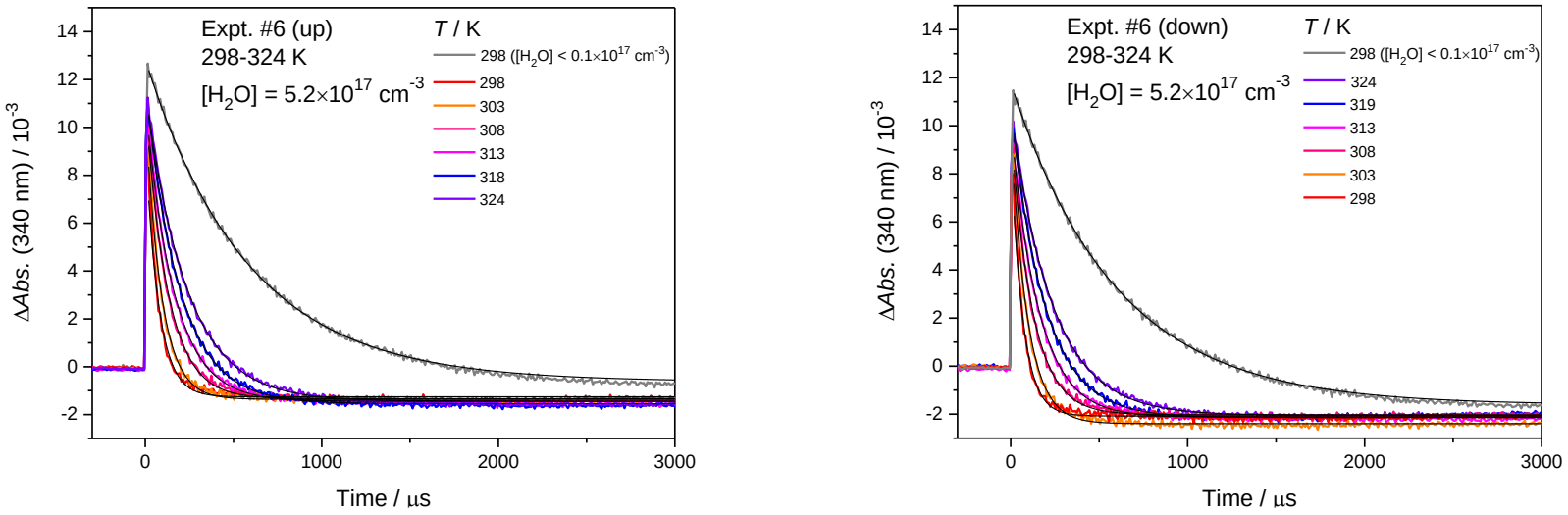

Figure 3B.4. Difference transient absorption traces for Experiments #4, 5, and 6 at different temperatures with constant H_2O concentration. Plots labeled "up" show traces obtained at successively higher temperatures; plots labeled "down" show traces at successively lower temperatures. Black lines are single exponential fits. The average R-squared values of the exponential fits are 0.996, 0.997, and 0.998 for Experiments #2a–2c respectively.

Appendix 3C. Temperature dependence of k_0

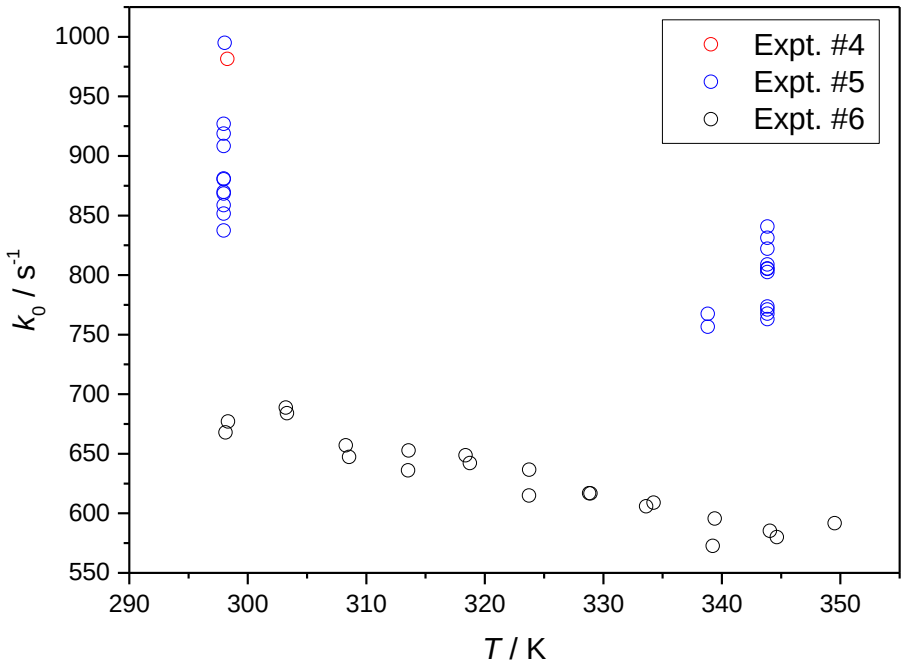

Figure 3C.1. Plot of k_0 (with no H_2O in reactor) at different temperatures for Experiments #4, 5, and 6.

Appendix 3D. Temperature dependence of k_{dimer} in Experiments #4-6

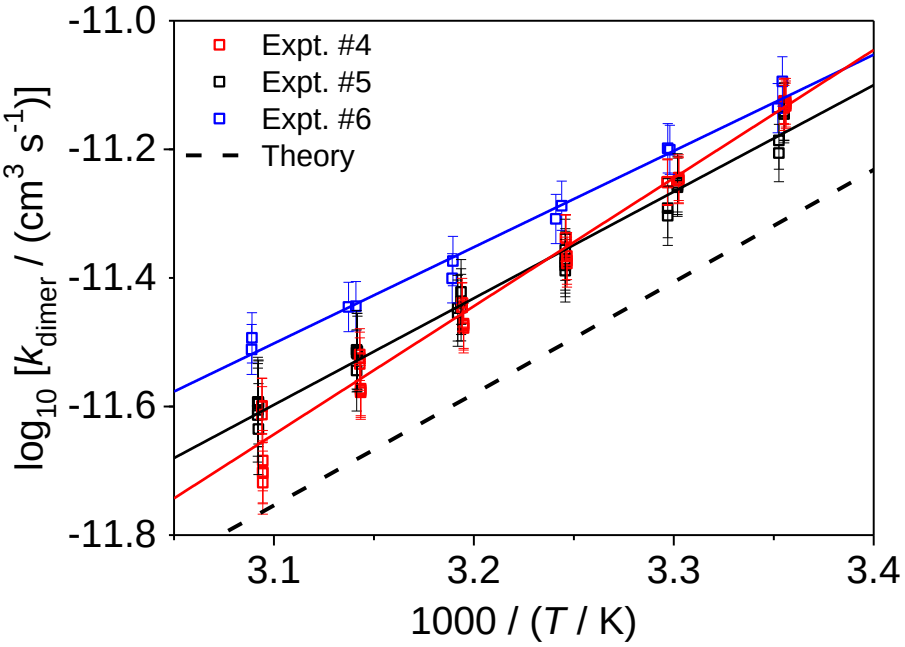

Figure 3D.1. Arrhenius plot of k_{dimer} for Experiments #4, 5, and 6. Solid lines are linear fits to the data from each experiment. Dashed line shows the calculated $k_{dimer}(T)$ (see the published version of this chapter for calculation details).

References

1. Heard, D. E.; Carpenter, L. J.; Creasey, D. J.; Hopkins, J. R.; Lee, J. D.; Lewis, a. C.; Pilling, M. J.; Seakins, P. W.; Carslaw, N.; Emmerson, K. M. High Levels of the Hydroxyl Radical in the Winter Urban Troposphere. *Geophys. Res. Lett.* **2004**, *31*, 1–5, DOI:10.1029/2004GL020544.
2. Emmerson, K. M.; Carslaw, N.; Pilling, M. J. Urban Atmospheric Chemistry during the PUMA Campaign 2: Radical Budgets for OH, HO_2 and RO_2. *J. Atmos. Chem.* **2005**, *52*, 165–183, DOI:10.1007/s10874-005-1323-2.
3. Mauldin III, R. L.; Berndt, T.; Sipilä, M.; Paasonen, P.; Petäjä, T.; Kim, S.; Kurtén, T.; Stratmann, F.; Kerminen, V.-M.; Kulmala, M. A New Atmospherically Relevant Oxidant of Sulphur Dioxide. *Nature* **2012**, *488*, 193–196, DOI:10.1038/nature11278.
4. Ehn, M.; Thornton, J. a; Kleist, E.; Sipilä, M.; Junninen, H.; Pullinen, I.; Springer, M.; Rubach, F.; Tillmann, R.; Lee, B.; et al. A Large Source of Low-Volatility Secondary Organic Aerosol. *Nature* **2014**, *506*, 476–479, DOI:10.1038/nature13032.
5. Berresheim, H.; Adam, M.; Monahan, C.; O'Dowd, C.; Plane, J. M. C.; Bohn, B.; Rohrer, F. Missing SO_2 Oxidant in the Coastal Atmosphere? – Evidence from High Resolution Measurements of OH and Atmospheric Sulfur Compounds. *Atmos. Chem. Phys. Discuss.* **2014**, *14*, 1159–1190, DOI:10.5194/acpd-14-1159-2014.
6. Sarwar, G.; Simon, H.; Fahey, K.; Mathur, R.; Goliff, W. S.; Stockwell, W. R. Impact of Sulfur Dioxide Oxidation by Stabilized Criegee Intermediate on Sulfate. *Atmos. Environ.* **2014**, *85*, 204–214, DOI:10.1016/j.atmosenv.2013.12.013.
7. Suto, M.; Manzanares, E. R.; Lee, L. C. Detection of Sulfuric Acid Aerosols by Ultraviolet Scattering. *Environ. Sci. Technol.* **1985**, *19*, 815–820, DOI:10.1021/es00139a008.
8. Becker, K. H.; Bechara, J.; Brockmann, K. J. Studies on the Formation of H_2O_2 in the Ozonolysis of Alkenes. *Atmos. Environ.* **1993**, *27A*, 57–61, DOI:10.1016/0960-1686(93)90070-F.
9. Leather, K. E.; McGillen, M. R.; Cooke, M. C.; Utembe, S. R.; Archibald, a. T.; Jenkin, M. E.; Derwent, R. G.; Shallcross, D. E.; Percival, C. J. Acid-Yield Measurements of the Gas-Phase Ozonolysis of Ethene as a Function of Humidity Using Chemical Ionisation Mass Spectrometry (CIMS). *Atmos. Chem. Phys.* **2012**, *12*, 469–479, DOI:10.5194/acp-12-469-2012.
10. Newland, M. J.; Rickard, A. R.; Alam, M. S.; Vereecken, L.; Muñoz, A.; Ródenas, M.; Bloss, W. J. Kinetics of Stabilised Criegee Intermediates Derived from Alkene Ozonolysis: Reactions with SO_2, H_2O and Decomposition under Boundary Layer Conditions. *Phys. Chem. Chem. Phys.* **2015**, *17*, 4076–4088, DOI:10.1039/C4CP04186K.
11. Berndt, T.; Voigtländer, J.; Stratmann, F.; Junninen, H.; Mauldin, R. L.; Sipilä, M.; Kulmala, M.; Herrmann, H. Competing Atmospheric Reactions of CH_2OO with SO_2 and Water Vapour. *Phys. Chem. Chem. Phys.* **2014**, *16*, 19130–19136, DOI:10.1039/C4CP02345E.
12. Welz, O.; Savee, J. D.; Osborn, D. L.; Vasu, S. S.; Percival, C. J.; Shallcross, D. E.; Taatjes, C. A. Direct Kinetic Measurements of Criegee Intermediate (CH_2OO) Formed by Reaction of CH_2I with O_2. *Science* **2012**, *335*, 204–207, DOI:10.1126/science.1213229.
13. Taatjes, C. A; Shallcross, D. E.; Percival, C. J. Research Frontiers in the Chemistry of Criegee Intermediates and Tropospheric Ozonolysis. *Phys. Chem. Chem. Phys.* **2014**, *16*, 1704–1718, DOI:10.1039/c3cp52842a.
14. Taatjes, C. A.; Welz, O.; Eskola, A. J.; Savee, J. D.; Scheer, A. M.; Shallcross, D. E.; Rotavera, B.; Lee, E. P. F.; Dyke, J. M.; Mok, D. K. W.; et al. Direct Measurements of

Conformer-Dependent Reactivity of the Criegee Intermediate CH_3CHOO. *Science.* **2013**, *340*, 177–180, DOI:10.1126/science.1234689.
15. Su, Y.-T.; Lin, H.-Y.; Putikam, R.; Matsui, H.; Lin, M. C.; Lee, Y.-P. Extremely Rapid Self-Reaction of the Simplest Criegee Intermediate CH_2OO and Its Implications in Atmospheric Chemistry. *Nat. Chem.* **2014**, *6*, 477–483, DOI:10.1038/nchem.1890.
16. Su, Y.-T.; Huang, Y.-H.; Witek, H. A.; Lee, Y.-P. Infrared Absorption Spectrum of the Simplest Criegee Intermediate CH_2OO. *Science* **2013**, *340*, 174–176, DOI:10.1126/science.1234369.
17. Ting, W.-L.; Chen, Y.-H.; Chao, W.; Smith, M. C.; Lin, J. J.-M. The UV Absorption Spectrum of the Simplest Criegee Intermediate CH_2OO. *Phys. Chem. Chem. Phys.* **2014**, *16*, 10438–10443, DOI:10.1039/c4cp00877d.
18. Beames, J. M.; Liu, F.; Lu, L.; Lester, M. I. Ultraviolet Spectrum and Photochemistry of the Simplest Criegee Intermediate CH_2OO. *J. Am. Chem. Soc.* **2012**, *134*, 20045–20048, DOI:10.1021/ja310603j.
19. Sheps, L. Absolute Ultraviolet Absorption Spectrum of a Criegee Intermediate CH_2OO. *J. Phys. Chem. Lett.* **2013**, *4*, 4201–4205, DOI:10.1021/jz402191w.
20. Smith, M. C.; Ting, W.-L.; Chang, C.-H.; Takahashi, K.; Boering, K. A.; Lin, J. J.-M. UV Absorption Spectrum of the C2 Criegee Intermediate CH_3CHOO. *J. Chem. Phys.* **2014**, *141*, 074302, DOI:10.1063/1.4892582.
21. Liu, F.; Beames, J. M.; Green, A. M.; Lester, M. I. UV Spectroscopic Characterization of Dimethyl- and Ethyl-Substituted Carbonyl Oxides. *J. Phys. Chem. A* **2014**, *118*, 2298–2306, DOI:10.1021/jp412726z.
22. Nakajima, M.; Endo, Y. Communication: Determination of the Molecular Structure of the Simplest Criegee Intermediate CH_2OO. *J. Chem. Phys.* **2013**, *139*, DOI:10.1063/1.4821165.
23. Stone, D.; Blitz, M.; Daubney, L.; Howes, N. U. M.; Seakins, P. Kinetics of CH_2OO Reactions with SO_2, NO_2, NO, H_2O and CH_3CHO as a Function of Pressure. *Phys. Chem. Chem. Phys.* **2014**, *16*, 1139–1149, DOI:10.1039/c3cp54391a.
24. Buras, Z. J.; Elsamra, R. M. I.; Jalan, A.; Middaugh, J. E.; Green, W. H. Direct Kinetic Measurements of Reactions between the Simplest Criegee Intermediate CH_2OO and Alkenes. *J. Phys. Chem. A* **2014**, *118*, 1997–2006, DOI:10.1021/jp4118985.
25. Welz, O.; Eskola, A. J.; Sheps, L.; Rotavera, B.; Savee, J. D.; Scheer, A. M.; Osborn, D. L.; Lowe, D.; Murray Booth, A.; Xiao, P.; et al. Rate Coefficients of C1 and C2 Criegee Intermediate Reactions with Formic and Acetic Acid near the Collision Limit: Direct Kinetics Measurements and Atmospheric Implications. *Angew. Chemie - Int. Ed.* **2014**, *53*, 4547–4550, DOI:10.1002/anie.201400964.
26. Ouyang, B.; McLeod, M. W.; Jones, R. L.; Bloss, W. J. NO_3 Radical Production from the Reaction between the Criegee Intermediate CH_2OO and NO_2. *Phys. Chem. Chem. Phys.* **2013**, *15*, 17070 DOI: 10.1039/C3CP53024H.
27. Chao, W.; Hsieh, J.; Chang, C.; Lin, J. J. Direct Kinetic Measurement of the Reaction of the Simplest Criegee Intermediate with Water Vapor. *Science* **2015**, *347*, 751–754, DOI:10.1126/science.1261549.
28. Lewis, T. R.; Blitz, M. a.; Heard, D. E.; Seakins, P. W. Direct Evidence for a Substantive Reaction between the Criegee Intermediate, CH_2OO, and the Water Vapour Dimer. *Phys. Chem. Chem. Phys.* **2015**, *17*, 4859–4863, DOI:10.1039/C4CP04750H.
29. Su, M.-N.; Lin, J. J.-M. Note: A Transient Absorption Spectrometer Using an Ultra Bright Laser-Driven Light Source. *Rev. Sci. Instrum.* **2013**, *84*, 086106, DOI:10.1063/1.4818977.
30. Ruscic, B. Active Thermochemical Tables: Water and Water Dimer. *J. Phys. Chem. A* **2013**, *117*, 11940–11953, DOI:10.1021/jp403197t.

31. Ting, W.-L.; Chang, C.-H.; Lee, Y.-F.; Matsui, H.; Lee, Y.-P.; Lin, J. J.-M. Detailed Mechanism of the $CH_2I + O_2$ Reaction: Yield and Self-Reaction of the Simplest Criegee Intermediate CH_2OO. *J. Chem. Phys.* **2014**, *141*, 104308, DOI:10.1063/1.4894405.
32. Sheps, L.; Scully, A. M.; Au, K. UV Absorption Probing of the Conformer-Dependent Reactivity of a Criegee Intermediate CH_3CHOO. *Phys. Chem. Chem. Phys.* **2014**, *16*, 26701–26706, DOI:10.1039/C4CP04408H.
33. Ryzhkov, A. B.; Ariya, P. A. A Theoretical Study of the Reactions of Parent and Substituted Criegee Intermediates with Water and the Water Dimer. *Phys. Chem. Chem. Phys.* **2004**, *6*, 5042, DOI:10.1039/b408414d.
34. Lovejoy, E. R.; Hanson, D. R.; Huey, L. G. Kinetics and Products of the Gas-Phase Reaction of SO_3 with Water. *J. Phys. Chem.* **1996**, *100*, 19911–19916, DOI:10.1021/jp962414d.
35. Kolb, C. E.; Jayne, J. T.; Worsnop, D. R.; Molina, M. J.; Meads, R. F.; Viggiano, A. A. Gas Phase Reaction of Sulfur Trioxide with Water Vapor. *J. Am. Chem. Soc.* **1994**, *116*, 10314–10315, DOI:10.1021/ja00101a067.
36. Jayne, J. T.; Pöschl, U.; Chen, Y.; Dai, D.; Molina, L. T.; Worsnop, D. R.; Kolb, C. E.; Molina, M. J. Pressure and Temperature Dependence of the Gas-Phase Reaction of SO_3 with H_2O and the Heterogeneous Reaction of SO_3 with H_2O/H_2SO_4 Surfaces. *J. Phys. Chem. A* **1997**, *101*, 10000–10011, DOI:10.1021/jp972549z.
37. Larson, L. J.; Kuno, M.; Tao, F.-M. Hydrolysis of Sulfur Trioxide to Form Sulfuric Acid in Small Water Clusters. *J. Chem. Phys.* **2000**, *112*, 8830, DOI:10.1063/1.481532.

Chapter 4

Unimolecular decomposition rate of the Criegee intermediate $(CH_3)_2COO$ measured directly with UV absorption spectroscopy

Adapted with permission of all coauthors from Smith, M. C.; Chao, W.; Takahashi, K.; Boering, K. A.; Lin, J. J.-M.; *J. Phys. Chem. A.* **2016**, *120* (27), 4789-4798, Piergiorgio Casavecchia and Antonio Lagana Festschrift special issue, DOI: 10.1021/acs.jpca.5b12124.

4.1 Introduction

The reaction of olefins with ozone in the atmosphere (*i.e.*, alkene ozonolysis) can produce stabilized carbonyl oxides known as Criegee intermediates (CIs) with substantial yields. The stabilized CI may then undergo several different reactions in the atmosphere, including (i) reaction with water or water dimer,[1–3] (ii) reaction with other atmospheric trace species such as SO_2,[4–6] and (iii) thermal decomposition.[7,8] Several studies have indicated that reactions of CIs may be a significant source of atmospheric OH under low light conditions and may contribute to H_2SO_4 formation.[9–12] Due to the short atmospheric lifetime of CIs, concentrations of atmospheric CIs cannot yet be measured directly and can only be estimated from known formation and removal rates. In particular, accurate determination of the rates of CI removal by different reactions is important to understand the impact of CIs on atmospheric chemistry and climate, especially their influence on HO_x production and aerosol formation.

Many laboratory investigations of alkene ozonolysis have measured reaction rates of CIs by monitoring the formation of CI reaction products (an "indirect" method of measuring CI kinetics); the resulting reported rate coefficients are often inconsistent with theoretical predictions, such as those for the reactions of CH_2OO with water and with SO_2.[13] Indirect measurements of CIs formed from alkene ozonolysis are susceptible to uncertainties in the ozonolysis mechanism, the yields and types of CIs formed, and interferences from byproducts. To address this issue, a simple method of preparing CIs for direct laboratory detection and kinetic measurements was recently reported.[14] In this scheme, a diiodoalkane precursor is photolyzed by ultraviolet light in the presence of O_2, leading to substitution of the iodine atom in the resulting iodoalkyl radical with O_2 to form the corresponding Criegee intermediate ($R_2CI_2 + h\upsilon \rightarrow R_2CI + I$; $R_2CI + O_2 \rightarrow R_2COO + I$, where R is a hydrogen atom or alkyl group). A number of studies have demonstrated the utility of this scheme for obtaining accurate reaction rate coefficients and absorption and action spectra; recent reviews have covered the range of investigations in detail.[15,16]

Some important insights have been obtained from these more recent direct CI measurements. First, the reaction rates between SO_2 and simple CIs (CH_2OO, CH_3CHOO, $(CH_3)_2COO$) were found to be orders of magnitude faster than previously reported rates from the indirect ozonolysis studies;[14,17–19] the fast rates suggest that CIs may efficiently oxidize SO_2 in the atmosphere, which may account for the observed "missing oxidant" contributing to atmospheric H_2SO_4.[11] Second, CH_2OO and other simple CIs were found to absorb strongly in the near-UV region.[20–24] Although estimates of effective loss rates of CIs in the atmosphere showed that UV photolysis cannot compete with unimolecular or bimolecular reactions,[22–24] the strong absorption in the 300-400 nm spectral region has enabled transient spectroscopic studies of the kinetics of bimolecular CI

reactions.[25–27] Several recent investigations revealed that the reaction between CH_2OO and water dimer is fast and should dominate the loss of CH_2OO in the troposphere.[28–30] Finally, systematic investigations of CI kinetics confirmed theoretical predictions that the bimolecular CI reaction rates are highly dependent on the CI structure.[18,19,28,31,32] Notably, the dimethyl-substituted CI, $(CH_3)_2COO$, showed a substantially slower reaction rate with water vapor than CH_2OO and an extremely fast reaction rate with SO_2.[19] This finding suggests that $(CH_3)_2COO$ and CIs with similar structures may survive high humidity in the atmosphere and may react rapidly enough with SO_2 to play a role in the atmospheric oxidation of SO_2; however, to estimate the steady-state concentrations of CIs in the atmosphere, accurate determinations of their thermal decomposition rates are needed.[19]

A number of recent studies have yielded estimates of the decomposition rates of Criegee intermediates. In the case of CH_2OO, experimental and theoretical determinations have indicated a very small rate coefficient for unimolecular decomposition of $< 0.5\ s^{-1}$ (Refs. 27,33–35); the slow rate is attributed to a high energetic barrier to O-O ring closure forming dioxirane, which is the most favorable decomposition channel for CH_2OO and Criegee intermediates with *anti* conformations.[36] However, CIs with a methyl group in the *syn* position such as *syn*-CH_3CHOO and $(CH_3)_2COO$ are expected to follow a different decomposition pathway involving the more facile hydrogen transfer from the *syn* methyl group to the terminal oxygen to form vinyl hydroperoxide, which may subsequently decompose to form OH radical.[36–38]

Studies of tetramethylethylene (TME) ozonolysis[6,39,40] yielded a larger thermal decomposition rate coefficient, k_d, for $(CH_3)_2COO$ of 3 to $6\ s^{-1}$. In addition, similar ozonolysis experiments determined k_d for $(CH_3)_2COO$ relative to that for its reaction with SO_2; [34,41] the reported ratios, k_d/k_{SO2}, fall within the range of $(2 \text{ to } 8)\times10^{12}\ cm^{-3}$. However, if the relative rates k_d/k_{SO2} are combined with the values of k_{SO2} determined in direct studies for CH_2OO ($\sim4\times10^{-11}\ cm^3s^{-1}$)[14] and CH_3CHOO ($\sim2\text{-}20\times10^{-11}\ cm^3s^{-1}$)[18,32] as well as the value of $1.32\times10^{-10}\ cm^3s^{-1}$ for $(CH_3)_2COO$,[19] much higher values of k_d ($\sim10^2\ s^{-1}$) would result.

Typically, procedures for determining k_{SO2} in direct detection experiments and k_d/k_{SO2} in ozonolysis experiments are less complex than those for determining k_d in ozonolysis experiments. Hence, k_d may need further investigations. In this work, we present the first determination of the unimolecular reaction rate coefficient, k_d, from direct detection of $(CH_3)_2COO$ and $(CD_3)_2COO$ using time-resolved UV absorption spectroscopy at temperatures from 283 K to 323 K, and compare the results with theoretical calculations to reveal insights into the unimolecular decomposition mechanism.

4.2 Experimental methods

The Criegee intermediate $(CH_3)_2COO$ was produced in a flow tube (76 cm long, 20 mm inner diameter) immersed in a water circulation tank with windows on each end. Time-resolved UV absorption was measured with light from a continuous-wave laser-driven plasma light source (Energetiq, EQ-99) which was projected into the entrance window by an achromatic lens; a right-angle SiO_2 prism and a spherical mirror were used to achieve a multiple pass configuration inside

the flow tube, increasing the absorption path length to eight times the length of the tube. Upstream of the flow tube, carrier gas N_2 was mixed with O_2 and passed through a container of liquid $(CH_3)_2CI_2$ heated to ~303 K. The $(CH_3)_2CI_2$ sample was synthesized using a procedure described previously[19,24,42] and its identity was confirmed using a residual gas analyzer and proton-NMR spectroscopy; the sample purity was about 85 to 95%, varying with different batches of synthesis and purification. To ensure that impurities in the sample did not affect our determination of the unimolecular rates, we performed experiments in which the concentration of $(CH_3)_2CI_2$ was varied (see Section 4.3 for more details).

The flow rate of each gas was controlled with mass flow controllers (Brooks, 5850E or 5800E). The total flow rate was typically ~3000 sccm (standard cubic centimeters per minute) for a total pressure of 200 Torr inside the reactor (10 Torr O_2). A reactor pressure of 200 Torr produces the most stable flow conditions for the apparatus in this work, and the unimolecular reaction rate at 200 Torr is already at the high-pressure limit (see Section 4.3). The mixture of N_2, O_2 and $(CH_3)_2CI_2$ vapor passed through another absorption cell (75.3 cm long, 12 mm diameter) where the absorption of $(CH_3)_2CI_2$ (or SO_2 in some experiments) was monitored with a D_2 lamp (Ocean Optics D-2000) and a UV spectrometer (Ocean Optics, Maya2000 Pro). Downstream of this cell, the gas mixture passed through ~1 m of copper tubing immersed in the same water bath to preheat (or precool) the gases before entering the flow reactor. The mixture entered the tube through a gas inlet at the center and exited through outlets to a vacuum pump at each end. A portion of pure N_2 gas flow was directed into each end of the tube to purge the inside of the windows from possible contamination by photochemical products. For experiments below room temperature, an additional flow of pure N_2 was used to purge the outer surfaces of the windows to prevent condensation of ambient water vapor.

To produce $(CH_3)_2COO$, a 248 nm pulsed KrF excimer laser was focused into the flow reactor, inducing photolysis of $(CH_3)_2CI_2$ and subsequent formation of the Criegee intermediate. The pulse rate of the laser was typically 1.04 Hz, and a total flow rate was used that was high enough to refresh the gas mixture between laser shots. The UV absorption spectrum of $(CH_3)_2COO$ has been reported[19,24] and features a strong absorption band from 300-360 nm. Here, the $(CH_3)_2COO$ absorption was monitored at 340 nm, where interference from the absorption of the IO byproducts is negligible.[19] A 340 nm band pass filter (Edmund Optics, 65129, 10-nm OD4 band pass filter) and a balanced photodiode detector (Thorlabs, PDB450A) were used to collect the probe light exiting the tube. Although $(CH_3)_2CI_2$ also absorbs light near 340 nm, its concentration change can be considered a step function in time due to pulsed photolysis, and $(CH_3)_2CI$ would be converted to $(CH_3)_2COO$ in the first few μs such that it would not affect the kinetic measurement of $(CH_3)_2COO$ (with a lifetime of a few ms). The above arguments have been shown to be valid in previous experiments using this apparatus.[19,28,30]

The temperature of the gases inside the flow tube was controlled with a temperature-controlled circulating water bath (Yih-Der, BL-730) connected to the water circulation tank. Readings were taken periodically throughout each experiment from three resistance temperature detectors (RTDs) located in glass wells extending several mm into the top of the tube at the left, center, and right positions. Each RTD was calibrated prior to the experiment against a precision sensor (Rotronic HC2-S, ±0.1 K accuracy) placed inside the reactor to measure the temperature of the gas mixture, assuming a linear relationship between the Rotronic and RTD sensor outputs. Due to the

uncertainty in this calibration, as well as temperature variations along the length of the flow path and slight inhomogeneity in the temperature of the water in the top and bottom of the tank, the overall temperature uncertainty is estimated to be ±0.5 K.

The time-resolved absorption was recorded with a digital oscilloscope which averaged the signal from at least 120 photolysis laser shots. The absorption signal was typically measured from -25 ms to 25 ms, where the laser pulse is defined as time 0; the baseline absorption prior to the photolysis pulse is subtracted from the signal to account for the constant contribution to the absorption from $(CH_3)_2CI_2$. (This leads to the negative baseline observed at long times in the absorption traces in Figures 4.1a-d, as explained further in Section 4.3.) The absorption baseline exhibits a low-frequency oscillation (*i.e.*, much longer timescale than the experimental timescale, such that its behavior is approximately linear within 10 ms) with an amplitude that intensifies at higher temperatures (due to the convection of air and the gas flow). To account for this fluctuation, in some cases the baseline from -10 ms to 0 ms was fit to a linear expression which was subtracted from the signal during data analysis. The absorption signal increased slightly after the laser shot even with no $(CH_3)_2CI_2$ added to the gas mixture; this time-dependent absorption change was found to be correlated with the laser pulse energy and independent of the chemistry in the flow tube.[19,28,30] Therefore, a background signal (without adding $(CH_3)_2CI_2$) was recorded at the beginning and end of data collection for each laser pulse energy and subtracted from the $(CH_3)_2COO$ absorption signal during analysis.

To measure the transient absorption of the isotopically-substituted CI, $(CD_3)_2COO$, the precursor $(CD_3)_2CI_2$ was synthesized using the same procedure as for $(CH_3)_2CI_2$ using deuterated acetone as the starting reagent. For experiments measuring the transient absorption of CH_2OO, commercial CH_2I_2 was used (Acros Organics, 99+%). To determine the reaction rate coefficient of $(CH_3)_2COO$ with SO_2, we measured the transient absorption of $(CH_3)_2COO$ with various concentrations of SO_2 (the flow of SO_2 was adjusted between 0 and 1 sccm with a mass flow controller) added to the $N_2/O_2/(CH_3)_2CI_2$ gas mixture. As shown previously,[19,22] neither SO_2 nor its potential reaction products (*e.g.*, SO_3) are expected to interfere with the absorption at 340 nm. For the SO_2 experiments, the total pressure in the reactor was 300 Torr to ensure that the reaction rate coefficients were determined in the high-pressure limit (see Ref. 19).

4.3 Results and discussion

4.3.1 Determination of k_d from the time-resolved absorption of $(CH_3)_2COO$

Table 4.1 provides a list of all experiments performed in this work with corresponding conditions. Representative time traces of the absorbance change at 340 nm for several different initial concentrations of $(CH_3)_2COO$ are shown in Figures 4.1a-d for 283 K, 298 K, 310 K, and 323 K. $[(CH_3)_2COO]_0$ was varied by modifying $[(CH_3)_2CI_2]_0$ as well as the laser pulse energy (typically from 6 to 18 mJ); both of these parameters are linearly proportional to the amount of $(CH_3)_2COO$ formed. The absorption signal was then used with the estimated absorption path length and cross section (1.6×10^{-17} cm^2 at 340 nm)[43] to quantify $[(CH_3)_2COO]$ for each absorption trace. As mentioned in Section 4.2, the slightly negative baseline at long times is attributed to depletion of

$(CH_3)_2CI_2$ by the photolysis pulse. Previous work in our laboratory[19] measuring the UV spectroscopy and kinetics of $(CH_3)_2COO$ has demonstrated that the absorption at 340 nm is a good probe of the concentration of $(CH_3)_2COO$ in the $(CH_3)_2CI_2/O_2$ photolysis system. As shown in Figure 4.1, the sharp increase in absorption after time zero is clear evidence of $(CH_3)_2COO$ formation and the decay rate of $[(CH_3)_2COO]$ is faster at higher $[(CH_3)_2COO]_0$. (See Appendix 4A for representative time traces of all experiments.)

The observed decay of $(CH_3)_2COO$ in this system may include contributions from the following processes: (i) thermal decomposition; (ii) reaction with other reactive species such as iodine atoms and other $(CH_3)_2COO$ radicals; and (iii) loss due to decomposition on the tube walls. To account for these processes, equation (1) is used to describe the loss of $(CH_3)_2COO$.

1. $$-\frac{d[(CH_3)_2COO]}{dt} = k_d[(CH_3)_2COO] + 2k_{self}[(CH_3)_2COO]^2 + k_{rad}[X_{rad}][(CH_3)_2COO] + k_{wl}[(CH_3)_2COO]$$
$$= (k_d + k_{wl} + 2k_{self}[(CH_3)_2COO] + k_{rad}[X_{rad}])[(CH_3)_2COO]$$

In equation (1), k_d is the unimolecular decomposition rate coefficient; k_{self} is the rate coefficient for the self-reaction $(CH_3)_2COO + (CH_3)_2COO$; $[X_{rad}]$ refers to the total concentration of reactive species (such as I atoms and OH radicals) contributing to the bimolecular loss, with a combined rate coefficient k_{rad};[19,44] and a term k_{wl} is included to account for the wall loss. The kinetic expression in equation (1) can be represented as a combination of first and second order terms, as in equation (2).

2. $$-\frac{d[(CH_3)_2COO]}{dt} = k_1[(CH_3)_2COO] + k_2[(CH_3)_2COO]^2$$

In equation (2), k_1 is the sum of k_d, k_{wl}, and $k_{rad}[X_{rad}]_e$ ($[X_{rad}]_e$ is the effective radical concentration at long times) and the k_2 term includes $(CH_3)_2COO$ self-reaction and $(CH_3)_2COO + X_{rad}$ (with the effective time-dependent concentration of $[X_{rad}]$-$[X_{rad}]_e$). We refer to equation (2) as Model A. Solving the differential equation of Model A yields the expression for $[(CH_3)_2COO]$ in equation (3).

3. $$[(CH_3)_2COO]_t = [(CH_3)_2COO]_0 \frac{(1+\frac{k_2[(CH_3)_2COO]_0}{k_1})^{-1}e^{-k_1t}}{1-(1+\frac{k_1}{k_2[(CH_3)_2COO]_0})^{-1}e^{-k_1t}}$$

The expression in equation (3) was used to fit the absorption traces; the resulting fits are shown as black lines in Figures 4.1a-d. To obtain reliable values for k_1 and k_2, the absorption traces at the highest $[(CH_3)_2COO]_0$ were fit first, since these have good signal-to-noise ratio and the largest second order contribution, and thus the most accurate value of k_2 could be obtained. Then, all of the absorption traces were fit simultaneously with k_2 fixed at the average value obtained from the higher concentration fits.

Table 4.1. List of experiments performed in this work.

Exp. #	Precursor	T (K)	P_{tot} (Torr)	P_{O2} (Torr)	Gas
1a	$(CH_3)_2CI_2$	283.4	200.1	6.6 or 9.7	N_2
1b	$(CH_3)_2CI_2$	285.3	200.1	9.7	N_2
1c	$(CH_3)_2CI_2$	293.3	200.1	9.6	N_2
1d	$(CH_3)_2CI_2$	298.5	200.3	9.7	N_2
1d-2	$(CH_3)_2CI_2$	298.2	200.2	10.1	N_2
1e	$(CH_3)_2CI_2$	310.2	200.1	9.9	N_2
1e-2	$(CH_3)_2CI_2$	310.1	200.1	9.9	N_2
1f	$(CH_3)_2CI_2$	323.2	200.4	9.8	N_2
2a	$(CH_3)_2CI_2$	298.6	200.1	9.7	N_2
2b	$(CH_3)_2CI_2$	298.5	100.1	9.6	N_2
3a	$(CD_3)_2CI_2$	283.2	200.0	9.7	N_2
3b	$(CD_3)_2CI_2$	298.5	200.1	9.8	N_2
3b-2	$(CD_3)_2CI_2$	298.5	200.1	9.7	N_2
3c	$(CD_3)_2CI_2$	310.3	200.1	9.8	N_2
3c-2	$(CD_3)_2CI_2$	310.0	200.0	9.9	N_2
3d	$(CD_3)_2CI_2$	323.2	200.0	9.9	N_2
4a	$(CD_3)_2CI_2$	298.4	200.0	9.8	N_2
4b	$(CD_3)_2CI_2$	298.4	100.0	9.8	N_2
5a	$(CH_3)_2CI_2$	282.8	300.1	9.8	N_2/SO_2
5a-2	$(CH_3)_2CI_2$	283.2	300.0	9.7	N_2/SO_2
5b	$(CH_3)_2CI_2$	293.0	300.0	9.8	N_2/SO_2
5b-2	$(CH_3)_2CI_2$	293.1	300.1	9.7	N_2/SO_2
5c	$(CH_3)_2CI_2$	302.9	300.0	9.8	N_2/SO_2
5c-2	$(CH_3)_2CI_2$	302.7	300.0	9.7	N_2/SO_2
6a	CH_2I_2	298.4	200.1	9.9	N_2
6b	CH_2I_2	298.0	200.0	9.3	N_2
6c	CH_2I_2	298.0	200.1	93.6	N_2/O_2
6d	CH_2I_2	297.9	200.1	187.0	O_2
6e	CH_2I_2	298.1	199.9	8.8	N_2

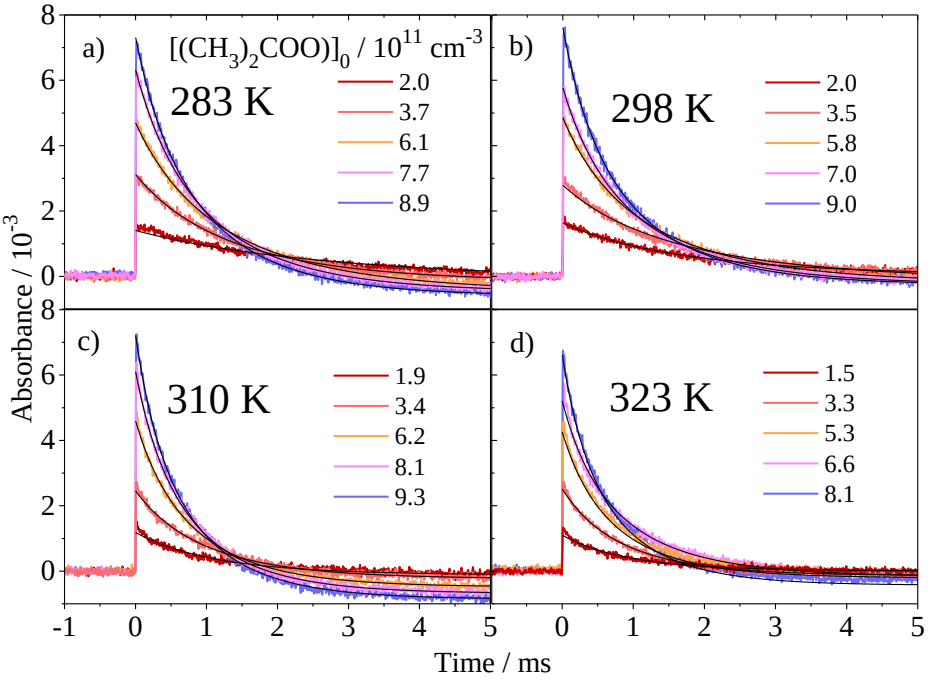

Figure 4.1. Difference absorbance traces at 340 nm showing $(CH_3)_2COO$ formation and decay (photolysis at time zero) for various initial $(CH_3)_2COO$ concentrations (in units of 10^{11} cm^{-3}; color coded as indicated in the legends) at (a) 283 K, (b) 298 K, (c) 310 K, and (d) 323 K. Smooth black curves are the fits to model A.

Figures 4.2a-d show the resulting values of k_1 and k_2 from Model A (see Section 4.3.2 for a discussion of Model B). The value of k_2 is related to $k_{rad}([X_{rad}]-[X_{rad}]_e)/[(CH_3)_2COO] + 2k_{self}$; to assess these resulting k_2 values, one can make the following approximations. If the yield of $(CH_3)_2COO$ is unity in the photolysis system, then the initial concentration of I atoms, $[I]_0$, will be equal to $2[(CH_3)_2COO]_0$. In reality, the $(CH_3)_2COO$ yield should be less than unity (our group has estimated a yield of 40% at 100 Torr)[19] and X_{rad} may include other species such as OH radicals in addition to I atoms, such that $[X_{rad}]_0$ is likely ~$5[(CH_3)_2COO]_0$ or greater. Assuming $[X_{rad}]_0 = 5[(CH_3)_2COO]_0$ and a value of 1×10^{-10} cm^3 s^{-1} for k_{self} (a reasonable estimate considering values of $(0.4\text{-}6)\times10^{-10}$ cm^3 s^{-1} have been reported[44–46] for the CH_2OO self-reaction), the resulting k_{rad} derived from the value of k_2 at 298 K in Figure 4.2b is on the order of 10^{-10} cm^3 s^{-1}, similar to the rate coefficient of $\leq9\times10^{-11}$ cm^3 s^{-1} derived for the reaction CH_2OO + I by Ting *et al.*[44] Therefore, the above result seems reasonable, especially considering that the concentration and identity of X_{rad} are not well known, and that other radical-radical reactions would also contribute to k_{rad}.

The intercepts of the linear fits in Figures 4.2a-d give the values of $k_{zc} = k_d + k_{wl}$ at each temperature. The value for k_{zc} varies strongly with temperature, ranging from ~300 s^{-1} at 283 K to ~900 s^{-1} at 323 K. To estimate the contribution from k_{wl}, we performed similar experiments using CH_2I_2 to

form CH_2OO in the same flow tube under the same gas flow rates. The results are shown in Figure 4.3; the intercept of the linear fit is around 30 s^{-1}. The thermal decomposition rate coefficient for CH_2OO is thought to be very small, likely <0.5 s^{-1}.[27,33–35] Assuming that $k_{wl} >> k_d$ for CH_2OO and that the rate of wall loss for CH_2OO is not significantly different from that for $(CH_3)_2COO$, we deduced values of k_d for $(CH_3)_2COO$ using $k_d = k_{zc} - k_{wl}$ for each experiment. The results are listed in Table 4.2 (see Section 4.3.4 for a discussion of k_d of $(CD_3)_2COO$).

4.3.2. Additional analysis and precursor contributions to k_d

In the following paragraphs, we describe two additional models used to analyze the observed loss rate of $(CH_3)_2COO$. The results provide some insight into the contribution of the second-order kinetics, as well as that of the synthesized precursor $(CH_3)_2CI_2$, to the derived k_d values.

Although Model A can fit the experimental absorption traces when the second order contribution is large, it is difficult to partition the k_1 and k_2 terms when the signal-to-noise ratio is low, which often leads to unphysical fit (the value of k_1 becomes too large when the value of k_2 is too small or vice versa). Accordingly, we tested the use of a single exponential function of the form $A(t) = A_0 e^{-k_{obs}t}$ to analyze the data. The resulting fits are shown in Appendix 4B. This simple form fits the absorption profiles reasonably well, although the observed absorbance (proportional to $[(CH_3)_2COO]$) can be a bit higher than the model prediction at short kinetic times (< 0.25 ms after laser pulse), especially for high $[(CH_3)_2COO]_0$. For example, in Appendix 4B the observed maximum absorbance at 298 K is $\sim 7.7 \times 10^{-3}$ for the highest $[(CH_3)_2COO]_0$, but the single exponential model predicts a maximum absorbance of about 7×10^{-3}. This difference indicates there is some contribution from second-order kinetics. To evaluate whether neglecting the second-order contribution causes a significant change in k_{zc}, we used a simplified model (referred to as Model B) in which the term $2k_{self}[(CH_3)_2COO] + k_{rad}[X_{rad}]$ is approximated as a constant $k_{eff}[X]$, as in equation (4).

4. $$-\frac{d[(CH_3)_2COO]}{dt} \cong (k_{zc} + k_{eff}[X])[(CH_3)_2COO] = k_{obs}[(CH_3)_2COO] \text{ where } k_{zc} = k_d + k_{wl}$$

Figures 4.2a-d show the plots of k_1 obtained from Model A and k_{obs} obtained from Model B at various $[(CH_3)_2COO]_0$. Due to the contribution of the k_2 term, the k_1 values from Model A are smaller than the k_{obs} values from Model B. In addition, a linear relationship with respect to $[(CH_3)_2COO]_0$ was observed for both models, suggesting that $[X_{rad}]_e$ in Model A or [X] in Model B is proportional to $[(CH_3)_2COO]_0$. This is expected since most of the reactive species should be formed in concentrations proportional to $[(CH_3)_2CI_2]_0$ and the laser pulse energy (assuming there are no reactive species in the precursor mixture; see below for further discussion) – *i.e.*, they are also proportional to the initial concentration of the Criegee intermediate, $[X] \propto [(CH_3)_2COO]_0$. In Models A and B, the extrapolation of k_1 (k_{obs}) to zero $[(CH_3)_2COO]_0$ would remove the contributions of the bimolecular processes, which are proportional to $[(CH_3)_2COO]_0$. The intercept k_{zc} would contain the contributions of the unimolecular decomposition k_d and a term k_{wl} to account for the wall loss. While Model A gives better fits to the absorption traces as expected, the k_{zc} values from both models are essentially the same. (See the published version of this chapter for a comparison of k_{zc} obtained from both models, and for a comparison of Models A and B for $(CD_3)_2COO$.) Although the discussion in this work primarily concerns analysis of the data using Model A, for some data sets with lower signal-to-noise ratios, the reliable determination of k_1 and

k_2 becomes difficult; hence, the simpler Model B with its single parameter k_{obs} remains useful for extracting k_{zc} from the data in these cases.

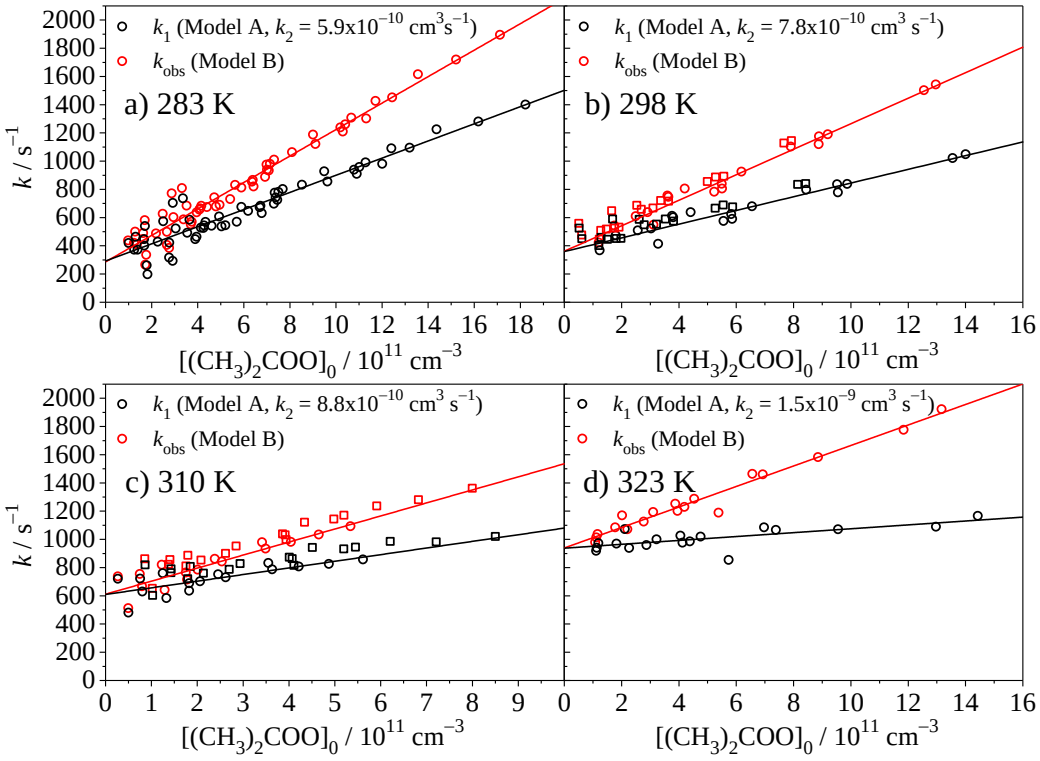

Figure 4.2. Comparison of k_1 obtained from Model A (with fixed k_2) and k_{obs} obtained from Model B as a function of $[(CH_3)_2COO]_0$ for a) 283 K, b) 298 K, c) 310 K, and d) 323 K. Different symbols represent experiments performed on different days for the same temperature. Lines represent the linear fits.

As mentioned in Section 4.2, an additional analysis was performed to verify that the precursor $(CH_3)_2CI_2$ or $(CD_3)_2CI_2$ and impurities do not affect the determination of k_{zc} (and therefore the determination of k_d, as discussed below). In this analysis (referred to here as Model A-p), we fit k_1 obtained from Model A to the expression in equation (5) to determine k_{zc}, k_{eff}^{C} (effective loss rate coefficient due to reactions of species with concentrations proportional to the CI), and k_{eff}^{P} (effective loss rate coefficient due to reactions of species with concentrations proportional to the precursor).

5. $$k_1 = k_{zc} + k_{eff}^{C}[(CH_3)_2COO]_0 + k_{eff}^{P}[(CH_3)_2CI_2]$$

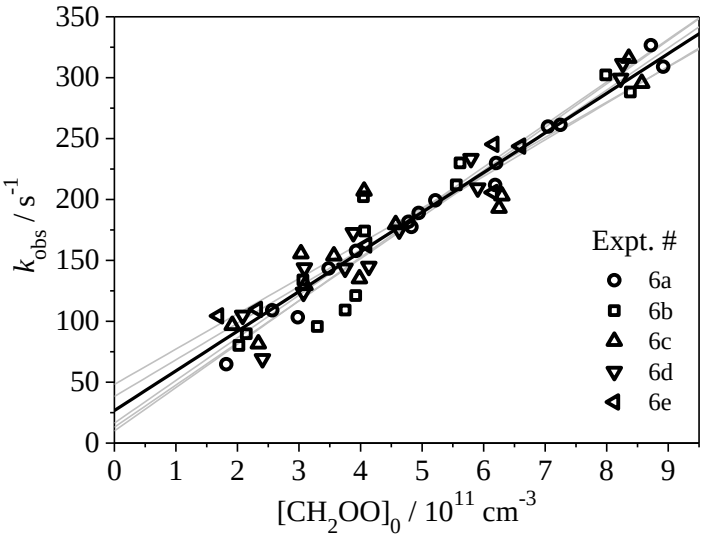

Figure 4.3. Effective loss rate k_{obs} (obtained with Model B) of CH_2OO at different initial CH_2OO concentrations for Experiment #6. Light gray lines are linear fits to each experiment; black line is a linear fit to all experiments.

The results are shown in Appendix 4C and Table 4.3. (See Section 4.3.4 for a discussion of k_d of $(CD_3)_2COO$). The fitted values of k_{eff}^{C} range from ~(3 to 7)×10^{-10} cm^3 s^{-1}, and k_{eff}^{P} ranges from ~(−3 to 4)×10^{-12} cm^3 s^{-1}. The value of k_{eff}^{P} depends on the sample preparation (*i.e.*, different batches of the sample resulted in different values for k_{eff}^{P}), indicating that it is related to the impurities in the sample. It is interesting to note that both positive and negative values were obtained for k_{eff}^{P}. The impurities in the sample may (i) react with the Criegee intermediate to reduce its lifetime (leading to a positive k_{eff}^{P}) and/or (ii) react with other radical species (I atoms, OH radicals, etc.) as a radical scavenger, such that the decay of the Criegee intermediate becomes slightly slower at higher precursor concentrations (leading to a negative k_{eff}^{P}). Nonetheless, the extrapolation using equation (5) should remove such contributions. In the case of $(CH_3)_2COO$, the fitted k_{zc} obtained in this analysis is very similar to the k_{zc} obtained with Model A. We therefore concluded that neither the precursor nor impurities in the precursor sample interfered with the kinetic analysis. However, for $(CD_3)_2COO$, the fitted k_{zc} in Model A-p (and therefore the derived k_d) is somewhat smaller than that in Model A. We comment further on this difference in Section 4.3.4.

Table 4.2. List of k_d values derived from linear fits to k_1 in Experiments 1 and 3.

Exp. #	CI	T (K)	Model A k_{zc} (s^{-1})[a]	Model A k_d (s^{-1})[b]
1a	$(CH_3)_2COO$	283.4	292±80	269±82
1b	$(CH_3)_2COO$	285.3	308±46	285±50
1c	$(CH_3)_2COO$	293.3	348±48	325±52
1d	$(CH_3)_2COO$	298.5	359±46	336±50
1d-2	$(CH_3)_2COO$	298.2	409±45	386±48
1e	$(CH_3)_2COO$	310.2	610±65	587±68
1e-2	$(CH_3)_2COO$	310.1	692±49	669±53
1f	$(CH_3)_2COO$	323.2	939±53	916±56
3a	$(CD_3)_2COO$	283.2	71±27	48±33
3b	$(CD_3)_2COO$	298.5	76±41	53±45
3b-2	$(CD_3)_2COO$	298.5	89±20	66±27
3c	$(CD_3)_2COO$	310.3	72±26	49±32
3c-2	$(CD_3)_2COO$	310.0	94±61	71±64
3d	$(CD_3)_2COO$	323.2	160±55	137±58

[a] The uncertainty in k_{zc} is determined by taking the standard deviation of the residuals from the linear fit to k_1; this estimate takes into account the fluctuation in k_1 caused by temporal changes in flow conditions and by the baseline/background subtraction. The errors in $[(CH_3)_2COO]_0/[(CD_3)_2COO]_0$, temperature, and k_1 fitting are relatively small and are not included in the analysis. [b] Obtained from the relation $k_d = k_{zc} - k_{wl}$. The term k_{wl} is estimated to be 23 s^{-1} (determined by the intercept of the black linear fit in Figure 4.3 with uncertainty of 19 s^{-1} (taken as the standard deviation of residuals from the linear fit). Although this value was determined at 298 K, any possible temperature dependence of k_{wl} between 283 and 323 K is likely to be small relative to the uncertainty in k_d.

4.3.3. Comparison with previous studies

The average values of k_d at 283 K, 298 K, 310 K and 323 K are given in Table 4.4. Table 4.4 shows that the k_d values are much larger than previously reported values determined indirectly in ozonolysis experiments (Refs. 6 and 40). As mentioned in Section 4.1, the small k_d values reported in these ozonolysis studies are not consistent with the k_d values that result from combining the k_d/k_{SO2} ratios determined in similar ozonolysis experiments (Refs. 34 and 41) with k_{SO2} values determined in direct measurements (Ref. 19 and this work). To assess the results in the context of previously reported values from the indirect ozonolysis studies, we compared the k_d values with values obtained by multiplying the k_d/k_{SO2} ratios reported in Ref. 34 and Ref. 41 by directly determined k_{SO2} values. For the case of Berndt *et al.*,[41] we performed experiments to determine the reaction rate coefficient of $(CH_3)_2COO$ with SO_2 at 283 K, 293 K, and 303 K in order to accurately scale the temperature-dependent k_d/k_{SO2} ratios reported in that work. Figures 4.4 and 4.5 show the results.

Table 4.3. Two-dimensional fit (Model A-p) parameters for Experiments #1 and 3.

Exp. #	CI	T (K)	Model A-p $k_{\mathrm{eff}}^{\mathrm{C}}$ (10^{-10} cm^3 s^{-1})	Model A-p $k_{\mathrm{eff}}^{\mathrm{P}}$ (10^{-13} cm^3 s^{-1})	Model A-p k_{zc} (s^{-1})[a]	Model A-p k_{d} (s^{-1})[b]
1a	$(CH_3)_2COO$	283.4	6.11	-0.36	293±80	270±82
1b	$(CH_3)_2COO$	285.3	6.40	-18.5	331±41	312±45
1c	$(CH_3)_2COO$	293.3	5.77	0.86	346±48	327±52
1d	$(CH_3)_2COO$	298.5	5.82	-13.4	395±38	376±42
1d-2	$(CH_3)_2COO$	298.2	5.33	-1.56	406±44	387±48
1e	$(CH_3)_2COO$	310.2	6.49	-27.2	646±58	627±61
1e-2	$(CH_3)_2COO$	310.1	3.68	7.03	682±47	663±51
1f	$(CH_3)_2COO$	323.2	2.77	-6.4	919±51	900±54
3a	$(CD_3)_2COO$	283.2	6.93	13.6	40±14	21±24[c]
3b	$(CD_3)_2COO$	298.5	5.48	11.6	32±22	13±29
3b-2	$(CD_3)_2COO$	298.5	5.61	6.36	78±19	59±27
3c	$(CD_3)_2COO$	310.3	6.42	6.47	44±19	25±27
3c-2	$(CD_3)_2COO$	310.0	4.88	30.1	31±26	12±32
3d	$(CD_3)_2COO$	323.2	4.62	36.4	90±41	71±45

[a] The uncertainty in k_{zc} of Model A-p is determined by taking the standard deviation of the residuals from the two-dimensional fit to k_1. [b] Obtained from the relation $k_{\mathrm{d}} = k_{zc} - k_{\mathrm{wl}}$, using k_{zc} values obtained with Model A-p. [c] Values of k_{d} with ≥100% uncertainty should be considered as upper limits.

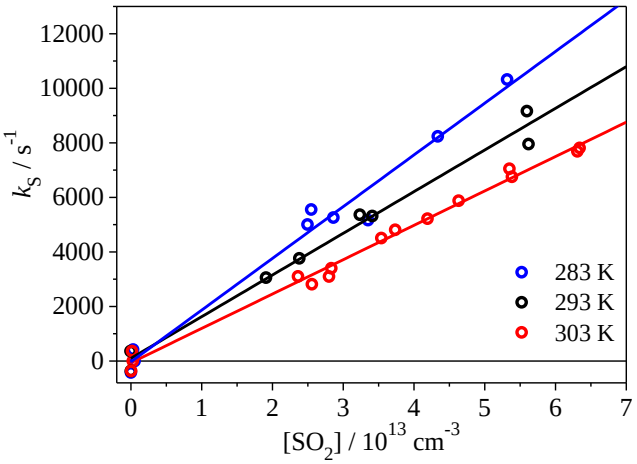

Figure 4.4. Effective loss rate k_S of $(CH_3)_2COO$ at 283 K, 293 K, and 303 K with different SO_2 concentrations added for Experiment #5 ($k_S = k_{\mathrm{obs}} - k_0$ where k_0 is the loss rate k_{obs} with no SO_2 added). The solid lines are linear fits with slope equal to k_{SO2}, the rate coefficient for the reaction of $(CH_3)_2COO$ with SO_2.

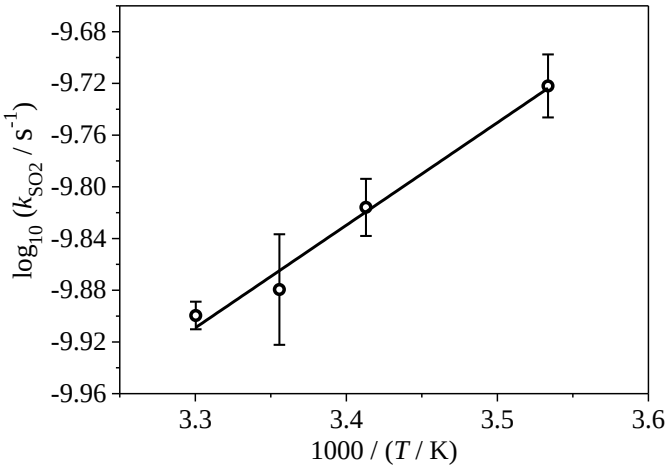

Figure 4.5. Arrhenius log plot of k_{SO2} obtained from the linear fits in Figure 4.4, with k_{SO2} at 298 K from Huang *et al.* 2015[19] also included. The slope of the linear fit corresponds to an Arrhenius activation energy of -3.7 kcal mol^{-1}.

Comparing the values in Table 4.4, it is clear that using k_{SO2} obtained from the direct measurements with the k_d/k_{SO2} ratios reported from the relative-rate ozonolysis studies leads to k_d values closer to the directly measured k_d than to the earlier values. Although the works referenced in Table 4.4 were performed at higher pressures than this work, the pressure dependence experiments shown in Figure 4.6 demonstrate that k_d under the conditions of this study (for both H- and D-substituted CIs) is at the high pressure limit.

The Arrhenius plot of k_d derived from direct measurement of $(CH_3)_2COO$ in this work is shown in Figure 4.7, showing a strong temperature dependence with an Arrhenius activation energy of 5.8±1.2 kcal mol^{-1} (here the uncertainty is represented as $\pm 2\sigma$ from the linear fit to the Arrhenius plot; the individual errors in k_d may increase this value slightly). Figure 4.7 and Table 4.4 show that the temperature dependent k_d values are about a factor of 2 lower than the k_d values derived from the two relative-rate ozonolysis studies. However, the temperature dependence observed in this work closely resembles that reported in the Berndt *et al.* study.[41]

4.3.4. Effect of D-substitution on k_d and comparison with theory

The unimolecular decomposition has been proposed to proceed by a 1,4-hydrogen transfer between the *syn*-substituted methyl group and the terminal oxygen atom on $(CH_3)_2COO$ to form a vinyl hydroperoxide.[47] This step may be followed by elimination of the OH group; as such, thermal decomposition of this and similar Criegee intermediates could be a significant source of OH radicals to the atmosphere.[38,40,47,48] To gain further insight into the mechanism of $(CH_3)_2COO$ thermal decomposition, we performed experiments to measure the loss rate of $(CD_3)_2COO$ at 283 K, 298 K, 310 K and 323 K. The resulting values of k_1 as a function of $[(CD_3)_2COO]_0$ are shown in Figure 4.8.

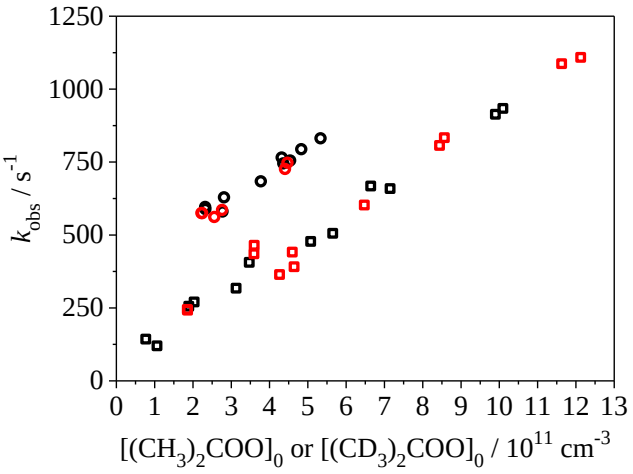

Figure 4.6. Effective loss rate k_{obs} (obtained with Model B) at different initial Criegee intermediate concentrations for different total pressures in Experiments #2 and 4. The total pressure was modified by altering the carrier N_2 flow rate. The intercept k_{zc} is independent of pressure, indicating the unimolecular decomposition rate at 200 Torr is at the high pressure limit. Black symbols: 200 Torr; red symbols: 100 Torr. Circles represent $(CH_3)_2COO$; squares, $(CD_3)_2COO$.

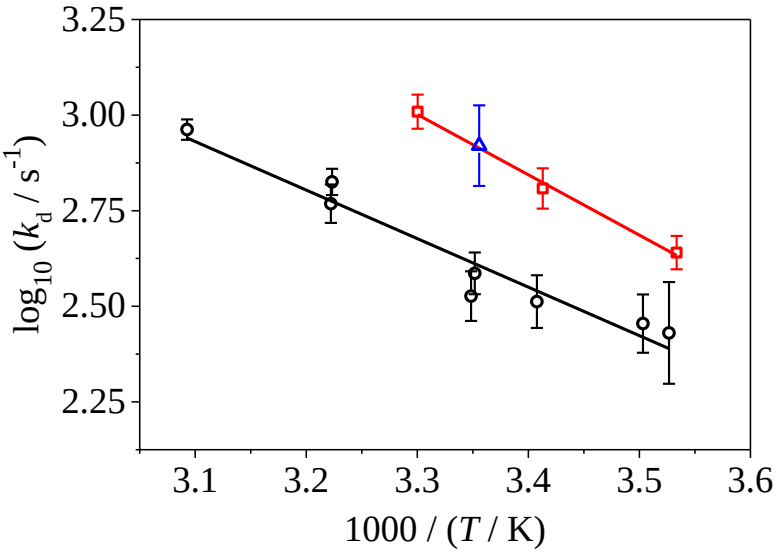

Figure 4.7. Arrhenius log plot of k_d for $(CH_3)_2COO$ obtained in this study. Black circles represent experimental data and the solid black line is a linear fit. Values of k_d derived from the reported k_d/k_{SO2} from Berndt *et al.*[41] using k_{SO2} determined in this work (red squares, solid red line is linear fit) and from Newland *et al.*[34] using k_{SO2} from Huang *et al.*[19] (blue triangle) are included for comparison. The ±0.5 K error in temperature is not shown.

Table 4.4. Summary of k_d/k_{SO2}, k_{SO2}, and k_d for $(CH_3)_2COO$ reported in (or derived from) previous experimental studies and this work. Bold entries indicate reported values; entries in parentheses indicate values taken from other references or scaled to reference values.

Ref.	Reported	Method	T (K)	k_d/k_{SO2} (10^{12} cm^{-3})	k_{SO2} (10^{-10} cm^{3}s^{-1})	k_d (s^{-1})
Kroll *et al.* 2001 (Ref. 40)	k_d	indirect	298*	(6.3±1.4, Ref. 34)	(0.010±0.0027)	**6.4±0.9**
Berndt *et al.* 2012 (Ref. 6)	k_d	indirect	293	(4.2±0.3, Ref. 41)	(0.0071±0.0011)	**3.0±0.4**
Berndt *et al.* 2014 (Ref. 41)	k_d/k_{SO2}	indirect	283	**2.3**	(1.90±0.19, This work)†	(437±44)
Berndt *et al.* 2014 (Ref. 41)	k_d/k_{SO2}	indirect	293	**4.2±0.3**	(1.53±0.15, This work)†	(643±78)
Newland *et al.* 2015 (Ref. 34)	k_d/k_{SO2}	indirect	298	**6.3±1.4**	(1.32±0.13, Ref. 19)	(832±202)
Berndt *et al.* 2014 (Ref. 41)	k_d/k_{SO2}	indirect	303	**8.1**	(1.26±0.13, This work)†	(1021±105)
This work	k_d, k_{SO2}	direct	283	1.4	**1.90±0.19**†	**269±82**‡
This work	k_{SO2}	direct	293	2.2	**1.53±0.15**†	**342**‖
This work & Ref. 19	k_d, k_{SO2}	direct	298	2.7	**1.32±0.13** (Ref. 19)	**361±49**
This work	k_{SO2}	direct	303	3.8	**1.26±0.13**†	**475**‖
This work	k_d	direct	310			**628±60**
This work	k_d	direct	323			**916±56**

* A temperature of 298 K is assumed, since the temperature was not explicitly stated in Ref. 40. † Obtained from the slope of the linear fit to the pseudo-first order plot in Figure 4.5; see text for more details. Estimated error is 10% due to uncertainty in the SO_2 concentration. ‡ The error is $\pm 1\sigma$ (σ = standard deviation). When multiple sets of data are available for one temperature, the average value and pooled standard deviation are used. See Table 4.2 for details. ‖ Obtained from the Arrhenius fit in Figure 4.7.

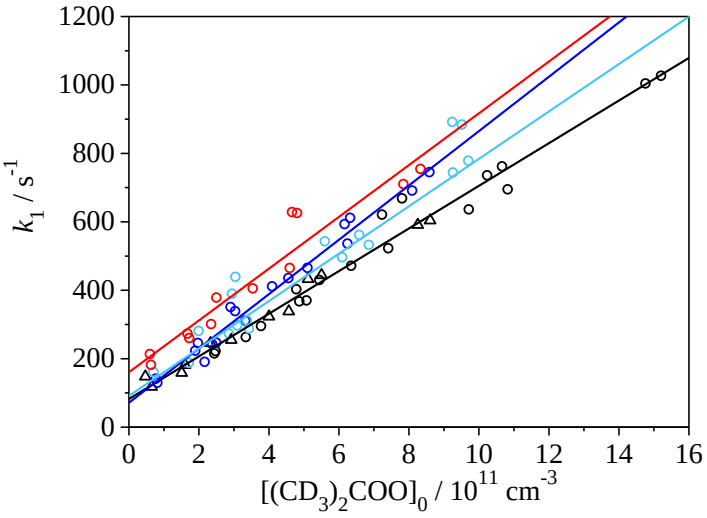

Figure 4.8. First order loss rate k_1 (obtained from Model A with k_2 = 4.1, 6.5, 6.2, and 4.4x10^{-10} cm^3 s^{-1} at 283 K, 298 K, 310 K, and 323 K respectively) at different initial concentrations of the deuterated Criegee intermediate $(CD_3)_2COO$ at 283 K (blue), 298 K (black, different symbols represent experiments performed on different days), 310 K (cyan), and 323 K (red). Lines represent linear fits to k_1 at each temperature.

Comparing Figures 4.2 and 4.8, it is clear that the intercepts k_{zc} are considerably lower for $(CD_3)_2COO$ than for $(CH_3)_2COO$, though the values of k_2 (~ 6.5×10^{-10} cm^3 s^{-1} at 298 K, which results in k_{rad} on the order of 10^{-10} cm^3 s^{-1}, assuming $[X_{rad}]_0 = 5[(CD_3)_2COO]_0$) are similar. The resulting values for k_d of $(CD_3)_2COO$ are listed in Table 4.2 and plotted in Figure 4.9. The value of k_d for $(CD_3)_2COO$ at 298 K was estimated to be <100 s^{-1}.

Although no significant temperature dependence of k_d for $(CD_3)_2COO$ was observed, we note as a caveat that the experimental conditions (*e.g.*, the instability of the baseline over long times) limit the measurement of loss rates slower than 100 s^{-1}. The stated errors in the k_d values for $(CD_3)_2COO$ in Table 4.2 are only the standard deviations and do not include possible systematic errors; therefore, the k_d values for $(CD_3)_2COO$ should be taken with a grain of salt. In addition, the values of k_d obtained from the more detailed Model A-p analysis (see the discussion of Model A-p above and Table 4.3) are somewhat smaller than those obtained from Model A, and the Model A-p values might be better estimates of the true k_d of $(CD_3)_2COO$. However, regardless of these qualifications, a substantial difference in k_d between $(CH_3)_2COO$ and $(CD_3)_2COO$ is observed at all the temperatures studied, indicating that k_d exhibits a strong H/D isotope effect.

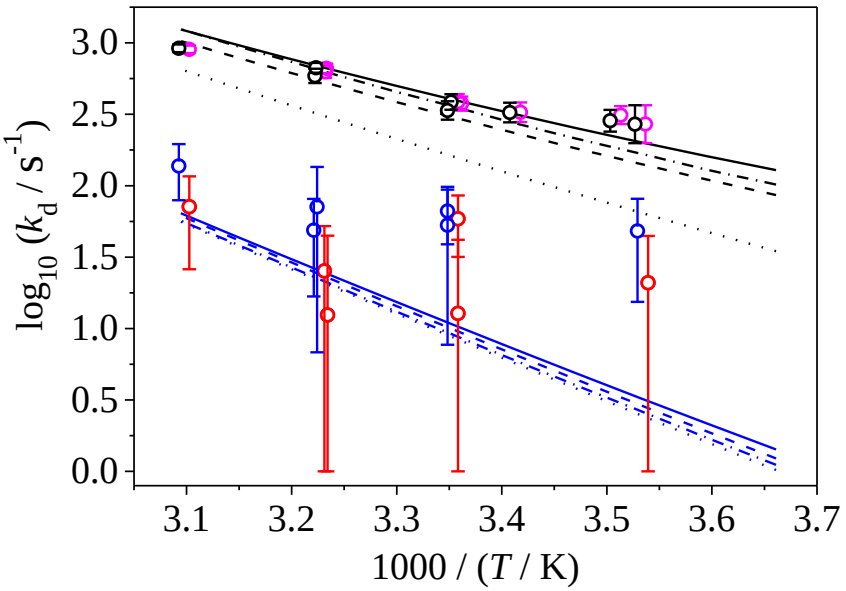

Figure 4.9. Arrhenius log plot of k_d for $(CH_3)_2COO$ determined with Model A (black) and with Model A-p (magenta, shifted right for clarity), and for $(CD_3)_2COO$ determined with Model A (blue) and with Model A-p (red, shifted right for clarity). Symbols represent experimental data, and lines represent the theoretical results (black for $(CH_3)_2COO$, blue for $(CD_3)_2COO$) using different approximation methods for tunneling: solid line, centrifugal-dominant small curvature semiclassical vibrational adiabatic (CDSCSAG) model; dashed line, asymmetric Eckart barrier; dash-dotted line, semiclassical VPT2; dotted line, zero curvature model (see published version of this chapter for details). The ±0.5 K error in temperature is not shown.

4.3.5. Comparison with theoretical $k_d(T)$

To gain a quantitative understanding of the reaction pathway and tunneling contributions, and to directly compare the experimental temperature dependence with the prediction from ab initio calculations, we directly compared the experimental results with the prediction from theoretical simulations of the unimolecular decomposition of $(CH_3)_2COO$ and $(CD_3)_2COO$ (see the published version of this chapter for calculation details). The Arrhenius plot in Figure 4.9 compares the results for $k_d(T)$ of $(CH_3)_2COO$ and $(CD_3)_2COO$ from experiment and theory. The experimental $k_d(T)$ values are consistent with the theoretical predictions for $(CH_3)_2COO$. We note here that the temperature dependence of k_d reported very recently by Fang *et al.*[48] gives results very similar to those obtained in the experiments described here. The experiments in Fang *et al.*[48] determined values for $k_d(E)$ by measuring time-resolved OH formation as a function of infrared excitation energy, providing complementary information to the $k_d(T)$ values reported in the present study. However, considering that the experimental energy range (16.0 to 17.4 kcal mol^{-1}) of the Fang *et al*. study[48] is much higher than the range of energies accessible under thermal conditions, the experimental thermal rates reported in the present work are more relevant to $(CH_3)_2COO$ unimolecular decomposition under atmospheric conditions.

In the case of $(CD_3)_2COO$, while the high temperature k_d values are relatively consistent with the theoretical prediction, we were unable to experimentally measure the low values of k_d (on the order of 10 s^{-1}) predicted by theory for 298 K or lower temperatures. As mentioned above, slow decay rates (< 100 s^{-1}) are difficult to measure under the present experimental conditions, due in part to baseline instability over long times. This experimental limitation is likely the main reason for the discrepancies between experiment and theory for k_d of $(CD_3)_2COO$. Notably, the values for k_d obtained using Model A-p (as described above) are closer to the theoretical result. This indicates that contributions to the $(CD_3)_2COO$ loss from precursor impurities or the precursor itself may be partly responsible for the differences between experiment and theory.

4.3.6. Implications of the present study

The comparison in Table 4.4 between the k_d values for $(CH_3)_2COO$ in this work and the values reported in previous works shows that the former values are about two orders of magnitude larger than those in earlier ozonolysis studies.[6,40] Here we discuss possible reasons for the observed discrepancies. Kroll *et al.*[40] measured the time of OH formation in the ozonolysis of TME, which produces $(CH_3)_2COO$. Although the unimolecular decomposition of $(CH_3)_2COO$ would eventually lead to OH products, the reaction proceeds through a vinyl hydroperoxide intermediate[47] (as seen in the published version of this chapter). At high pressures (*e.g.*, 100 Torr in Ref. 40, 200 Torr in this work) the intermediate would be collisionally stabilized and would decompose to OH on a longer time scale than that of the decomposition of $(CH_3)_2COO$. As a result, the rate constant reported by Ref. 40 would be smaller than that for the unimolecular decomposition of $(CH_3)_2COO$. Theoretical calculations of the reaction coordinate for vinyl hydroperoxide formation and decomposition to OH are currently in progress. The studies in Ref. 6 and Ref. 40 both utilized flow reactor schemes detecting the products of CI unimolecular or bimolecular reactions after mixing alkenes with ozone; hidden systematic problems in their experimental methodologies or uncertainties in the reference values may also contribute to the discrepancies.

The k_d values derived in this work from direct observation of $(CH_3)_2COO$ are consistent with the theoretical predictions, in which the reaction path is also consistent with previous work.[33,47-49] This agreement, along with the fact that the experimental scheme in the present work is markedly less complex than those employing the alkene ozonolysis mechanism to form $(CH_3)_2COO$, supports the assertion that the value for k_d and its temperature dependence reported here can be used to better constrain the unimolecular decomposition rates of $(CH_3)_2COO$. This may be of benefit in a number of applications in CI chemistry, especially considering that TME ozonolysis is often a standard or reference system in alkene ozonolysis studies.

4.4. Conclusion

This work presents the first determination of the unimolecular decomposition rate k_d under thermal conditions for $(CH_3)_2COO$ from direct measurements of the Criegee intermediate. The temperature dependence of k_d from 283 K to 323 K was determined and an Arrhenius activation energy of ~6 kcal mol^{-1} is reported. Theoretical calculations of the temperature dependence of k_d of $(CH_3)_2COO$ are in close agreement with the experimental results. The estimated k_d at room temperature is much

larger than values of k_d reported in earlier studies[6,40] in which indirect methods to measure Criegee intermediates formed from ozonolysis were used. However, the combination of k_d/k_{SO2} reported by recent ozonolysis studies[34,41] and k_{SO2} determined by direct detection of Criegee intermediates[19] gives values for k_d close to the result in this work. In addition, the values for $k_d(T)$ of $(CH_3)_2COO$ determined in this work are consistent with a very recent experimental and theoretical study reporting $k_d(E)$ of $(CH_3)_2COO$.[48] This work also presents experimental evidence of an isotope effect in k_d which is qualitatively consistent with the theoretical prediction, lending support to the proposed 1,4-hydrogen transfer mechanism for the unimolecular decomposition of $(CH_3)_2COO$. The value for k_d determined in this work is quite large at all temperatures studied, which implies that thermal decomposition is one of the dominant pathways for $(CH_3)_2COO$ removal in the atmosphere.

Appendix 4A. Transient absorption traces of all experiments

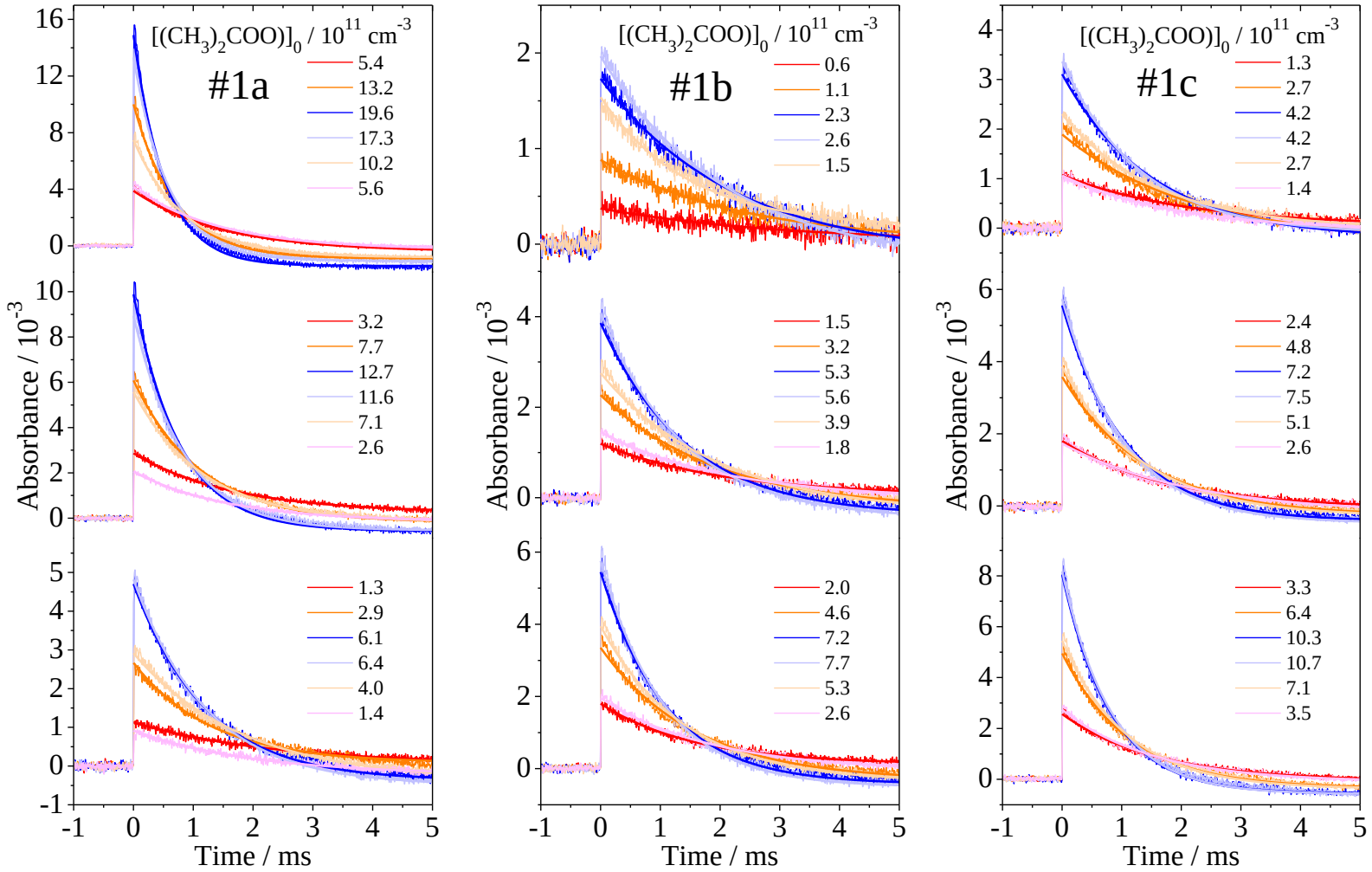

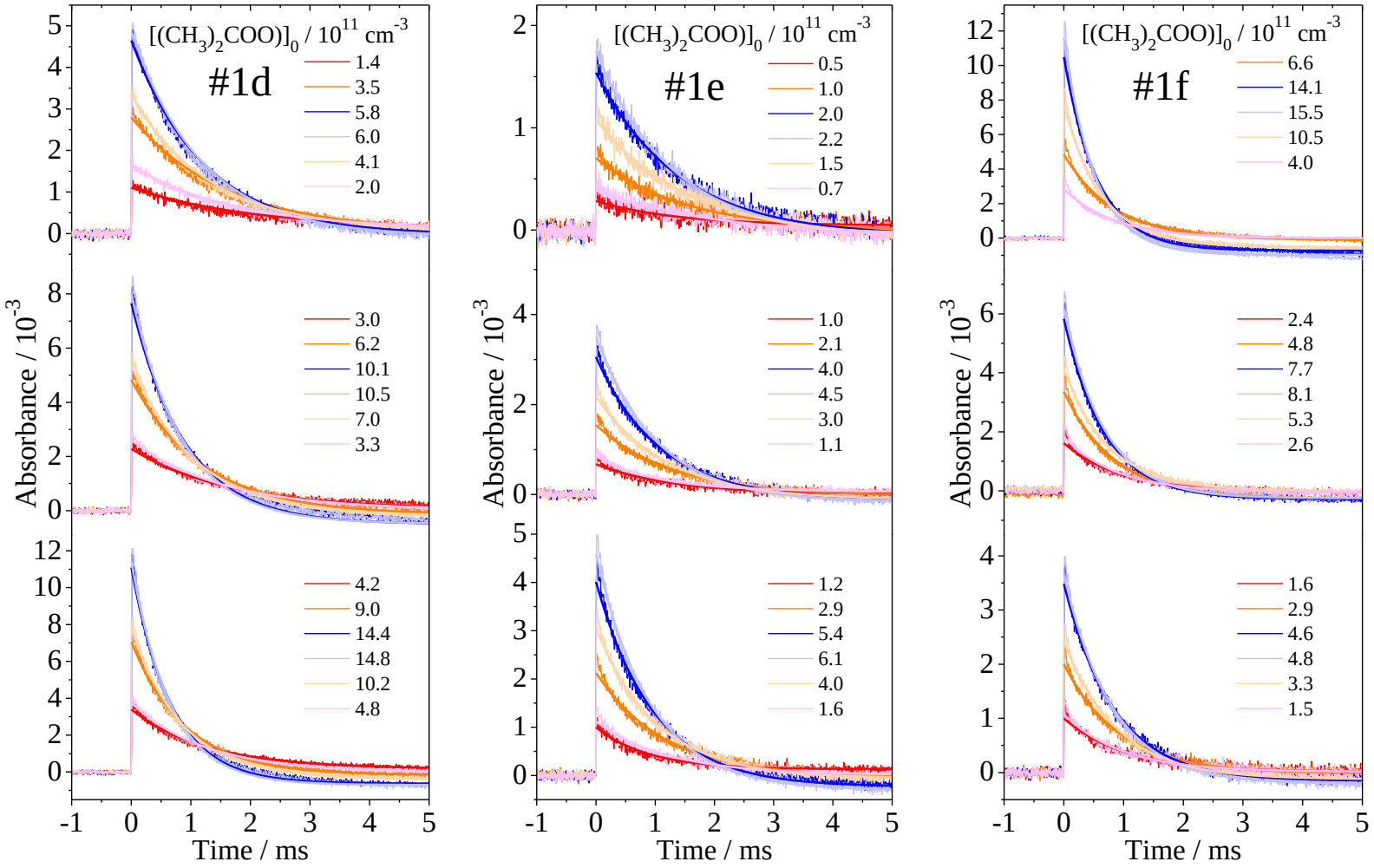

Figure 4A.1. Representative difference absorbance traces at 340 nm showing $(CH_3)_2COO$ formation and decay (photolysis at time 0) for various initial $(CH_3)_2COO$ concentrations for Experiment #1. Solid curves are single exponential fits.

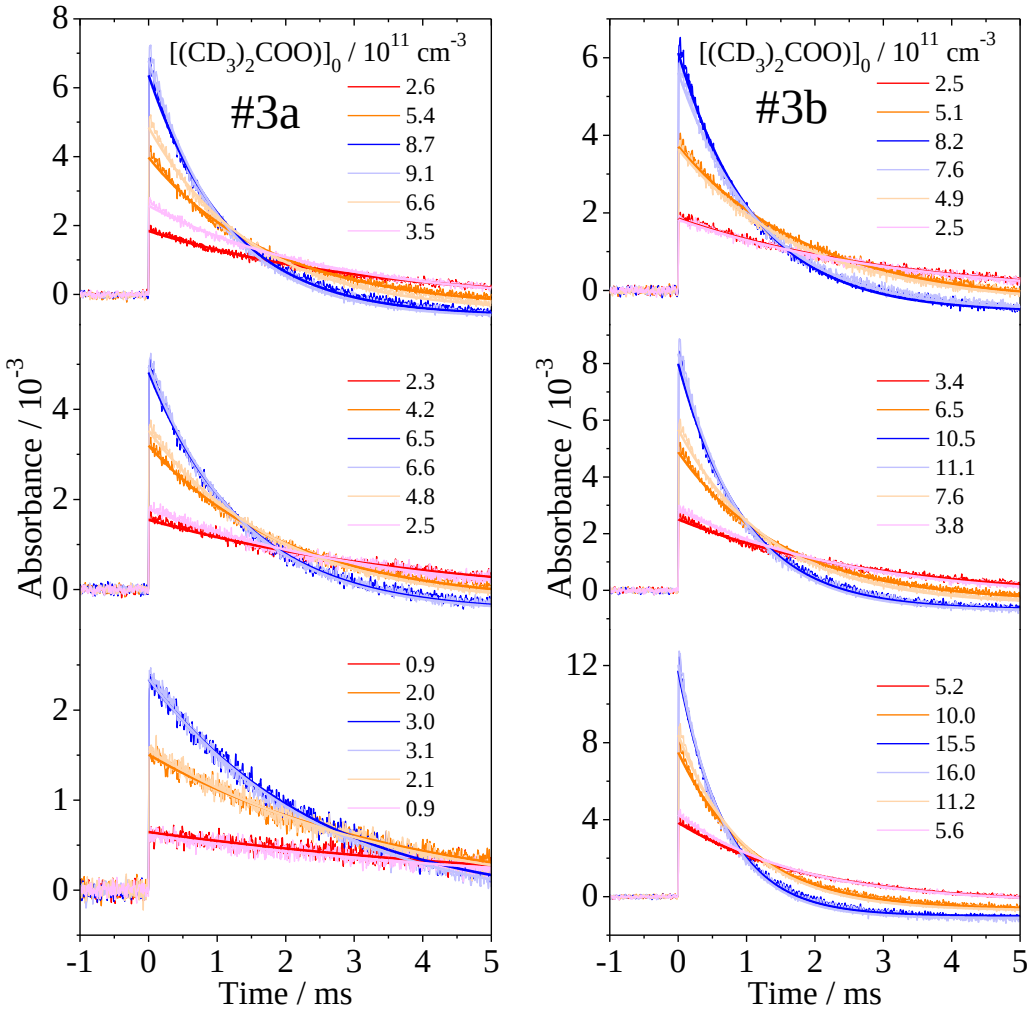
#3a
[(CD3)2COO)]0 / 10^11 cm^-3
2.6
5.4
8.7
9.1
6.6
3.5
2.3
4.2
6.5
6.6
4.8
2.5
0.9
2.0
3.0
3.1
2.1
0.9
Absorbance / 10^-3
Time / ms
#3b
[(CD3)2COO)]0 / 10^11 cm^-3
2.5
5.1
8.2
7.6
4.9
2.5
3.4
6.5
10.5
11.1
7.6
3.8
5.2
10.0
15.5
16.0
11.2
5.6
Absorbance / 10^-3
Time / ms

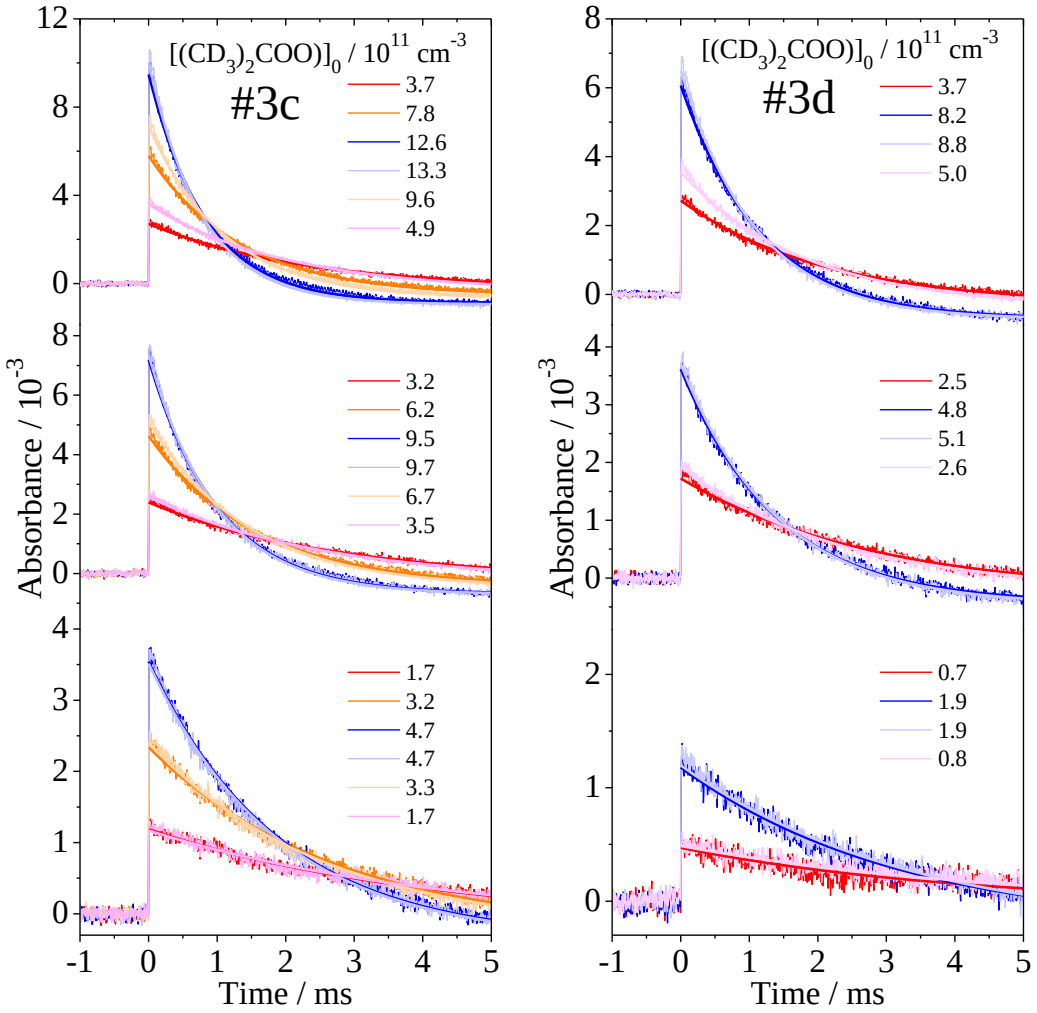

Figure 4A.2. Representative difference absorbance traces at 340 nm showing $(CD_3)_2COO$ formation and decay (photolysis at time 0) for various initial $(CD_3)_2COO$ concentrations for Experiment #3. Solid curves are single exponential fits.

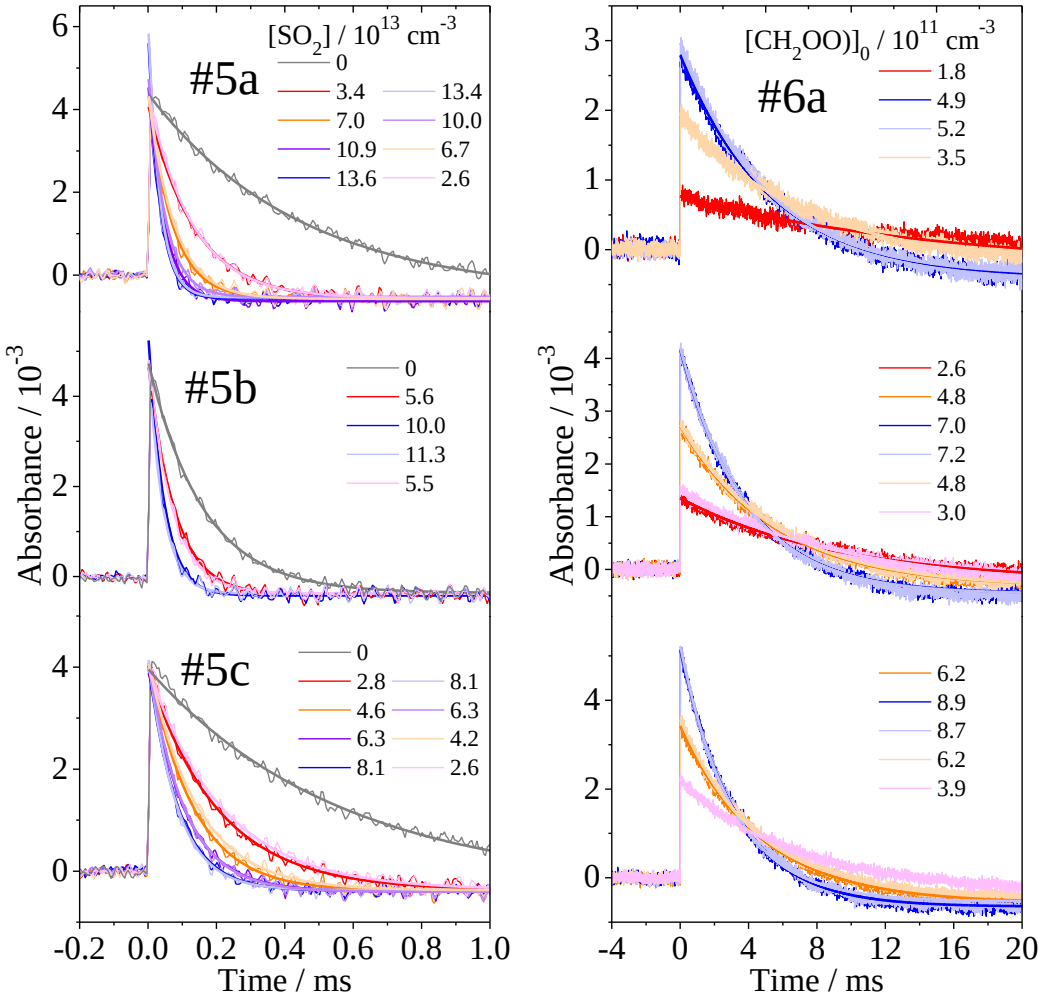

Figure 4A.3. Left: Representative difference absorbance traces at 340 nm showing $(CH_3)_2COO$ formation and decay (photolysis at time 0) with various SO_2 concentrations for Experiment #5. Solid curves are single exponential fits. Initial $(CH_3)_2COO$ concentration: #5a, $4.9\pm0.4\times10^{-11}$ cm^{-3}; #5b, $5.2\pm0.2\times10^{-11}$ cm^{-3}; #5c, $4.9\pm0.1\times10^{-11}$ cm^{-3}. Right: Representative difference absorbance traces at 340 nm showing CH_2OO formation and decay (photolysis at time 0) for various initial CH_2OO concentrations for Experiment #6. Solid curves are single exponential fits.

Appendix 4B. Model B fits to representative transient absorption traces

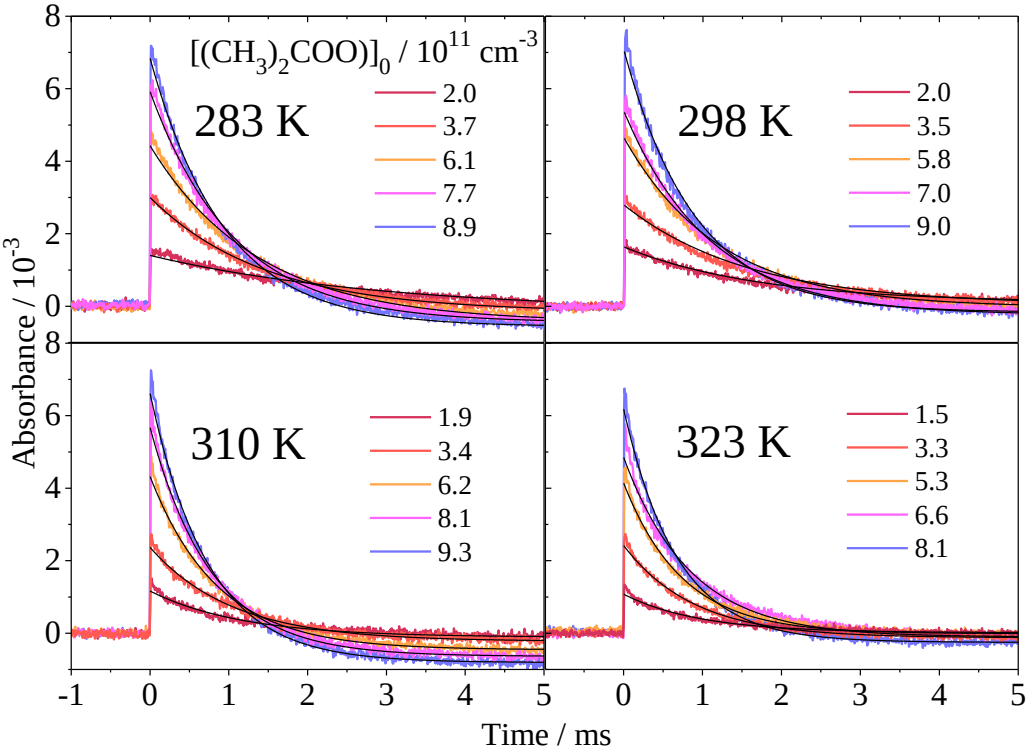

Figure 4B.1. Difference absorbance traces at 340 nm showing $(CH_3)_2COO$ formation and decay in Experiment #1 (as in Figure 4.1 of the main text) with the fits to Model B shown as black curves.

Appendix 4C. Three dimensional plot comparing the fits to Model A and Model A-p

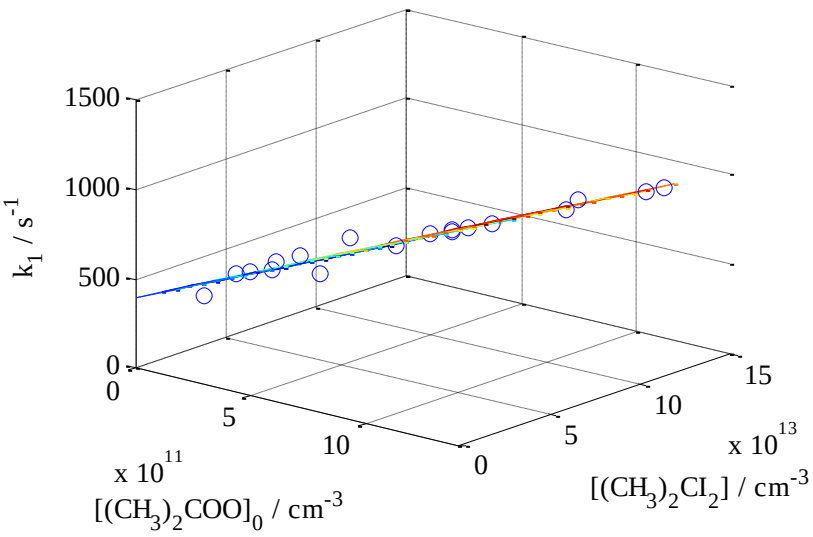

Figure 4C.1. Three dimensional plot for Experiment #1d showing the dependence of k_1 on $[(CH_3)_2COO]_0$ and $[(CH_3)_2CI_2]$. Circles show experimental data; colored surface (viewed on edge) represents k_1 obtained from a two-dimensional fit to $k_1 = k_{zc} + k_{eff}^{C}[(CH_3)_2COO]_0 + k_{eff}^{P}[(CH_3)_2CI_2]$.

References

1. Hasson, A. S.; Chung, M. Y.; Kuwata, K. T.; Converse, A. D.; Krohn, D.; Paulson, S. E. Reaction of Criegee Intermediates with Water Vapor: An Additional Source of OH Radicals in Alkene Ozonolysis? *J. Phys. Chem. A* **2003**, *107*, 6176–6182.
2. Ryzhkov, A.; Ariya, P. A Theoretical Study of the Reactions of Parent and Substituted Criegee Intermediates with Water and the Water Dimer. *Phys. Chem. Chem. Phys.* **2004**, *6*, 5042.
3. Berndt, T.; Voigtländer, J.; Stratmann, F.; Junninen, H.; Mauldin, R. L.; Sipilä, M.; Kulmala, M.; Herrmann, H. Competing Atmospheric Reactions of CH_2OO with SO_2 and Water Vapour. *Phys. Chem. Chem. Phys.* **2014**, *16*, 19130–19136.
4. Martinez, R. I.; Herron, J. T. Gas-phase Reaction of SO_2 with a Criegee Intermediate in the Presence of Water Vapor. *J. Environ. Sci. Health A Environ. Sci. Eng.* **1981**, *16*, 623–636.
5. Vereecken, L.; Harder, H.; Novelli, A. The Reaction of Criegee Intermediates with NO, RO_2, and SO_2, and Their Fate in the Atmosphere. *Phys. Chem. Chem. Phys.* **2012**, *14*, 14682–14695.
6. Berndt, T.; Jokinen, T.; Mauldin, R.; Petäjä, T.; Herrmann, H.; Junninen, H.; Paasonen, P.; Worsnop, D.; Sipilä, M. Gas-Phase Ozonolysis of Selected Olefins: The Yield of Stabilized Criegee Intermediate and the Reactivity Toward SO_2. *J. Phys. Chem. Lett.* **2012**, *3*, 2892–2896.
7. Herron, J. T.; Martinez, R. I.; Huie, R. E. Kinetics and Energetics of the Criegee Intermediate in the Gas Phase. I. The Criegee Intermediate in Ozone-alkene Reactions. *Int. J. Chem. Kinet.* **1982**, *14*, 201–224.
8. Zhang, D.; Lei, W.; Zhang, R. Mechanism of OH Formation from Ozonolysis of Isoprene: Kinetics and Product Yields. *Chem. Phys. Lett.* **2002**, *358*, 171–179.
9. Heard, D. High Levels of the Hydroxyl Radical in the Winter Urban Troposphere. *Geophys. Res. Lett.* **2004**, *31*.
10. Emmerson, K.; Carslaw, N.; Pilling, M. Urban Atmospheric Chemistry During the PUMA Campaign 2: Radical Budgets for OH, HO_2 and RO_2. *J. Atmos. Chem.* **2005**, *52*, 165–183.
11. Mauldin, R. L.; Berndt, T.; Sipilä, M.; Paasonen, P.; Petäjä, T.; Kim, S.; Kurtén, T.; Stratmann, F.; Kerminen, V. M.; Kulmala, M. A New Atmospherically Relevant Oxidant of Sulphur Dioxide. *Nature* **2012**, *488*, 193–196.
12. Sarwar, G.; Simon, H.; Fahey, K.; Mathur, R.; Goliff, W.; Stockwell, W. Impact of Sulfur Dioxide Oxidation by Stabilized Criegee Intermediate on Sulfate. *Atmos. Environ.* **2014**, *85*, 204–214.
13. Johnson, D.; Marston, G. The Gas-phase Ozonolysis of Unsaturated Volatile Organic Compounds in the Troposphere. *Chem. Soc. Rev.* **2008**, *37*, 699–716.
14. Welz, O.; Savee, J. D.; Osborn, D. L.; Vasu, S. S.; Percival, C. J.; Shallcross, D. E.; Taatjes, C. A. Direct Kinetic Measurements of Criegee Intermediate (CH_2OO) Formed by Reaction of CH_2I with O_2. *Science* **2012**, *335*, 204–207.
15. Lee, Y. P. Perspective: Spectroscopy and Kinetics of Small Gaseous Criegee Intermediates. *J. Chem. Phys.* **2015**, *143*, 020901.

16. Osborn, D.; Taatjes, C. The Physical Chemistry of Criegee Intermediates in the Gas Phase. *Int. Rev. Phys. Chem.* **2015**, *34*, 309–360.
17. Stone, D.; Blitz, M.; Daubney, L.; Howes, N. U.; Seakins, P. Kinetics of CH_2OO Reactions with SO_2, NO_2, NO, H_2O and CH_3CHO as a Function of Pressure. *Phys. Chem. Chem. Phys.* **2014**, *16*, 1139–1149.
18. Taatjes, C. A.; Welz, O.; Eskola, A. J.; Savee, J. D.; Scheer, A. M.; Shallcross, D. E.; Rotavera, B.; Lee, E. P.; Dyke, J. M.; Mok, D. K.; *et al.* Direct Measurements of Conformer-dependent Reactivity of the Criegee Intermediate CH_3CHOO. *Science* **2013**, *340*, 177–180.
19. Huang, H. L.; Chao, W.; Lin, J. J. Kinetics of a Criegee Intermediate That Would Survive High Humidity and May Oxidize Atmospheric SO_2. *Proc. Natl. Acad. Sci. U. S. A.* **2015**, *112*, 10857–10862.
20. Beames, J. M.; Liu, F.; Lu, L.; Lester, M. I. Ultraviolet Spectrum and Photochemistry of the Simplest Criegee Intermediate CH_2OO. *J. Am. Chem. Soc.* **2012**, *134*, 20045–20048.
21. Sheps, L. Absolute Ultraviolet Absorption Spectrum of a Criegee Intermediate CH_2OO. *J. Phys. Chem. Lett.* **2013**, *4*, 4201–4205.
22. Ting, W. L.; Chen, Y. H.; Chao, W.; Smith, M. C.; Lin, J. J. The UV Absorption Spectrum of the Simplest Criegee Intermediate CH_2OO. *Phys. Chem. Chem. Phys.* **2014**, *16*, 10438–10443.
23. Smith, M. C.; Ting, W. L.; Chang, C. H.; Takahashi, K.; Boering, K. A.; Lin, J. J. UV Absorption Spectrum of the C2 Criegee Intermediate CH_3CHOO. *J. Chem. Phys.* **2014**, *141*, 074302.
24. Liu, F.; Beames, J. M.; Green, A. M.; Lester, M. I. UV Spectroscopic Characterization of Dimethyl- and Ethyl-substituted Carbonyl Oxides. *J. Phys. Chem. A* **2014**, *118*, 2298–2306.
25. Welz, O.; Eskola, A. J.; Sheps, L.; Rotavera, B.; Savee, J. D.; Scheer, A. M.; Osborn, D. L.; Lowe, D.; Murray Booth, A.; Xiao, P.; *et al.* Rate Coefficients of C1 and C2 Criegee Intermediate Reactions with Formic and Acetic Acid Near the Collision Limit: Direct Kinetics Measurements and Atmospheric Implications. *Angew. Chem. Int. Ed. Engl.* **2014**, *126*, 4635–4638.
26. Buras, Z. J.; Elsamra, R. M.; Jalan, A.; Middaugh, J. E.; Green, W. H. Direct Kinetic Measurements of Reactions Between the Simplest Criegee Intermediate CH_2OO and Alkenes. *J. Phys. Chem. A* **2014**, *118*, 1997–2006.
27. Chhantyal-Pun, R.; Davey, A.; Shallcross, D. E.; Percival, C. J.; Orr-Ewing, A. J. A Kinetic Study of the CH_2OO Criegee Intermediate Self-reaction, Reaction with SO_2 and Unimolecular Reaction Using Cavity Ring-down Spectroscopy. *Phys. Chem. Chem. Phys.* **2015**, *17*, 3617–3626.
28. Chao, W.; Hsieh, J. T.; Chang, C. H.; Lin, J. J. Direct Kinetic Measurement of the Reaction of the Simplest Criegee Intermediate with Water Vapor. *Science* **2015**, *347*, 751–754.
29. Lewis, T. R.; Blitz, M. A.; Heard, D. E.; Seakins, P. W. Direct Evidence for a Substantive Reaction Between the Criegee Intermediate, CH_2OO, and the Water Vapour Dimer. *Phys. Chem. Chem. Phys.* **2015**, *17*, 4859–4863.

30. Smith, M. C.; Chang, C. H.; Chao, W.; Lin, L. C.; Takahashi, K.; Boering, K. A.; Lin, J. J. Strong Negative Temperature Dependence of the Simplest Criegee Intermediate CH_2OO Reaction with Water Dimer. *J. Phys. Chem. Lett.* **2015**, *6*, 2708–2713.
31. Anglada, J. M.; González, J.; Torrent-Sucarrat, M. Effects of the Substituents on the Reactivity of Carbonyl Oxides. A Theoretical Study on the Reaction of Substituted Carbonyl Oxides with Water. *Phys. Chem. Chem. Phys.* **2011**, *13*, 13034–13045.
32. Sheps, L.; Scully, A. M.; Au, K. UV Absorption Probing of the Conformer-dependent Reactivity of a Criegee Intermediate CH_3CHOO. *Phys. Chem. Chem. Phys.* **2014**, *16*, 26701–26706.
33. Olzmann, M.; Kraka, E.; Cremer, D.; Gutbrod, R.; Andersson, S. Energetics, Kinetics, and Product Distributions of the Reactions of Ozone with Ethene and 2,3-Dimethyl-2-butene. *J. Phys. Chem. A* **1997**, *101*, 9421–9429.
34. Newland, M. J.; Rickard, A. R.; Alam, M. S.; Vereecken, L.; Muñoz, A.; Ródenas, M.; Bloss, W. J. Kinetics of Stabilised Criegee Intermediates Derived from Alkene Ozonolysis: Reactions with SO_2, H_2O and Decomposition Under Boundary Layer Conditions. *Phys. Chem. Chem. Phys.* **2015**, *17*, 4076–4088.
35. Berndt, T.; Kaethner, R.; Voigtländer, J.; Stratmann, F.; Pfeifle, M.; Reichle, P.; Sipilä, M.; Kulmala, M.; Olzmann, M. Kinetics of the Unimolecular Reaction of CH_2OO and the Bimolecular Reactions with the Water Monomer, Acetaldehyde and Acetone Under Atmospheric Conditions. *Phys. Chem. Chem. Phys.* **2015**, *17*, 19862–19873.
36. Anglada, J. M.; Bofill, J. M.; Olivella, S.; Solé, A. Unimolecular Isomerizations and Oxygen Atom Loss in Formaldehyde and Acetaldehyde Carbonyl Oxides. A Theoretical Investigation. *J. Am. Chem. Soc.* **1996**, *118*, 4636–4647.
37. Martinez, R. I.; Herron, J. T. Stopped-flow Studies of the Mechanisms of Ozone-alkene Reactions in the Gas Phase: Tetramethylethylene. *J. Phys. Chem.* **1987**, *91*, 946–953.
38. Liu, F.; Beames, J. M.; Petit, A. S.; McCoy, A. B.; Lester, M. I. Infrared-driven Unimolecular Reaction of CH_3CHOO Criegee Intermediates to OH Radical Products. *Science* **2014**, *345*, 1596–1598.
39. Kroll, J.; Clarke, J.; Donahue, N.; Anderson, J. Mechanism of HO_x Formation in the Gas-Phase Ozone−Alkene Reaction. 1. Direct, Pressure-Dependent Measurements of Prompt OH Yields. *J. Phys. Chem. A* **2001**, *105*, 1554–1560.
40. Kroll, J.; Sahay, S.; Anderson, J.; Demerjian, K.; Donahue, N. Mechanism of HO_x Formation in the Gas-Phase Ozone-Alkene Reaction. 2. Prompt Versus Thermal Dissociation of Carbonyl Oxides to Form OH. *J. Phys. Chem. A* **2001**, *105*, 4446–4457.
41. Berndt, T.; Jokinen, T.; Sipilä, M.; Mauldin, R.; Herrmann, H.; Stratmann, F.; Junninen, H.; Kulmala, M. H_2SO_4 Formation from the Gas-phase Reaction of Stabilized Criegee Intermediates with SO_2: Influence of Water Vapour Content and Temperature. *Atmos. Environ.* **2014**, *89*, 603–612.
42. Pross, A.; Sternhell, S. Oxidation of Hydrazones with Iodine in the Presence of Base. *Aust. J. Chem.* **1970**, *23*, 989.
43. Chang, Y.; Chang, C.; Lin, J. J. Absolute UV Absorption Cross Sections of Dimethyl Substituted Criegee Intermediate $(CH_3)_2COO$. **2016**, submitted.

44. Ting, W. L.; Chang, C. H.; Lee, Y. F.; Matsui, H.; Lee, Y. P.; Lin, J. J. Detailed Mechanism of the $CH_2I + O_2$ Reaction: Yield and Self-reaction of the Simplest Criegee Intermediate CH_2OO. *J. Chem. Phys.* **2014**, *141*, 104308.
45. Su, Y. T.; Lin, H. Y.; Putikam, R.; Matsui, H.; Lin, M. C.; Lee, Y. P. Extremely Rapid Self-reaction of the Simplest Criegee Intermediate CH_2OO and Its Implications in Atmospheric Chemistry. *Nat. Chem.* **2014**, *6*, 477–483.
46. Buras, Z. J.; Elsamra, R. M.; Green, W. H. Direct Determination of the Simplest Criegee Intermediate (CH_2OO) Self Reaction Rate. *J. Phys. Chem. Lett.* **2014**, *5*, 2224–2228.
47. Liu, F.; Beames, J. M.; Lester, M. I. Direct Production of OH Radicals Upon CH Overtone Activation of $(CH_3)_2COO$ Criegee Intermediates. *J. Chem. Phys.* **2014**, *141*, 234312.
48. Fang, Y.; Liu, F.; Barber, V. P.; Klippenstein, S. J.; McCoy, A. B.; Lester, M. I. Communication: Real Time Observation of Unimolecular Decay of Criegee Intermediates to OH Radical Products. *J. Chem. Phys.* 2016, *144*, 061102.
49. Gutbrod, R.; Kraka, E.; Schindler, R. N.; Cremer, D. Kinetic and Theoretical Investigation of the Gas-Phase Ozonolysis of Isoprene: Carbonyl Oxides as an Important Source for OH Radicals in the Atmosphere. *J. Am. Chem. Soc.* **1997**, *119*, 7330–7342.

Chapter 5

Isotopic composition of N_2O formed in corona discharge as a function of pressure and discharge energy

5.1 Introduction

Nitrous oxide (N_2O) is the third most important greenhouse gas after CO_2 and methane, with a global warming potential 265 times that of CO_2 over a 100 year time horizon.[1] The concentration of N_2O in the atmosphere is currently about 325 ppb, and has risen by about 20% over preindustrial levels, due mainly to increasing fertilizer use.[1–4] Limiting N_2O emissions is an important component of climate change mitigation. N_2O was included as one of six greenhouse gases targeted for emissions reduction in the 1997 Kyoto Protocol,[5] and more than 100 countries pledged in the recent Paris agreement to reduce emissions of N_2O and other agricultural greenhouse gases in order to limit the increase in global average temperature to 2°C by 2100.[6]

The main source of N_2O to the atmosphere is microbial activity in soils and in the ocean.[2,7,8] Other known sources include biomass burning, fossil fuel combustion, and lightning.[7,9] The main sinks of N_2O are photolysis (90%) and photo-oxidation (10%) in the stratosphere. The latter process produces NO radicals with about a 60% yield, and the resulting stratospheric NO_x ($NO + NO_2$) participates in catalytic cycles of ozone destruction.[8,10,11] N_2O is therefore considered an ozone-depleting substance (ODS) in addition to being a greenhouse gas.[11] Notably, N_2O was not included as an ODS in the 1987 Montreal Protocol or in subsequent agreements, in contrast to chlorofluorocarbons which have been extensively regulated;[11] this omission was partly due to uncertainties in the relative magnitudes of anthropogenic and natural sources of N_2O to the atmosphere at the time. However, now that chlorofluorocarbon emissions have been successfully phased out, N_2O is considered the most significant anthropogenic ODS.[11] In light of the high global warming potential of N_2O and its capacity for ozone depletion, it is of vital importance that we quantify and ultimately control anthropogenic emissions of N_2O to the atmosphere, as well as reliably predict future changes in its anthropogenic and natural sources.

While the observed rise in atmospheric N_2O levels since preindustrial times can be roughly explained by the imbalance between the magnitudes of the sources (both anthropogenic and natural) and the stratospheric sinks,[8,12,13] a quantitative and mechanistic understanding of N_2O sources and their spatial and temporal variability is required to develop effective policies for limiting emissions. Over the last decade, as highly precise measurements of atmospheric N_2O concentrations at a number of locations have become available,[14–17] inverse models have been used to infer the magnitudes and temporal and geographic distribution of N_2O sources.[14,15,18–21] A large source of uncertainty in these studies is the transport of air depleted in N_2O from the stratosphere to the troposphere, which can influence concentrations near the Earth's surface on annual, subannual, and interannual timescales.[14,15] In addition to this uncertainty due to stratospheric chemistry, results from inverse models have suggested that N_2O emissions in the tropics are higher than expected. Indeed, higher tropical or subtropical N_2O emissions may be consistent with observations of elevated N_2O concentrations in the upper tropical and subtropical troposphere during the HIPPO (HIaper Pole-to-Pole Observations) campaign.[22,23] The source of the elevated N_2O

remains ambiguous; Wofsy *et al.*[22,23] suggested lofting of tropical soil emissions by convective activity or perhaps other sources such as biomass burning or lightning could be responsible for the temporal and spatial variability observed.

Measurements of the isotopic composition of N_2O can provide additional constraints on which sources or sinks of atmospheric N_2O affect, for example, an air parcel or a time series of measurements at a given location. This additional information provided by the isotope composition stems from the fact that isotope fractionation due to different N_2O production or destruction processes (*e.g.*, production by microbial nitrification or denitrification, or destruction by stratospheric photolysis) often results in distinctive $^{15}N/^{14}N$ and $^{18}O/^{16}O$ ratios in the N_2O produced (for a production process) or the N_2O remaining after some fraction of the N_2O is destroyed (for a destruction process). For example, Park *et al.*[3] measured a long-term decreasing trend in the $^{15}N/^{14}N$ and $^{18}O/^{16}O$ heavy isotope ratios of N_2O in firn air from Antarctica, as well as seasonal and interannual variations in the isotope ratios of N_2O in air archived at Cape Grim, Tasmania between 1978 and 2005. The long-term decrease in the heavy isotope ratios of N_2O was attributed to the increasing magnitude of isotopically depleted microbial sources (depleted in the heavy isotopes ^{15}N and ^{18}O) to the atmosphere. Furthermore, the observed seasonal cycles in N_2O isotope composition were in phase with what was expected from the seasonality of the transport of isotopically-enriched N_2O from the stratosphere (since photolysis enriches the residual N_2O in ^{15}N and ^{18}O); yet the combination of the $^{15}N/^{14}N$ and $^{18}O/^{16}O$ ratios with the $^{15}N/^{14}N$ ratio at the central nitrogen atom showed that these isotope signals could not be due to stratosphere-to-troposphere transport alone, and also implicated an important contribution from Southern Ocean upwelling,[3] a significant but not well-quantified source of N_2O that may increase in magnitude as climate changes.[24,25] Thus, the "isotopic fingerprint" allowed differentiation of the influence of both the stratospheric sources and the ocean upwelling sink of surface air in Tasmania, which could not be distinguished by concentration measurements alone.

The isotopic composition of stratospheric N_2O[26–30] and N_2O produced by microbial nitrification, denitrification, and nitrifier denitrification (*e.g.*, Refs. 31–39) have been extensively studied. In contrast, the isotopic signature of N_2O produced by biomass burning and combustion in general has been investigated by only two laboratory studies,[40,41] and the isotopic composition of N_2O produced by electrical discharge has never been measured directly (apart from recent trial measurements performed in our laboratory[42]). The isotopic composition of N_2O formed in lightning may be of particular interest for identifying the origin of the enhanced N_2O levels in the tropical and subtropical upper troposphere during HIPPO. N_2O is known to be produced in corona discharges in air,[43–50] possibly through a variety of potential mechanisms outlined in Table 5.1.[46,51–74] Large enrichments in ^{15}N have been reported of up to 3000% in nitrogen atoms in a plasma discharge in N_2[75] and of up to 21% in the sum of "nitrogen oxides" in a plasma discharge in air;[76] although these studies did not measure N_2O directly and did not use standard isotope methodology to determine the enrichments, they do suggest that N_2O produced under plasma discharge conditions might exhibit large enrichments in ^{15}N.

This chapter describes the first direct measurements of the isotopic composition of N_2O formed in a corona discharge in air as a function of pressure and discharge voltage. The resulting isotopic composition helps to characterize the "isotopic fingerprint" of N_2O

generated by in-cloud and cloud-to-cloud lightning which could be used to determine the origin of enhanced N_2O concentrations in the upper troposphere, and may also help to elucidate the chemical mechanisms leading to N_2O production (and destruction) in a corona discharge.

Table 5.1. Proposed reactions relevant for N_2O formation and destruction in electric discharges.

Important electron impact reactions		
a)	$e^- + O_2 \rightarrow O_2(^1D,^1S) + e^-$ $e^- + N_2 \rightarrow N_2(^3S,^3P,^1S) + e^-$ $e^- + O_2 \rightarrow 2\ O(^3P) + e^-$ $e^- + O_2 \rightarrow O(^3P) + O(^1D) + e^-$ $e^- + N_2 \rightarrow 2\ N(^4S) + e^-$	*e.g.*, Chen and Davidson (2002)[51]
N_2O formation reactions		
b)	$N(^4S) + NO_2 \rightarrow N_2O + O$	*e.g.*, Wennberg et al., 1994;[52] see also Semeniuk *et al.* (2008),[77] Funke *et al.* (2008),[53] Sheese *et al.* (2016)[54] for formation in upper atmosphere
c)	$N_2(A^3\Sigma) + O_2 \rightarrow N_2O^* + O(^3P)$ $N_2O^* + M \rightarrow N_2O + M$	Zipf (1980),[55] Iannuzzi *et al.* (1982),[56] Fraser and Piper (1989),[57] Funke *et al.* (2008),[58] Sheese *et al.* (2016)[54]
d)	$O(^1D) + N_2 + M \rightarrow N_2O + M$	DeMore and Raper, 1962;[59] Estupiñán *et al.* (2002)[60]
e)	$O_3(^1B_2) + N_2 \rightarrow N_2O + O_2$ $O_3(^3B_1) + N_2 \rightarrow N_2O + O_2$	Prasad (2002),[65] Prasad (2005),[66] Prasad and Zipf (2008)[67]
f)	$N_2(v \geq 15) + O_2(A^1\Delta \text{ or } b^1\Sigma) \rightarrow N_2O + O$	Fraser *et al.* (1990)[68]
g)	$NO_3(A^2E') + N_2 \rightarrow N_2O + NO_2$ $NO_2(A^2B_1, {}^2B_2) + N_2 \rightarrow N_2O + NO$	Zellner *et al.* (1992),[69] Marić *et al.* (1992)[70]
h)	$O_3^+ + N_2 \leftrightarrow N_2O_3^+$ $N_2O_3^+ \rightarrow N_2O + O_2^+$	Cacace *et al.* (2001),[61] Midey *et al.* (2002),[62] Zhu *et al.* (2003),[63] de Petris (2003)[64]
N_2O destruction reactions (in discharges)		
i)	$N_2O + e^- \rightarrow N_2 + O + e^-$	Piper and Rawlins (1986),[71] Kline *et al.* (1991)[46]
j)	$N_2O + M^+ \rightarrow N_2O^+ + M$ $N_2O^+ + e^- \rightarrow N_2 + O$	Hu *et al.* (2002)[72]
k)	$N_2O + O(^1D) \rightarrow 2NO$ $N_2O + O(^1D) \rightarrow 2N_2 + O_2$	Cleland and Hess (1989),[73] Herron and Green (2001)[74]
l)	$N_2O + M^* \rightarrow N_2 + O$	Piper and Rawlins (1986),[71] Kline *et al.* (1991)[46]

5.2 Experimental methods

5.2.1 Corona discharge experiments

Figure 5.1 shows a schematic of the experimental setup constructed by Randazzo[42] for the purpose of producing N_2O by flowing zero air (dry air, 80% N_2, 20% O_2) in a corona discharge cell for subsequent measurements of its isotopic composition. The cell is connected to a glass manifold equipped with a turbo pump system (CFV100, Alcatel Vacuum Technology). A flowing mixture of N_2 and O_2 (Ultra Zero grade, Praxair, Danbury, CT; delivery pressure of 15 psig) was introduced into the manifold upstream of the discharge cell. The flow rate was regulated with a metering valve (Nupro valve M series, Kurt J. Lesker Company) upstream of the cell, and a convection gauge (317, MKS Instruments, Andover, MA, calibrated for air) downstream of the discharge cell was used to measure the downstream pressure of the flowing gas mixture.

The discharge cell consists of a 12 cm long stainless steel tube (2 cm diameter) with a tungsten wire (100 μm diameter) suspended in the tube center. The wire is connected to a high voltage power supply (MJ10P1550, Glassman High Voltage, High Bridge, NJ), with its high voltage output controlled by a variable 0-10 V signal from a low voltage power supply (1651A, B&K Precision, Yorba Linda, CA). The tube is grounded through a picoammeter (6485, Keithley Instruments, Cleveland, OH). Once the flow of zero air stabilized, a voltage between 0.25 and 5.0 kV (1.5 mA current) was applied to the tungsten wire in the discharge cell. The resulting voltage difference (extending radially from the wire to the surrounding tube wall) induces an electric current that can dissociate or ionize N_2 and O_2 in the flowing zero air mixture, initiating the chemistry leading to formation of N_2O as well as NO, NO_2, ozone, and possible other products related to impurities in the zero air (*e.g.*, very small amounts of CO, CO_2). A purple glow in the discharge cell provided a visual confirmation of the corona discharge, which can be attributed mainly to fluorescence of excited and/or ionized N_2.[78,79] Downstream of the discharge cell, the discharge products, entrained in the zero air flow, passed through a trap containing NaOH-coated silica (Ascarite, Sigma-Aldrich, St. Louis, MO) to remove NO_2 and some NO as well as any residual CO_2 in the zero air, and a silver wool trap (Sigma-Aldrich, St. Louis, MO) to remove ozone. Downstream of these traps, the mixture then passed through a Russian doll trap[80] (*i.e.*, a trap equipped with a very efficient high-surface area nested glass thimble) immersed in liquid nitrogen (LN2), in which N_2O and other trace gases condensable at 77 K (mainly H_2O) were trapped.

After 15 minutes (or 5 or 45 minutes for some experiments – see below and Table 5.2), the high voltage was switched off, terminating the corona discharge. The flow of zero air through the cell was maintained for 2-3 more minutes to condense all remaining N_2O in the Russian doll trap, and then the metering valve was closed (halting the flow of zero air) and the non-condensable N_2 and O_2 was pumped away for 10-15 minutes with N_2O condensed in the Russian doll trap. Following this step, the 10 mL glass sample tube on the sample port was immersed in LN2 and the Russian doll trap containing N_2O was immersed in an ethanol slush at -95℃ (with one run at -75℃) for at least 15 minutes, so that N_2O was transferred into the sample tube while any residual H_2O remained condensed in the Russian doll trap. The sample tube was then isolated and warmed to room temperature, and the pressure in a calibrated volume was measured with a capacitance manometer (Baratron, 10 Torr range, MKS Instruments) to determine the yield of N_2O. The N_2O was then expanded to an evacuated 40 mL

stainless steel cylinder, which was isolated and removed from the manifold to prepare for IRMS analysis. (Some of the earlier experiments involved immersing the stainless steel cylinder in LN2 in order to condense all the N_2O generated during the run into the cylinder. However, this caused a leak in one of the cylinders, so this procedure was discontinued since enough N_2O for multiple IRMS analyses could be collected simply by expansion from the glass sample tube into the cylinder. All N_2O yields were calculated according to the pressure in the calibrated volume for each procedure.)

Since the flow rate through the discharge cell was not measured directly in these first experiments, the flow rate was estimated using the air flow calculator at http://www.tlv.com/global/TI/calculator/air-flow-rate-through-valve.html, the variable flow coefficient of the metering valve C_v, and the approximate cell pressure. At downstream pressures less than 1 Torr (C_v ~ 0.0005), the estimated flow rate through the discharge cell was ~3700 cm^3 s^{-1}, corresponding to a residence time of ~10 ms in the discharge cell and an average energy input per reactant (zero air) molecule of ~0.5 eV. The energy input per reactant molecule decreased as the discharge voltage was lowered. For the highest pressure flow experiments (5-10 Torr, C_v ~ 0.001-0.002) the estimated flow rate was lower, about 540 cm^3 s^{-1}, corresponding to a longer residence time of ~70 ms and somewhat lower energy input per reactant molecule of ~0.1-0.2 eV. Appendix 5A gives a summary of these estimated flow rates and energy inputs per reactant molecule for the experimental conditions explored in this work.

In addition to the experiments described above in which the corona discharge was operated with zero air flowing continuously through the system, two experiments were run under static conditions at a pressure of ~10 Torr. In these experiments, the valve to the high-flow turbo pump system was closed and zero air was introduced through the metering valve until the system reached a pressure of ~10 Torr on the Baratron gauge. Then, the metering valve to the zero air was closed, LN2 was placed on the Russian doll trap, and the discharge was switched on. After 15 minutes, the discharge was switched off and the non-condensable gases (mainly N_2 and O_2) were pumped away through the Russian doll trap. (In one of the experiments the LN2 was not placed on the Russian doll trap until after the discharge was terminated; see footnote in Table 5.2.) The rest of the procedure was the same as for the flow experiments described above.

Appendix 5B provides a summary of the individual experimental conditions for each run in this chapter. Experiments #1a-1f in Appendix 5B were performed to measure the dependence of the isotopic composition on the discharge voltage; in these runs the voltage delivered to the discharge cell was varied between 0.25 and 5.0 kV, with the downstream pressure (measured on the downstream convection gauge) held approximately constant at ~0.5 Torr. (In Experiment #1a-3, the temperature of the ethanol slush for separating N_2O from H_2O was -75°C, rather than -95°C as in all other runs. This run was used to check for possible incomplete collection in the -95°C slush runs. No significant difference in the N_2O isotopic composition was observed.) Experiments #2a-2d (low pressure) and Experiments #3a, 3b, and 3b-2 (high pressure) were performed to measure the dependence of the isotopic composition on downstream pressure/flow rate. In the low pressure runs, the downstream pressure was varied from 0.065 to 0.865 Torr. In the high pressure runs, the downstream pressure was set to 5 Torr (1 run) and to 10 Torr (2 runs). Experiments #4a and 4b were performed under static conditions at 10 Torr. The discharge voltage was set at 5.0 kV for all the pressure runs.

A number of blank and control runs were performed (which are not listed in Appendix 5B). In early tests of the system detailed in Randazzo,[42] the gas mixture flowing out of the discharge cell was delivered to a Residual Gas Analyzer (a small quadrupole mass spectrometer; Model 300, Stanford Research Systems, Sunnyvale, CA) which showed that N_2O and other products formed only when the corona discharge was on. In the present study, blank tests were performed in which the full collection procedure was carried out with zero air but without turning on the high voltage power supply (*i.e.*, without running the corona discharge). No detectable amount of condensable gases were trapped, indicating again that the measured yield in the experiments can be fully attributed to species formed in the corona discharge. A control run was also performed in which an aliquot of pure N_2O from our IRMS working standard was introduced into the flowing zero air upstream of the discharge cell and processed by the full procedure (without turning on the discharge). The amount of N_2O collected post-run was similar to the pre-run aliquot, and its isotopic composition was the same as that of the working standard (within the relatively small amount of fractionation due to sample handling, as discussed below). Finally, the length of time the discharge was run (and the gas collected in the Russian doll trap) was varied between 2.5 and 45 minutes. The yield of N_2O scaled approximately linearly with the collection time, and the resulting measurements of the isotopic composition were identical within the error expected due to (1) slight differences in discharge and flow/pressure conditions, (2) small amounts of isotope fractionation due to sample handling, and (3) measurement precision. Details of the error analysis are discussed in the next section.

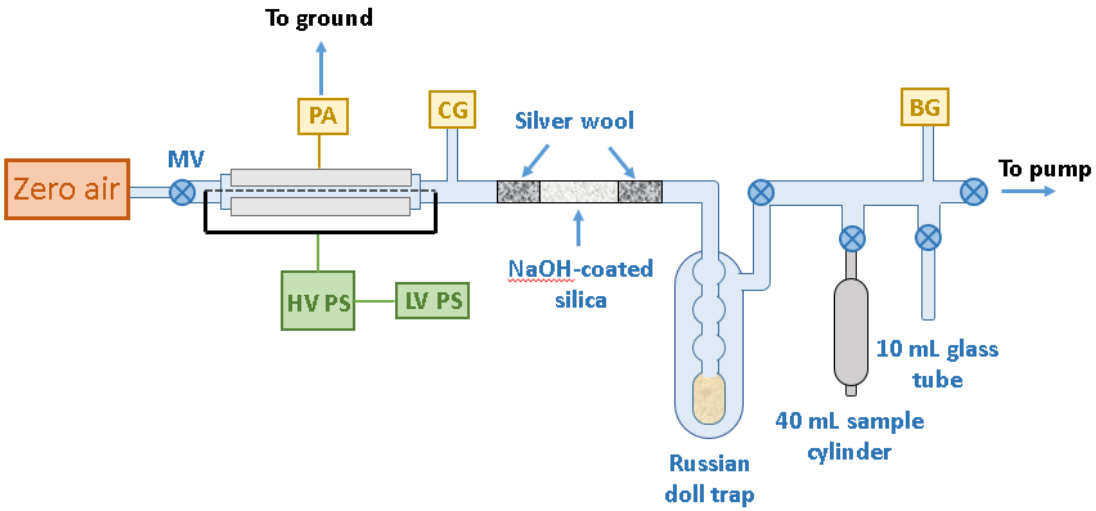

Figure 5.1. Schematic of the experimental apparatus. MV = metering valve; LV PS = low voltage power supply; HV PS = high voltage power supply; PA = picoammeter; CG = convection gauge; BG = capacitance manometer (Baratron gauge).

5.2.2 IRMS analysis

The isotopic composition of N_2O generated in the corona discharge apparatus was measured by a Finnigan MAT 252 Isotope Ratio Mass Spectrometer (IRMS) operated

in continuous flow mode with an online PreConcentrator-Gas Chromatography inlet system (PreCon-GC-IRMS). To measure aliquots of the low-pressure, pure N_2O samples, some modifications were made to the standard protocol for measuring whole air samples in our laboratory (*e.g.*, Refs. 3 and 81). Since the 40 mL sample cylinders contained large amounts of pure N_2O at low pressures, direct injection into the online GC was not feasible. Instead, sample aliquots were transferred into 20 mL glass flasks on a gas transfer vacuum line, which were then mounted onto the PreCon, and the automated program for measuring whole air samples was modified to include build-up of helium in the 20 mL flask to at or above atmospheric pressure (as described in Ref. 82).

Specifically, samples were prepared by taking aliquots from the 40 mL cylinders on a glass-manifold vacuum line equipped with transfer ports and a diffusion pump. Depending on the amount of N_2O generated in the discharge run, and on the amount remaining after previous aliquot transfers, various glass flasks (20 mL or 100 mL) were attached to one or two transfer ports as ballast volumes, as well as the 20 mL sample transfer flask for IRMS analysis. The sample cylinder was opened to the 20 mL sample flask and to various ballast volumes to obtain a suitable amount of N_2O in the sample flask for IRMS analysis (0.5-3 mol, based on previous calibrations). The 40 mL sample cylinder was then isolated, removed from the manifold, and stored for further analyses on subsequent aliquots. The above transfer steps were repeated with the remaining N_2O in the sample cylinder in order to prepare another aliquot in the 20 mL sample flask. Multiple aliquots were taken for IRMS analysis, both for replicate measurements as well as the requirement of two separate aliquots to determine the site-specific nitrogen isotopic composition (see below). Tests of the ballast volume transfer procedure using N_2O reference gas showed that this procedure may result in isotope fractionation of up to ±2‰. Fractionation of this magnitude due to sample handling would be unacceptably large for many applications, but it was deemed acceptable in our search for an isotopic fingerprint (*i.e.*, deviations larger than 2‰ relative to the reactant N_2 and O_2) for N_2O produced in the corona discharge experiments in this study.

Figure 5.2 shows a schematic of the continuous-flow PreCon-GC-IRMS for measuring the isotopic composition of N_2O. For each isotopic composition measurement, the 20 mL sample flask containing 1-3 nmol N_2O from the corona discharge experiment was mounted on the PreCon. Following prompts from the automated sample preparation program, the upstream valve to the sample flask was opened first in order to pressurize it to ~800 Torr (requiring ~50 secs at a He flow rate of ~25 mL/min).[82] Then, the downstream valve to the sample flask was opened, allowing N_2O in the sample flask to be entrained in the flow of He which then passes through a chemical trap containing $MgClO_4$ (Sigma-Aldrich, St. Louis, MO) to remove H_2O, and NaOH-coated silica (Ascarite; Sigma-Aldrich, St. Louis, MO) to remove CO_2, followed by another $MgClO_4$ trap to remove the H_2O generated by the NaOH trap. The apparatus first operates in "vent mode" in which the N_2O condenses into a metal U-tube immersed in LN2. Then the unit switches to "loop mode" in which the first trap is warmed and the condensables are frozen into a second trap immersed in LN2; this trap contains a capillary with much smaller volume and serves to cryo-focus the N_2O for injection into the GC column. The cryo-focused N_2O is injected into the GC (Poraplot Q, 25 m long, 25°C) and separated from other impurities in the sample such as residual CO_2. Eluting species enter the open

split region, a system of capillaries for transferring gas to the IRMS. Another open split capillary system is used to transfer N_2O from a reference cylinder to the IRMS.

The IRMS (Finnigan MAT 252) consists of an ionization region in which gases are ionized by electron impact and the resulting ions are focused with ion optics into a magnetic analyzer. The ion trajectories follow curved paths according to their mass-to-charge (*m*/*z*) ratio, and are collected by Faraday cups set in a cup configuration for *m*/*z* 44, 45, and 46. These ratios correspond to $^{14}N^{14}N^{16}O^+$; a combination of $^{15}N^{14}N^{16}O^+$, $^{14}N^{15}N^{16}O^+$, and $^{14}N^{14}N^{17}O^+$; and $^{14}N^{14}N^{18}O^+$, respectively. The measured ratios of voltages at *m*/*z* 45 and 46 relative to *m*/*z* 44 are compared to those measured for an N_2O standard (our laboratory reference gas), which is measured several times before and several times after the sample elutes from the GC and enters the IRMS. The results are then converted into the isotopic composition relative to international standards.

Because the abundances of rare isotopes that occur in nature are typically very small, the isotopic composition is often expressed in terms of "δ values" in "per mil" (‰) – *i.e.*, parts per thousand deviations from an international standard, as shown in Equation (1) for $\delta^{15}N$.

$$(1)\ \delta^{15}\mathrm{N} = \left(\frac{\mathrm{R}^{15}\mathrm{N}_{\mathrm{sample}}}{\mathrm{R}^{15}\mathrm{N}_{\mathrm{standard}}} - 1\right) \times 1000$$

Equation (1) yields the "average" or "bulk" $^{15}N/^{14}N$ ratio in a sample of N_2O. It is also possible to measure the ratio of $^{15}N/^{14}N$ in the NO^+ fragment formed by dissociative ionization of N_2O in the mass spectrometer (which is ~30% of the N_2O^+ parent ion signal). Using both the first measurement of the bulk $^{15}N/^{14}N$ ratio for N_2O^+ ions and this additional measurement of NO^+ ions on a separate aliquot of the N_2O sample, one can derive the nitrogen isotopic composition at the central (α) position (*i.e.*, $^{14}N^{15}NO$) and the terminal (β) position (i.e., $^{15}N^{14}NO$).[83,84] The $\delta^{15}N^{\alpha}$ and $\delta^{15}N^{\beta}$ values are known as the "site-specific" isotopic composition. For measurements of the site-specific isotopic composition of N_2O, a second aliquot of a given sample must be run, usually on the day after measurements of the bulk isotopic composition. The separate NO^+ run is needed because the cup configurations on the older Finnigan MAT 252 IRMS had to be set at the factory before the benefits of making simultaneous measurements of *m/z* 30 and 31 ratios, corresponding to $^{14}N^{16}O^+$ and $^{15}N^{16}O^+$ respectively, and of *m/z* 44, 45, and 46 were anticipated.

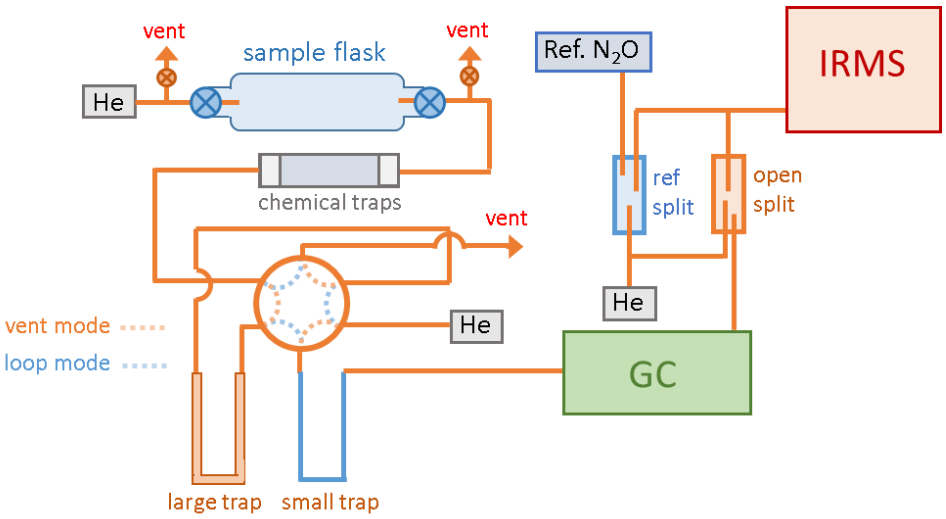

Figure 5.2. Schematic of the Finnigan MAT Continuous Flow-PreCon-GC-IRMS for N_2O isotopic composition measurements.

Using the relationships in Equations (2)-(6) below, the measured isotope ratios for the sample and the working standard are converted to $\delta^{15}N$, $\delta^{15}N^{\alpha}$ and $\delta^{18}O$ values against international standards: "air N_2" for $\delta^{15}N$, "air O_2" for $\delta^{18}O$, and "air N_2" for $\delta^{15}N^{\alpha}$ and SP (for which we use the currently accepted air N_2 standard of Toyoda and Yoshida,[81,83] abbreviated here for clarity as "T&Y air N_2 scale"). In Equations (2)-(6), ${}^{x}R^{y}$ represents the isotope ratios of ${}^{15}N^{\alpha}$, ${}^{15}N^{\beta}$, ${}^{17}O$, or ${}^{18}O$; A and B are coefficients representing the covariance of ${}^{17}O$ with ${}^{18}O$ (a mass-dependent relationship of ~0.515); and s is a measured "scrambling" coefficient which is the fraction of NO^{+} fragments containing N from the terminal position of N_2O (8.04% for our IRMS). See Ref. 82 for further details on these calculations.

(2) $${}^{45}R = {}^{15}R^{\alpha} + {}^{15}R^{\beta} + {}^{17}R$$

(3) $${}^{46}R = \left({}^{15}R^{\alpha} + {}^{15}R^{\beta}\right){}^{17}R + {}^{18}R + {}^{15}R^{\alpha}{}^{15}R^{\beta}$$

(4) $${}^{17}R = A\left({}^{18}R\right)^{B}$$

(5) $${}^{31}R = \frac{s{}^{15}R^{\alpha} + (1-s){}^{15}R^{\beta} + {}^{15}R^{\alpha}{}^{15}R^{\beta}}{1 + s{}^{15}R^{\beta} + (1-s){}^{15}R^{\alpha}} + {}^{17}R$$

(6) $$\text{Site preference} = \text{SP} = \left(\frac{{}^{15}R^{\alpha}}{{}^{15}R^{\beta}} - 1\right) \times 1000 \approx \delta^{15}N^{\alpha} - \delta^{15}N^{\beta}$$

"Site Preference," defined in Equation (6) as simply the arithmetic difference between $\delta^{15}N^{\alpha}$ and $\delta^{15}N^{\beta}$ in a sample, is commonly used by ecologists and microbiologists; in any form, the "relative enrichments" or "Site Preference" (SP) can be useful since it is often independent of substrate (or reactant) isotopic composition, which may be unknown in field studies (*e.g.*, Refs. 35–37).

Based on previous studies and long-term evaluation of our IRMS measurement precision for N_2O in whole air samples,[3,26,81] single measurement precisions are ±0.2‰ for $\delta^{15}N$, ±0.25‰ for $\delta^{18}O$, ±0.8‰ for $\delta^{15}N^{\alpha}$, and ±1.0‰ for $\delta^{15}N^{\beta}$ (1σ). For the N_2O discharge studies, there are additional sources of systematic error to consider when comparing measurements of the isotope composition from separate discharge runs under different conditions, or even when comparing replicate IRMS runs of different aliquots of the same N_2O discharge sample, as described below.

First, it is difficult to reproduce pressure and flow rate conditions in the corona discharge cell, and to reproduce discharge energies for the energy-dependent runs in Experiments #1a-1f. Second, systematic isotope fractionation is possible due to sample handling (including both the sample collection procedure on the discharge line and the transfer of very low pressure samples from the 40 mL to 20 mL flasks with various ballast volumes, as described in Section 5.2.1). In tests, the amount of isotope fractionation due to all sample handling ranged from almost no fractionation to as large as 3‰ for $\delta^{18}O$; this upper limit is based on the maximum spread in N_2O isotope measurements of samples from (a) running an aliquot of N_2O reference gas through both the entire discharge cell collection procedure (with the discharge off) and the sample aliquot transfer procedure (described above), (b) varying discharge/N_2O collection times between 2.5 and 45 minutes, and (c) tests of the aliquot sampling procedure using an aliquot of N_2O reference gas. This upper limit is also consistent with the observed scatter between different experiment runs under similar conditions. Where possible, runs under similar conditions are averaged together, and measurement differences less than 3‰ for $\delta^{15}N$ and $\delta^{18}O$ and less than 5‰ for $\delta^{15}N^{\alpha}$ are considered to be within experimental uncertainty. These averages are presented and discussed in the Results and Discussion section. For completeness, measurements for individual runs are given in tables and plots in Appendices 5B to 5D.

To assess the isotope fractionation associated with N_2O formation/destruction in a corona discharge, the isotopic composition of N_2O produced in the discharge must be compared with the nitrogen and oxygen isotopic composition of the reactant zero air. The zero air used in the experiments consists of compressed N_2 and O_2 taken from ambient air. The isotopic composition of the reactant air is assumed to be ~0‰ for both $\delta^{15}N$ and $\delta^{18}O$, based on previous estimates of 1) ^{15}N fractionation introduced in a high-purity N_2 cylinder by the commercial air reduction process[42,85] of 0 to 2‰ and 2) ^{18}O fractionation introduced in a high-purity O_2 cylinder by the commercial air reduction process of <3‰.[42,86] This assumption is reasonable given the overall random and systematic experimental error, estimated above as ±3‰, of our N_2O isotopic composition measurements for a given sample aliquot.

In the results section below, the N_2O discharge results are also compared with the isotopic composition of tropospheric N_2O collected at UC Berkeley and measured at least once each day that IRMS measurements were performed. Appendix 5C gives a summary of results for tropospheric N_2O. The average value for $\delta^{15}N$ is 5.9±0.3‰ (1σ, N=14) and the average for $\delta^{18}O$ is 44.0±0.2‰. These values are consistent with other recent measurements of the isotopic composition of tropospheric N_2O,[3,81,87] and the standard deviations are consistent with the estimated long-term precision of IRMS measurements for our laboratory, noted above.[26] The average value for $\delta^{15}N^{\alpha}$ is 16.8±1.1‰ on the T&Y air N_2 scale, and 1.1±1.2‰ on the tropospheric N_2O "scale"

that is used as a transfer standard among the N_2O isotope community,[81] indicating that the measured site-specific isotopic composition of UC Berkeley campus air is representative of that for tropospheric N_2O.

5.3 Results and Discussion

Results for the measurements of the isotopic composition of N_2O produced in corona discharge as a function of discharge cell pressure and discharge voltage are summarized in Table 5.2, with detailed results for each experimental run compiled in Appendix 5B. In general, the yield of N_2O increased with increasing discharge cell pressure and voltage, and ^{15}N and $^{15}N^{\alpha}$ were enriched and ^{18}O depleted relative to their abundances in air N_2 and air O_2. There are deviations from these generalizations, however, especially at the lowest pressures and discharge voltages, as discussed below. At the highest pressures run to date, the ^{15}N and $^{15}N^{\alpha}$ enrichments and ^{18}O depletions are quite large: as high as +32 and +77‰ for $\delta^{15}N$ and $\delta^{15}N^{\alpha}$ respectively, and as low as -71‰ for $\delta^{18}O$. These changes are an order of magnitude or more larger than the variations in isotopic composition of N_2O measured at the surface or in the upper troposphere, and are distinct from the background tropospheric N_2O isotopic composition.[3,81]

The following sections discuss **(1)** the dependence of the N_2O isotopic composition on discharge cell pressure and discharge voltage; **(2)** a comparison of the present results with previous laboratory measurements of the yields and ^{15}N enrichments of nitrogen atoms or unspeciated "nitrogen oxides"; **(3)** possible mechanisms and isotope effects for N_2O production and destruction pathways in a corona discharge that may be consistent with the new laboratory data; and **(4)** potential atmospheric applications, including the possibility of distinguishing on local to regional scales whether the enhanced N_2O concentrations observed recently in the upper troposphere[22,23] are due to lofting of soil or ocean emissions, biomass burning, or recent lightning activity.

5.3.1 Dependence of N_2O isotopic composition on pressure and discharge voltage

The yield and isotopic composition of N_2O from the corona discharge as a function of discharge cell pressure at a fixed discharge voltage of 5.0 kV are shown in Figure 5.3 for both the flowing zero air (circles) and static zero air (triangles) conditions. For the flowing zero air experiments, the N_2O yield increased approximately linearly with pressure. The yield at 10 Torr under static conditions was significantly lower (by a factor of 16) than the yield at 10 Torr under flowing conditions; this is presumably due to the larger influence of N_2O destruction (*e.g.*, reactions i through l in Table 5.1) over the 15 minute residence time in the discharge cell for static runs (relative to the estimated 70 ms residence time for the flowing 10 Torr runs; see Appendix 5A). At all pressures, the central nitrogen atom and the average over the two nitrogen atom positions in N_2O from the corona discharge were enriched in ^{15}N relative to the zero air reactant N_2. N_2O produced in the static runs at 10 Torr was less enriched in ^{15}N than the corresponding flowing runs at 10 Torr. The trends in the $^{18}O/^{16}O$ ratios are more complex. At pressures below 1 Torr, ^{18}O in N_2O from the corona discharge was enriched relative to the zero air reactant O_2, while at pressures above 1 Torr large ^{18}O depletions were observed. The divergent behavior of the isotopic composition below 1 Torr relative to higher pressures in Figure 5.3b-d might be related to the shifting spatial

balance of the corona discharge. Fewer electrons are present in the discharge at low pressures, but they have higher kinetic energy and can travel farther, leading to an increase in the size of the region of ionization;[88] this could produce lower yields of N_2O with smaller enrichments (or depletions) since, as discussed further below, reaction rates at higher energies are less sensitive to isotope effects. Isotope-isotope plots for the pressure-dependent data in Figure 5.3 are shown in Figure 5.4; these plots reduce some of the scatter in Figure 5.3, yielding linear correlations between $\delta^{15}N^{\alpha}$ and $\delta^{15}N$ of slope 2.1±0.1 (1σ; $R^2 = 0.98$) and between $\delta^{18}O$ and $\delta^{15}N$ of -2.8±0.3 (1σ; $R^2 = 0.92$).

Table 5.2. Summary of N_2O yields and isotopic composition as a function of discharge voltage and downstream pressure.

# samples	Voltage (kV)	Pressure (Torr)[a]	Yield N_2O (nmol)[b, c]	$\delta^{15}N$ (‰ vs. air N_2)	$\delta^{18}O$ (‰ vs. air O_2)	$\delta^{15}N^{\alpha}$ (‰ vs. T&Y air N_2)	$\delta^{15}N^{\beta}$ (‰ vs. T&Y air N_2)	SP (‰ vs. T&Y air N_2)
3[d]	5.0	0.523±0.025	1108±202	3.7±1.0	23.4±1.5	10.0±1.3	-2.3±4.0	12.4±5.3
1	3.5	0.570	944	3.5±0.1	23.8±0.3	8.4±1.5	-1.5±1.4	9.9±2.1
1	1.5	0.580	1073	4.0±0.1	24.1±0.1	3.1±1.5	5.1±1.5	-2.0±2.1
2	1.0	0.545±0.007	910±130	2.7±0.1	22.9±0.8	1.8±6.9	3.6±6.8	-1.7±13.7
3	0.50	0.563±0.006	739±33	0.7±1.0	18.2±0.9	0.1±2.8	1.3±2.0	-1.1±4.4
1	0.25	0.580	363	-0.4±0.8	2.6±0.1	-9.4±2.0	8.8±3.6	-18.2±4.1
1	5.0	0.065	263	5.2±0.1	12.3±0.1	19.5±1.6	-9.4±1.5	28.9±2.2
1	5.0	0.220	860	2.8±0.2	31.1±0.2	15.8±1.6	-10.6±1.5	26.4±2.2
1	5.0	0.380	689	3.0±0.1	28.9±0.2	10.8±1.6	-5.0±1.4	15.8±2.1
1	5.0	0.865	1090	6.2±0.2	3.3±0.3	16.7±1.6	-4.6±1.4	21.4±2.1
1[e]	5.0	4.720[f]	4305	32.2±0.1	-71.0±0.6	77.2±1.7	-13.8±1.4	91.1±2.2
2[e]	5.0	9.75±0.02[f]	7969±817	32.5±2.6	-43.1±1.3	70.7±0.1	-6.2±5.1	76.8±5.1
2	5.0	9.77±0.11[f,g]	499±192	17.9±1.1	-44.4±3.0	44.9±3.9	-9.5±1.7	54.4±5.6

[a] Indicates convection gauge pressure reading downstream of discharge cell. [b] Calculated using the final pressure in a calibrated volume of the gas separated from the ethanol slush. [c] Average and 1σ standard deviation of all samples for each condition when uncertainties are given. [d] Includes data point for -75°C ethanol slush. [e] Sample from one run was collected for 5 mins instead of 15; the yields from these runs were multiplied by 3 to compare with the 15 minute runs. [f] Indicates absolute pressure reading on Baratron gauge. [g] Performed under static pressure.

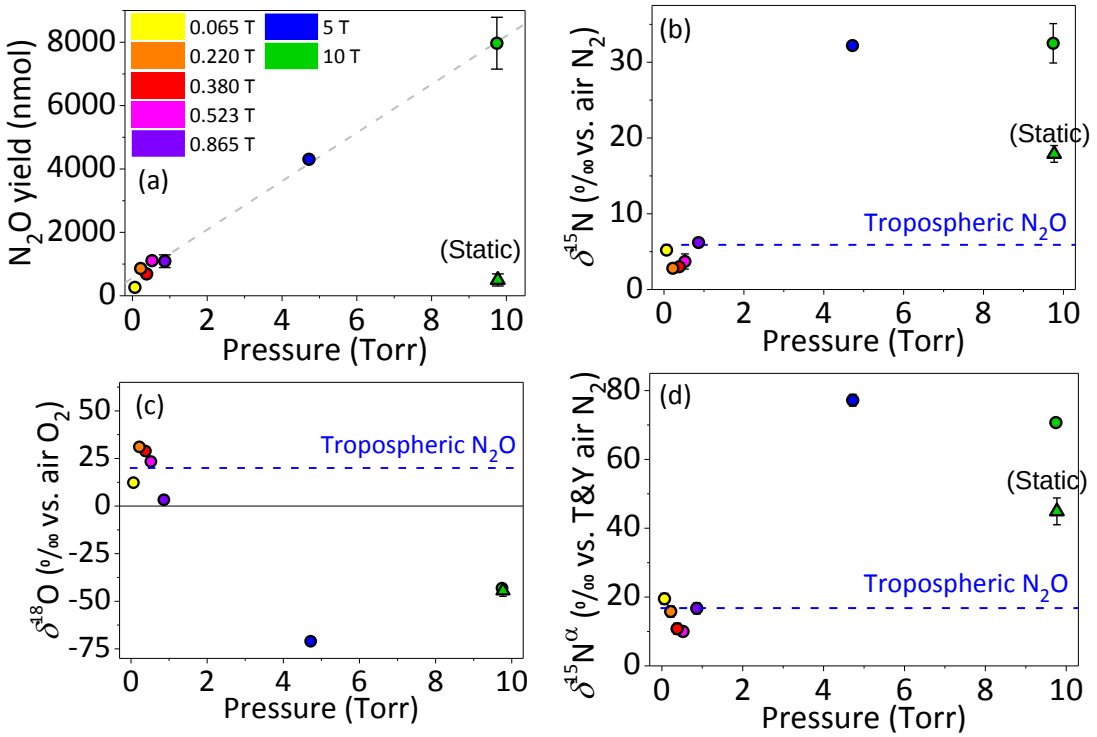

Figure 5.3. Measured N_2O yields (a) and N_2O isotopic composition (b-d) as a function of corona discharge cell pressure for experiments at a constant discharge voltage of 5.0 kV (#1a and #2-4); (b) $\delta^{15}N$ (‰ vs. air N_2), (c) $\delta^{18}O$ (‰ vs. air O_2), (d) $\delta^{15}N^{\alpha}$ (‰ vs. air N_2 on Toyoda and Yoshida[89] scale, or T&Y air N_2). Triangles represent the average yield and isotopic composition for the two static zero air runs at 10 Torr (#4); circles represent the flowing zero air experiments (#1a, #2-3), either individual runs or averages if N > 1. Error bars are 1σ standard deviations of the averages. Dashed line in (a) represents a linear fit to all data except the static runs. For reference, the average isotopic composition of tropospheric N_2O (see Appendix 5C) is shown as blue dashed lines, and the reactant zero air has an isotopic composition of 0 ± 2‰ for $\delta^{15}N$, $\delta^{15}N^{\alpha}$, and $\delta^{18}O$ on the air N_2 and air O_2 scales (see text).

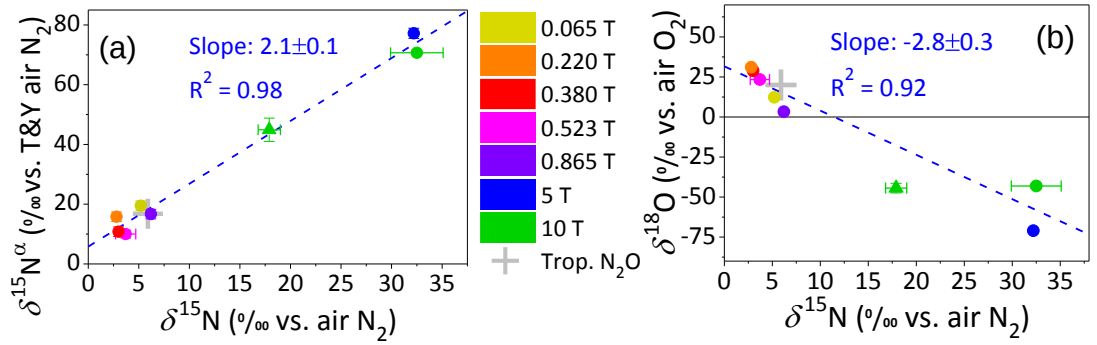

Figure 5.4. Isotope-isotope plots for (a) $\delta^{15}N^{\alpha}$ vs. $\delta^{15}N$ and (b) $\delta^{15}N$ vs. $\delta^{18}O$ for the results shown in Figure 5.3. Triangles represent the static pressure runs at 10 Torr (#4). Blue dashed lines represent least-squares linear fits to all data points except the static experiments. (The slopes from the δ-value regressions are the same as those from the more formal ln-ln isotope relationships to within the 1σ uncertainties given.)

The yield and isotopic composition of N_2O from the corona discharge experiments as a function of discharge voltage at a constant cell pressure of ~0.5 Torr are shown in Figure 5.5. (No static runs were performed at 0.5 Torr.) The N_2O yield increases non-linearly with discharge energy, rising rapidly between 0.25 kV and 0.50 kV and reaching a plateau (within the noise) at about 1.0-1.5 kV. This behavior, along with the noticeably weakened glow of the discharge at the lowest voltages in these experiments, may reflect the fact that the rate of electron impact reactions in the corona discharge ionization region is expected to decrease with decreasing voltage.[88] The values for $\delta^{18}O$ of N_2O behave similarly to the yields: at the lowest voltage (0.25 kV), $\delta^{18}O$ of N_2O is within a few per mil of the reactant O_2, then increases rapidly to ~18‰ at 0.5 kV, and reaches a plateau of ~23‰ at 1.0-1.5 kV and above. The values for $\delta^{15}N$ of N_2O also increase non-linearly with increasing discharge voltage, though they arguably begin to rise above the reactant N_2 isotopic composition at higher discharge voltages compared with the $\delta^{18}O$ values. The values for $\delta^{15}N^{\alpha}$ also increase with discharge voltage, but the trend appears more linear than that for the bulk $\delta^{15}N$ values, and actually dips below the reactant isotopic composition at the lowest voltage; however, it is unclear whether this one run is statistically different from the reactant gas isotopic composition of 0‰, given the low N_2O yield and thus potentially larger issues for $\delta^{15}N^{\alpha}$ due to sample handling fractionation, and given some large scatter in $\delta^{15}N^{\alpha}$ results at higher discharge energies that appear to average out when there are replicate runs. Isotope-isotope plots for the voltage-dependent data in Figure 5.5 are given in Figure 5.6, which clearly shows that the isotopic composition of N_2O at the lowest discharge voltage deviates from the trend at higher voltages. A possible explanation for the sharp rise in enrichments above 0.25 kV in ^{18}O and above 0.5 to 1.0 kV for ^{15}N in Figure 5.5 is that these discharge energies correspond to energetic thresholds for reactions that have large isotope effects, such as the dissociation of O_2 (5.15 eV for $O_2 \rightarrow 2O(^3P)$ and 7.1 eV for $O_2 \rightarrow O(^3P)+O(^1D)$) and the dissociation of N_2 (9.79 eV for $N_2 \rightarrow 2N(^4S)$). Further speculation about implications of these results for reaction mechanisms is given in Section 5.3.3.

5.3.2 Comparison with previous experiments

The work reported in this chapter represents the first direct measurements by IRMS of the ^{15}N and ^{18}O isotopic composition of N_2O formed in a corona discharge. However, several previous investigations are relevant to this study and offer an interesting comparison.

Basov *et al.*[90] used a standard magnetic sector mass spectrometer to measure the ratio of ^{15}N to ^{14}N signals in NO formed in a pulsed glow electric discharge in a mixture of N_2 and O_2 at 20 Torr and 77 K. Extremely large enrichments of up to 2000% (20,000‰) were measured relative to their reactant N_2. In similar experiments, Manuccia and Clark[76] measured the ^{15}N isotopic composition of combined 'nitrogen oxides' (~90% N_2O, ~10% NO and NO_2) at pressures of ~0.5-6 Torr. To avoid isobaric interferences (*e.g.*, interference of the $^{15}NO_2^+$ signal by $H^{14}NO_2^+$ formed by ion-molecule reactions with residual H_2O in the ion source of the mass spectrometer), they converted all the nitrogen-containing species formed in the discharge to N_2 (with 90% conversion yields) and measured the isotopic composition of the resulting N_2. They found ^{15}N enrichments of up to 210‰ for the nitrogen oxides in 20:1 N_2:O_2 mixtures at 77 K, and concluded

that the extreme ^{15}N enrichments measured by Basov *et al.* were an artifact of protonation reactions in the mass spectrometer.

Manuccia and Clark[76] found that the total yield of nitrogen oxides in their experiments increased with pressure, which is consistent with our results. The increase in yield of nitrogen oxides with increased pressure is also consistent with previous investigations of NO production in an arc discharge by Wang *et al.*[91] and of NO and N_2O formed in a corona discharge in CO_2/N_2 mixtures by Nna-Mvondo *et al.*[92] Similar to our direct measurements of the isotopic composition of N_2O, Manuccia and Clark[76] measured increasing ^{15}N enrichments with increasing discharge cell pressure. They attributed the pressure dependence to the inverse relationship between pressure and the energy input per reactant molecule: the higher the pressure, the lower the energy input per reactant molecule for a given discharge voltage, and the lower the energy per reactant molecule, the larger the ^{15}N enrichments. This dependence likely reflects the fact that when molecules can access higher energy states, their reaction rates generally depend less sensitively on small differences in vibrational frequencies that lead to isotope effects. In the closest conditions to our experiments, Manuccia and Clark found ^{15}N enrichments of ~130‰ in the sum of N_2O, NO, and NO_2 in an air-like N_2:O_2 mixture at 300 K at pressures near 3 Torr and ~0.01 eV per reactant molecule. This ^{15}N enrichment is larger than the largest value of 32‰ for $\delta^{15}N$ of N_2O at 5 and 10 Torr in the present study; however, the discharge conditions in this work lead to larger estimated energy inputs per reactant molecule of ~0.1-0.2 eV (see Appendix 5A). In light of the above points and similarities, we predict that decreasing the average energy per reactant molecule by increasing the pressure further in our experiments may lead to larger ^{15}N enrichments.

A number of experimental differences between (or uncertainties in) the Manuccia and Clark study and in this work may also account for some of the differences in ^{15}N enrichments. In addition to their measurement of the ^{15}N enrichment in the sum of nitrogen oxides, their reported 90% conversion to N_2 (rather than 99.9% conversion) suggests that isotope fractionation may affect their isotope composition. Using a traditional magnetic sector mass spectrometer rather than an isotope ratio mass spectrometer designed to make precise measurements at natural isotope abundances adds additional uncertainties to their ^{15}N enrichments. Given these uncertainties in addition to the large uncertainty in the estimated flow rates and therefore energies per reactant molecule in this work, the ^{15}N results shown in Figures 5.3 to 5.6 can be considered roughly consistent with the trends in ^{15}N enrichments and relative yields reported by Manuccia and Clark. Thus, since the measured trends with pressure and energy are similar, the Manuccia and Clark results can likely be used as a guide for further systematic study of the pressure, energy, and flow rate dependence of the isotopic composition of N_2O formed in our corona discharge apparatus.

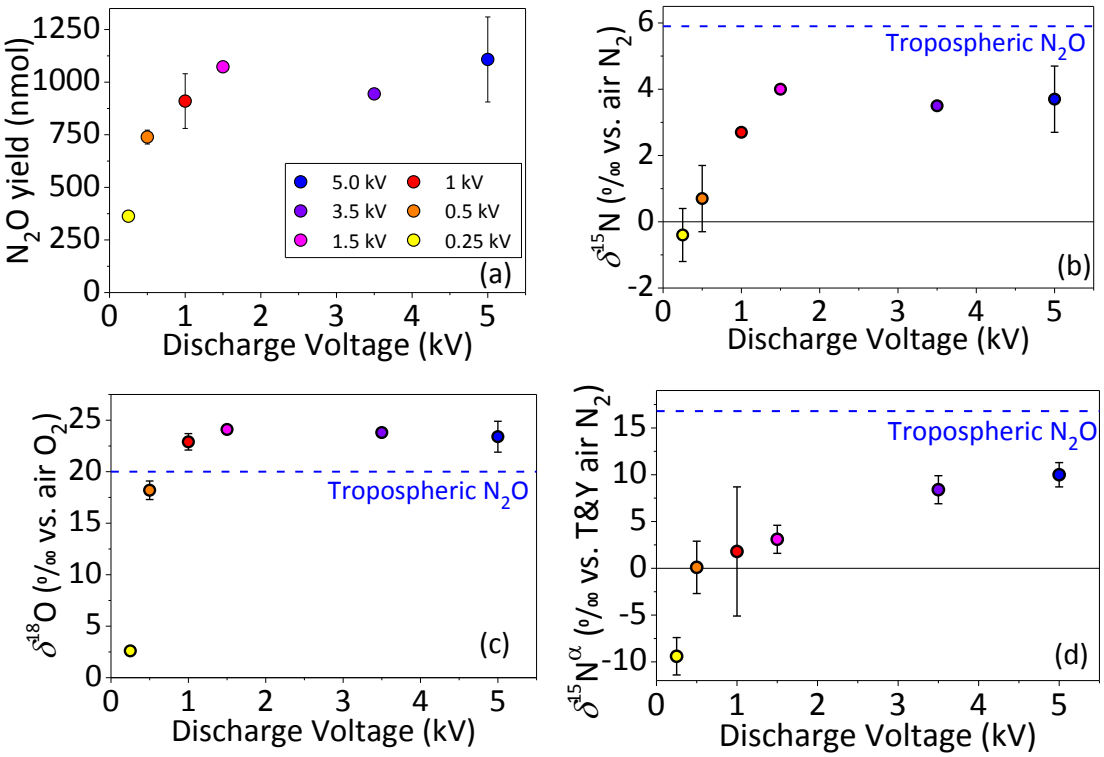

Figure 5.5. Measured N_2O yields (a) and N_2O isotopic composition (b-d) as a function of discharge voltage at a constant pressure of ~0.5 Torr (#1a-1f); (b) $\delta^{15}N$ (‰ vs. air N_2), (c) $\delta^{18}O$ (‰ vs. air O_2), (d) $\delta^{15}N^{\alpha}$ (‰ vs. T&Y air N_2). Average values for current tropospheric N_2O (see Appendix 5C) are shown as dashed lines.

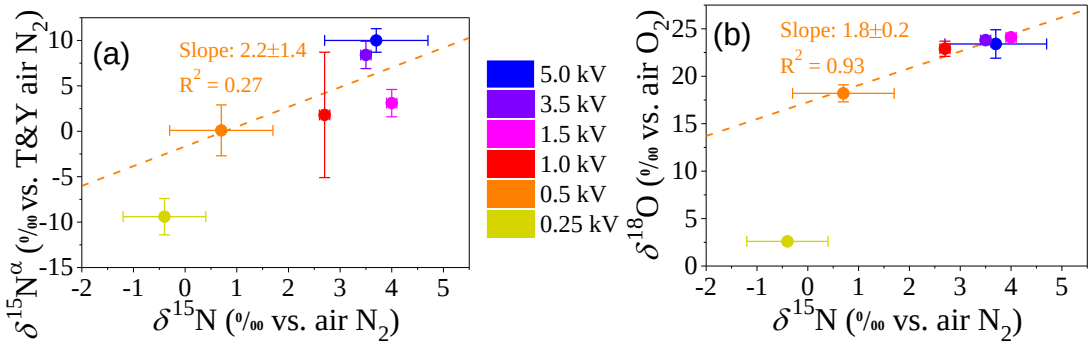

Figure 5.6. Isotope-isotope plots for (a) $\delta^{15}N^{\alpha}$ vs. $\delta^{15}N$ and (b) $\delta^{15}N$ vs. $\delta^{18}O$ for the results shown in Figure 5.5. Orange dashed lines represent least-squares linear fits to all data points except 0.25 kV; see text. (The slopes from the δ-value regressions are the same as those from the more formal ln-ln isotope relationships to within the 1σ uncertainties given.)

More recently, Gorshunov and Gudenko[75] used electron paramagnetic resonance to measure the ^{15}N abundances in nitrogen atoms after flowing N_2 was subjected to pulsed electric discharge at room temperature and pressures of 3-6 Torr, as a function of flow rate through the discharge tube. At the lowest flow rate of ~40 cm^3 s^{-1}, they measured

30-fold enrichments (29,000‰) in ^{15}N relative to the reactant N_2.[75] They found that the enrichments decreased rapidly with increasing flow rate, to ~400‰ at flow rates near 500 cm^3 s^{-1} and a minimum of ~150‰ at the highest flow rate of ~2000 cm^3 s^{-1}. Comparing with our measurements for N_2O (Appendices 5A and 5B), we do measure an inverse correlation between the flow rate and ^{15}N enrichments in N_2O: ^{15}N enrichments of ~1-5‰ at flow rates of ~3700 cm^3 s^{-1} (corresponding to <1 Torr) increasing to ~32‰ ($\delta^{15}N$) and 77‰ ($\delta^{15}N^{\alpha}$) as the flow rate drops to ~500 cm^3 s^{-1} (corresponding to 5-10 Torr). Furthermore, the experiments by Gorshunov and Gudenko were performed at similar electrical energies (corresponding to 0.01-0.1 eV per molecule)[75] to those of Manuccia and Clark (0.001-0.1 eV per molecule).[76] Based on the discussion of the Manuccia and Clark study above, the lower energy input per molecule relative to our work might be expected to produce higher ^{15}N enrichments. Finally, Gorshunov and Gudenko measured enrichments in ^{15}N atoms, not nitrogen oxides, and in fact no nitrogen oxides could form since their experiments were performed in N_2 only. It is intriguing, however, that the trends in the ^{15}N enrichments with flow rates and energies are similar between our two studies, and could be interpreted to mean that large ^{15}N enrichments in the nitrogen atom pool might lead to large (albeit smaller) enrichments in the N_2O produced in the discharge when oxygen is also present.

For completeness, we note that, to our knowledge, the only other study of the isotopic composition of nitrogen oxides produced in electric discharges is that of Hoering in 1957.[93] In those experiments, air flowed through a sealed Pyrex tube in which a spark was produced by a 10 kV voltage across platinum or tungsten electrodes separated by ¼ inch; the flow of air then passed through a solution of 0.1 M NaOH. The ozone produced in the spark was presumed sufficient to oxidize all the nitrogen oxides to nitrate ions in solution, which were then collected, reduced to NH_3, oxidized to N_2, and analyzed for $\delta^{15}N$. Values ranged from -0.5‰ for the tungsten electrodes to 1.4‰ for the platinum electrodes on the air N_2 scale. Hoering speculated that the high effective temperature of the spark discharge prevented significant isotopic fractionation relative to the reactant N_2 in the nitrogen oxides produced. The chemistry occurring in such high energy spark discharge experiments is expected to be similar to the chemistry in high energy lightning strikes or flash channels, which are known to produce mostly NO_x; this is likely to be very different from the lower energy corona discharge region surrounding the hot channel or in intracloud discharges where N_2O and ozone are formed (*e.g.*, Refs. 44, 45). Thus, the isotopic composition of NO_x formed in high energy spark discharges[93] may be quite distinct from the isotopic composition produced in corona discharges, with larger isotopic fractionations potentially occurring in lower energy corona discharge channels.

In summary, our direct measurements of the isotopic composition of N_2O formed in a corona discharge as a function of pressure and discharge voltage are at least qualitatively consistent with the results of Manuccia and Clark, when the larger energy depositions per reactant molecule we estimate for our experiments are taken into account. Depending on pressure and energy conditions, the ^{15}N enrichments can be quite large, with possible ^{15}N enrichments on the order of +100‰. The ^{18}O isotopic composition, which has been measured for the first time in this study, shows depletions on the order of -50‰ at the highest pressures measured; oxygen isotopic fractionation could result from a number of processes in the discharge. In the next section, we

speculate on the possible reaction mechanisms for N_2O formation (and destruction) in a corona discharge that may be consistent with the isotopic composition of N_2O measured.

5.3.3 Isotopic insights into N_2O chemistry in a corona discharge

We expect that the large variations in the nitrogen and oxygen isotope composition and the yields of N_2O in these corona discharge experiments will provide new constraints on the mechanism(s) of N_2O formation and destruction in corona discharges. Future work is needed, particularly kinetics modeling (*e.g.*, Ref. 51) of the results presented here and of additional experiments in which the cell pressure, flow rate, and residence times are varied in a more independent manner than was possible in the experiments presented here. For now, we simply speculate on the nature of the isotopic constraints and what they may reveal about the mechanisms participating in N_2O formation and destruction.

Out of the various N_2O formation reactions in Table 5.1, those most likely to be relevant for our discharge experiments are the reactions listed in b, c, and d. These reactions have been confirmed and well-studied in the laboratory, have sufficiently large rate coefficients, and have been used in previous corona discharge modeling studies. Preliminary results from a kinetics model using the program Kintecus[94] with reactions, rate coefficients, and positive corona discharge parameters at room temperature and 1 atm zero air[51] suggest that N_2O production via Reaction b ($N + NO_2$) dominates over Reaction c ($N_2(^3\Sigma) + O_2$) and Reaction d ($O^1D + N_2 + M$) (A. A. Wiegel, personal communication). In the following discussion, we assess our results in the context of these three formation mechanisms and their potential isotopic signatures.

Figure 5.4a shows that the ^{15}N enrichments in N_2O are carried largely by the central nitrogen atom. As the cell pressure increases, the ^{15}N enrichment at the central nitrogen position ($\delta^{15}N^{\alpha}$) grows twice as fast as the average enrichment over the central and end positions ($\delta^{15}N$), with a slope of 2.1±0.1 ($R^2 = 0.98$). Such a site-specific enrichment could occur via Reaction b if one or more of the reactants is already enriched – if, for example, the NO_2 reactant is enriched in ^{15}N. NO_2 could be enriched in ^{15}N due to nitrogen isotope exchange with NO; this may be plausible since Walters *et al.*[95] recently measured a fractionation constant of ~35‰ for the reaction $^{15}NO + {}^{14}NO_2 \rightarrow {}^{14}NO + {}^{15}NO_2$. By similar arguments, nitrogen isotope exchange in the N + NO reaction might result in ^{15}N enrichments in NO relative to the $^{15}N/^{14}N$ ratio in atomic N produced by N_2 dissociation in the corona discharge. This series of enrichments, then, leading up to ^{15}N enrichments in NO_2, could conceivably result in large enrichments at the central nitrogen atom position in N_2O via Reaction b. Site-specific enrichments might also result from Reactions c and d, but only if the formation rate or stability of the new $N^{\cdots}O$ bond is enhanced for ^{15}N over ^{14}N. Without further scrutiny, the reactions in c and d seem less likely to produce a site-specific ^{15}N enrichment in N_2O, especially combined with the measured ^{18}O depletions.

Figure 5.4b shows that, as cell pressure increases, N_2O becomes progressively depleted in ^{18}O relative to ^{16}O. Considering the static experiments, one might think that the depletion in ^{18}O could be caused by sequestering of the heavy oxygen isotopes (^{17}O and ^{18}O) by ozone, due to the large, mass-independent kinetic isotope effects in the energy transfer ozone formation reaction ($O + O_2 + M \rightarrow O_3$).[96,97] In other words, the ^{18}O

depletion might be a reservoir effect in which the entire oxygen isotope pool, apart from ozone molecules produced and destroyed at steady-state in the discharge, becomes depleted in ^{18}O. However, the flowing 10 Torr experiments resulted in N_2O with the same $\delta^{18}O$ values as the static experiments. Unless ozone in the discharge reaches steady-state within the estimated residence time of about 70 ms for the 10 Torr flowing experiments, a reservoir effect leading to large ^{18}O depletions is not plausible. In addition, Chen and Davidson[88] calculate that two-thirds of the ozone may be produced by reactions involving electronically excited N_2 and O_2 (*e.g.*, Ref. 98). Since only the energy transfer mechanism for ozone formation is thought to produce the large, mass-independent enrichments in ozone,[96,97] ozone produced in the discharge may not even exhibit similar mass-independent enrichments in ^{17}O and ^{18}O. We also note that isotope exchange via the $NO + O_3$ reaction, which leads to mass-independent ^{17}O and ^{18}O enrichments in atmospheric NO_2, may or may not be relevant for the chemical and physical regimes of the discharge region which are potentially very different than the typical atmosphere. Rather, the large ^{18}O depletions in N_2O produced in the discharge may simply result from a series of normal primary kinetic isotope effects, in which ^{16}O atoms and molecules containing ^{16}O react faster than their ^{18}O analogues; these effects could exist for dissociation reactions as well as any of the N_2O formation reactions in Table 5.1; we will discuss ideas to test for these possibilities below.

Destruction of N_2O may also occur in the discharge region, particularly in the static experiments performed at 10 Torr. Yields of N_2O in the static runs were 16 times lower than for the flowing runs (regardless of whether LN2 was placed on the Russian doll trap during the discharge, allowing N_2O diffusing far downstream from the discharge cell to be frozen, or whether the LN2 was added to the trap at the end of the 15-minute discharge; see methods and Appendix 5B). We attribute the drop in yield in the static runs to N_2O destruction in the discharge regions during these runs, due to reactions such as i through l in Table 5.1. If this is the case, then the isotope effects in the participating N_2O destruction reactions appear to be very small or otherwise indistinguishable from those of the formation reactions; this is evident in the isotope-isotope plots in Figure 5.4, as well as in Figure 5.7, which shows the $\delta^{15}N^{\alpha}$ and $\delta^{15}N^{\beta}$ values for all runs versus $\delta^{18}O$. In fact, Figure 5.7 clearly summarizes the results presented in this chapter: as $\delta^{18}O$ of N_2O decreases, $\delta^{15}N^{\alpha}$ increases while $\delta^{15}N^{\beta}$ stays approximately the same (within the scatter). This behavior implicates the important effect of isotopic substitution on the rate and/or energetics of the $N^{\cdots}O$ bond forming (or breaking), either directly during formation of N_2O or during the series of reactions leading to N_2O formation.

The above considerations can be tested by adding potential ^{15}N, ^{17}O, and ^{18}O isotope effects into the positive corona discharge kinetics model of Chen and Davidson[88] and performing sensitivity studies. Additionally, measurements of the ^{17}O isotopic composition of N_2O formed in static and flowing corona discharge experiments will provide insight into the role ozone and its mass-independent isotope enrichments may play in producing the observed patterns of oxygen isotope fractionation in N_2O.

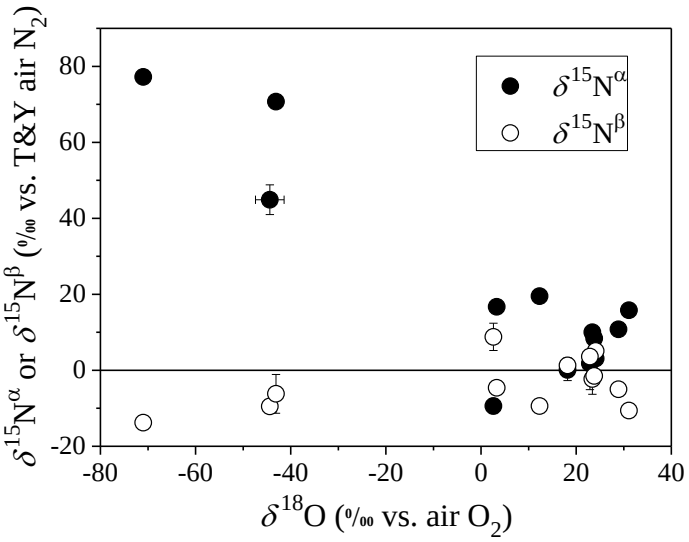

Figure 5.7. Isotope-isotope plot of $\delta^{18}O$ (vs. air O_2) against $\delta^{15}N^{\alpha}$ (vs. T&Y air N_2) and $\delta^{15}N^{\beta}$ (vs. T&Y air N_2) from Table 5.2 for all experiments.

5.3.4 Applications to atmospheric N_2O

Based on laboratory measurements extrapolated to the atmosphere, corona discharge is thought to contribute only a very small amount (~4×10^{-4} Tg y^{-1} or ~0.002%) to the total sources of N_2O to the atmosphere each year.[9] If the 29,000‰ enrichments in ^{15}N of nitrogen atoms relative to reactant N_2 measured by Gorshunov and Gudenko[75] existed in atmospheric corona discharges, such an isotopic signature could translate into enormous ^{15}N enrichments in N_2O, which might influence the global N_2O isotope budget or the small trends and seasonal and interannual variations in the N_2O isotope composition measured at the Earth's surface (*e.g.*, Ref. 3). However, our direct measurements of the isotope composition of N_2O produced by corona discharge in the laboratory suggest that these enormous enrichments are not likely.

Despite an anticipated small contribution to the global N_2O budget and N_2O isotope budget, however, the isotopic fingerprint shown in the isotope-isotope relationships for corona discharge N_2O under the conditions we have measured so far (Figure 5.4) is entirely distinct from the isotopic fingerprints of other N_2O sources. N_2O emitted from soils is highly depleted in both ^{15}N and ^{18}O, while residual N_2O in N_2O-depleted air returning from the stratosphere is highly enriched in both ^{15}N and ^{18}O and has a $^{15}N^{\alpha}$ vs. ^{15}N slope of 1.4.[3,26,99] The isotopic composition of N_2O from biomass burning, based on a single laboratory study,[41] appears to vary depending on the type of matter burned and on burn conditions (smoldering versus flaming); in the laboratory, its $\delta^{15}N$ value was similar to background N_2O with only a small site preference (*i.e.*, little difference between $\delta^{15}N^{\alpha}$ and $\delta^{15}N^{\beta}$), and $\delta^{18}O$ was similar to air O_2 (as might be expected for combustion), *i.e.*, ~23‰ lower than background N_2O. Based on this isotopic signature, if a plume of air influenced by biomass burning mixes into background tropospheric air, the isotopic composition of N_2O in the mixed air should show little to no change in $\delta^{15}N$, a decrease in $\delta^{15}N^{\alpha}$ and Site Preference, and a decrease in $\delta^{18}O$. Thus, these

isotope-isotope relationships for N_2O from soil emissions, the stratosphere, and biomass burning are all different from those for the N_2O produced in our corona discharge experiments, in which ^{15}N is enriched, $^{15}N^{\alpha}$ even more enriched (with a $\delta^{15}N^{\alpha}/\delta^{15}N$ slope of 2), and ^{18}O is depleted.

In addition to the isotope signature of N_2O from the corona discharge being distinct from that of other sources, it is also quite large. Thus, we expect that even very small changes in N_2O mixing ratios due to lightning activity may result in isotope variations that are large enough to measure and detect. By analogy, our laboratory has successfully made such N_2O isotope measurements in air collected in the upper tropical troposphere during the NASA TC4 mission and determined that biomass burning or another combustion source was responsible for the small (~1 ppbv) increase in N_2O mixing ratio. Whole air samples were collected across a plume at an altitude of 14 km in the upper tropical troposphere; even though the N_2O mixing ratio increased by a maximum of only 1 ppb, the $\delta^{15}N^{\alpha}$ and Site Preference values decreased by ~5 and ~9‰ respectively, and $\delta^{18}O$ decreased by ~2‰, while the $\delta^{15}N$ value did not change significantly.[81] The magnitudes of these variations are well above our detection limits and easily detectable. Since these changes matched the N_2O isotope signature expected from biomass burning/combustion (described above), the N_2O isotope data, combined with a suite of other tracer measurements and back trajectory calculations, led to the conclusion that the sampled plume was a mixture of combustion-influenced and polluted urban air that had been lofted by convection over the previous 24 hours, most likely over Panama City.[81]

Our lightning discharge laboratory results for the isotopic composition of N_2O suggest that, in a similar fashion, we may be able to distinguish local or regional enhancements in N_2O mixing ratios due to lightning versus those from biomass burning or from lofting of soil or ocean emissions. Such an application can help identify the source of the ~2-3 ppbv enhancements in N_2O mixing ratios observed in the tropics and subtropics in January and November of 2009 during the HIPPO mission.[22,23] Indeed, as discussed earlier, in situ N_2O mixing ratio measurements from the HIPPO mission and 'top-down' inverse modeling studies of atmospheric N_2O mixing ratios[14,15] all point to significantly larger emissions in the tropics and subtropics than previously assumed, yet the source of the elevated N_2O levels – biomass burning, soil emissions, or lightning – is unknown. Future measurements of the isotopic composition of the enhanced N_2O may help to unambiguously resolve the source of such enhanced N_2O levels across the tropics.

5.4 Conclusions

The bulk nitrogen ($\delta^{15}N$), site-specific nitrogen ($\delta^{15}N^{\alpha}$, $\delta^{15}N^{\beta}$), and oxygen ($\delta^{18}O$) isotope composition of N_2O produced in a corona discharge in dry air were measured as a function of pressure/flow rate and discharge voltage. Although the ^{15}N enrichments were not as large as some previous indirect experiments suggested,[75,76,90] the ^{15}N enrichments directly measured in N_2O were still quite large, with $\delta^{15}N$ values of up to +32‰ on the air N_2 scale and even larger ^{15}N enrichments measured at the central nitrogen site of up to +77‰ on the Toyoda and Yoshida[89] air N_2 scale at a discharge cell pressure of 5 Torr. A comparison of this work with the dependence of ^{15}N enrichments on energy deposition per reactant molecule in the Manuccia and Clark

study, in which ^{15}N enrichments in the sum of nitrogen oxides were measured, suggests that even larger ^{15}N enrichments may occur at higher discharge pressures in the laboratory (and the atmosphere) which correspond to lower energies per molecule. The oxygen isotopic composition of N_2O produced in a corona discharge is reported here for the first time, and shows the opposite trend – a large isotopic depletion in ^{18}O, reaching a minimum of -71‰ on the air O_2 scale.

These new direct corona discharge N_2O isotope composition measurements point to several applications. First, the isotopic composition measurements can be used to constrain the importance of various reaction pathways for forming N_2O in a corona discharge and their dependence on discharge conditions. For example, the large ^{15}N enrichments measured at the central nitrogen position may be consistent with the formation of N_2O by reaction of nitrogen atoms with NO_2. The large depletion in ^{18}O in both flowing and static pressure experiments may result from normal kinetic isotope effects in which ^{16}O isotopologues react faster than ^{18}O isotopologues in a series of reactions leading to the formation N_2O. Further investigation of the dependence of the N_2O isotopic composition on pressure, flow, and energy, combined with kinetics modeling of the sensitivity of the N_2O isotopic composition to various potential isotope effects, will provide a more complete picture of the mechanisms at play in our experiments, and may help to resolve the ongoing debate over the relative importance of various mechanisms leading to N_2O formation in electrical discharges.

Second, we have shown that the isotope signature of N_2O formed in a corona discharge is large and distinct enough to be used to identify the influence of lightning activity on N_2O in the atmosphere on local to (perhaps) regional scales. This application can be pursued immediately and may help resolve important current questions about the spatial and temporal variability of N_2O concentrations in the upper tropical troposphere and their causes. Specifically, our laboratory results show that the isotope-isotope relationships for N_2O produced in a corona discharge – similar to corona discharges in intra- and inter-cloud lightning – are distinct from those for N_2O from soil emissions, biomass burning, or transport of stratospheric air into the troposphere: ^{15}N is enriched, ^{15}N at the central nitrogen atom site is considerably more enriched (with a large Site Preference), ^{18}O is depleted. In contrast, ^{15}N and ^{18}O are generally depleted in N_2O produced from microbial activity in soils and the oceans, with a generally positive Site Preference; N_2O returning from the stratosphere is enriched in ^{15}N and ^{18}O, with a large Site Preference; and N_2O from biomass burning has ^{15}N similar to background tropospheric N_2O, little Site Preference (unlike background tropospheric N_2O), and ^{18}O similar to air O_2 (*i.e.*, depleted with respect to background tropospheric N_2O). Therefore, using a combination of measurements of $\delta^{15}N$, $\delta^{15}N^{\alpha}$, and $\delta^{18}O$ of N_2O and measurements of N_2O mixing rations in future atmospheric field campaigns will allow us to distinguish whether recent lightning activity or another source has influenced an air parcel, and thus may help to identify the source of frequent but transient N_2O observed in the upper tropical troposphere.[22,23]

Appendix 5A. Estimated flow rates and energy inputs

Table 5A.1. Summary of estimated flow rates and energy inputs for various experimental conditions.

Discharge voltage (kV)	Downstream pressure (Torr)	Flow rate (sccm)[a, b]	Flow rate (cm^3 s^{-1})	Residence time (s)	Energy input per molecule (eV)[c]
5.0	<1	233	3689	0.01	0.78
3.5	<1	233	3689	0.01	0.55
1.5	<1	233	3689	0.01	0.23
1.0	<1	233	3689	0.01	0.16
0.5	<1	233	3689	0.01	0.08
0.25	<1	233	3689	0.01	0.04
5.0	5	470	541	0.07	0.24
5.0	10	940	541	0.07	0.49

[a] Estimated assuming a linear pressure gradient downstream of the metering valve for flow experiments. [b] The error in the estimated flow rate, residence time, and energy input is mainly due to uncertainty in the valve flow coefficient and is about 50%. [c] Average energy input per molecule reactant (zero air).

Appendix 5B. Isotopic composition of N_2O formed in individual runs

Table 5B.1. Summary of N_2O isotopic composition for corona discharge experiments.

#	Discharge voltage (kV)	Downstream pressure (Torr)	Yield N_2O (nmol)[a]	$\delta^{15}N$ (‰ vs. air N_2)	$\delta^{18}O$ (‰ vs. air O_2)	N_b[b]	$\delta^{15}N^{\alpha}$ (‰ vs. T&Y air N_2)	$\delta^{15}N^{\beta}$ (‰ vs. T&Y air N_2)	SP (‰ vs. T&Y air N_2)	N_{ss}[c]
1a	5.0	0.500	1194	4.9±0.1[d]	25.0±0.3	2	9.1±1.5	0.5±1.4	8.6±2.1	3
1a-2	5.0	0.550	877	3.4±0.1	22.1±0.1	2	--	--	--	0
1a-3[e]	5.0	0.520	1253	3.0±0.2	23.1±0.1	2	10.9±1.6	-5.2±1.4	16.1±2.1	1
1b	3.5	0.570	944	3.5±0.1	23.8±0.3	4	8.4±1.5	-1.5±1.4	9.9±2.1	5
1c	1.5	0.580	1073	4.0±0.1	24.1±0.1	3	3.1±1.5	5.1±1.5	-2.0±2.2	3
1d	1.0	0.550	818	2.6±0.1	22.4±0.3	3	-3.1±1.5	8.4±1.4	-11.4±2.0	3
1d-2	1.0	0.540	1002	2.7±0.1	23.4±0.2	3	6.7±1.5	-1.3±1.4	8.0±2.1	4
1e	0.5	0.560	772	1.4±0.1	19.1±0.1	3	3.3±1.5	-0.5±1.4	3.8±2.0	3
1e-2	0.5	0.570	706	1.0±0.1	18.2±0.1	3	-1.3±1.5	3.4±1.4	-4.7±2.0	3
1e-3	0.5	0.560	739	-0.5±0.9	17.3±0.1	2	-1.7±1.5	0.8±2.1	-2.5±2.6	3
1f	0.25	0.580	363	-0.4±0.8	2.6±0.1	3	-9.4±2.0	8.8±3.6	-18.2±4.1	3
2a	5.0	0.065	263	5.2±0.1	12.3±0.1	3	19.5±1.6	-9.4±1.5	28.9±2.2	5
2b	5.0	0.220	860	2.8±0.2	31.1±0.2	4	15.8±1.6	-10.6±1.5	26.4±2.2	3
2c	5.0	0.380	689	3.0±0.1	28.9±0.2	4	10.8±1.6	-5.0±1.4	15.8±2.1	4
2d	5.0	0.865	1090	6.2±0.2	3.3±0.3	4	16.7±1.6	-4.6±1.4	21.4±2.1	6
3a	5.0	4.720[f]	4305[g]	32.2±0.1	-71.0±0.6	2	77.2±1.7	-13.8±1.4	91.1±2.2	1
3b	5.0	9.760[f]	7391	34.5±0.3	-44.0±0.1	2	70.7±1.7	-2.6±1.4	73.3±2.2	1

3b-2	5.0	9.730[f]	8547[g]	30.8	-42.19	1	70.6±1.7	-9.8±1.4	80.4±2.2	1
4a[h]	5.0	9.850[f]	635	18.8±0.1	-42.2±0.7	3	47.7±1.6	-10.7±1.4	58.4±2.1	4
4b[h,i]	5.0	9.690[f]	363	17.3±0.2	-46.5±0.3	4	42.2±1.6	-8.3±1.4	50.4±2.1	3
JR[j]	5.0	0.556±0.022[k, l]	86±2	0.8±1.9	23.1±1.2	6	1.9±3.7	-0.3±1.1	2.2±3.8	4
JR[j]	5.0	0.886[k]	126	2.8	-0.7±0.7	2	11.5±1.6	-6.1±1.4	17.6±2.1	1

[a] Yield calculated assuming final pressure contains 100% N_2O. [b] N_b = number of measurements of the bulk N_2O isotopic composition. [c] N_{ss} = number of measurements of the site-specific N_2O isotopic composition. [d] 1σ standard deviation. [e] A temperature of -75°C was used for the ethanol slush for this run. [f] Indicates absolute pressure reading on Baratron gauge. [g] N_2O was collected with LN_2 for 5 mins; the yield is multiplied by 3 to compare with the 15 min runs. [h] Performed under static pressure. [i] LN2 was not placed on the Russian doll trap during the discharge time for this run. [j] From Randazzo, Ref. 42. The small discrepancies between this work and that of Randazzo can likely be attributed to differences in sample collection, sample handling procedures and/or the calibration of the IRMS. [k] For the preliminary measurements by Randazzo, the flow rate was modulated by changing the regulator pressure on the zero air tank (between 15 psi and 25 psi) while keeping the metering valve setting constant. This may have produced a slightly different pressure gradient in the discharge region and may account for some of the small differences between the results presented here and those by Randazzo. [l] Average of six samples.

Appendix 5C. Isotopic composition of tropospheric N_2O

Table 5C.1. Summary of isotopic composition measurements for tropospheric N_2O.

#	Date of run(s)[a]	$\delta^{15}N$ (‰ vs. air N_2)	$\delta^{18}O$ (‰ vs. air O_2)	Date of site-specific run(s)[a]	$\delta^{15}N^{\alpha}$ (‰ vs. T&Y air N_2)	$\delta^{15}N^{\beta}$ (‰ vs. T&Y air N_2)	SP (‰ vs. T&Y air N_2)	SP (‰ vs. trop. N_2O)
T1	2015/8/1	6.6	20.0	2015/7/31	17.9	-5.0	22.9	4.2
T2	2015/8/5	6.3	20.3	--	--		--	--
T3	2015/8/13	6.4	20.2	2015/8/15	15.0	-2.4	17.5	-1.2
T4	2015/8/18	6.1	20.0	2015/8/19	18.7	-6.8	25.5	6.8
T5	2015/8/15	6.3	19.8	2015/8/19	18.6	-6.4	25.0	6.3
T6	2015/8/15	6.3	19.8	2015/8/21	17.0	-4.7	21.6	3.0
T7	2015/8/21	6.4	19.9	--	--		--	--
T8	2015/8/24	6.0	19.8	2015/8/25	16.1	-4.2	20.3	1.7
T9	2015/8/26	6.0	19.9	2015/8/25	16.1	-4.2	20.3	1.7
T10	2015/8/26	6.0	19.9	2015/8/27	16.1	-4.2	20.3	1.6
T11	2015/8/28	5.9	20.0	2015/8/27	16.1	-4.6	20.7	2.0
T12	2015/8/28	5.9	20.0	2015/8/29	16.1	-4.6	20.7	2.1
T13	2015/10/10	5.4	20.2	2015/10/5	16.9	-6.3	23.2	4.5
T14	2016/5/19	5.8	20.1	2016/5/23	16.7	-5.4	22.0	3.4
Avg.		**6.1±0.3[b]**	**20.0±0.2**		**16.8±1.1**	**-4.9±1.2**	**21.7±2.2**	**3.0±2.2**

[a] Indicates either a single run or an average of runs on the same day. [b] 1σ standard deviation.

Appendix 5D. Supplementary figures for individual runs

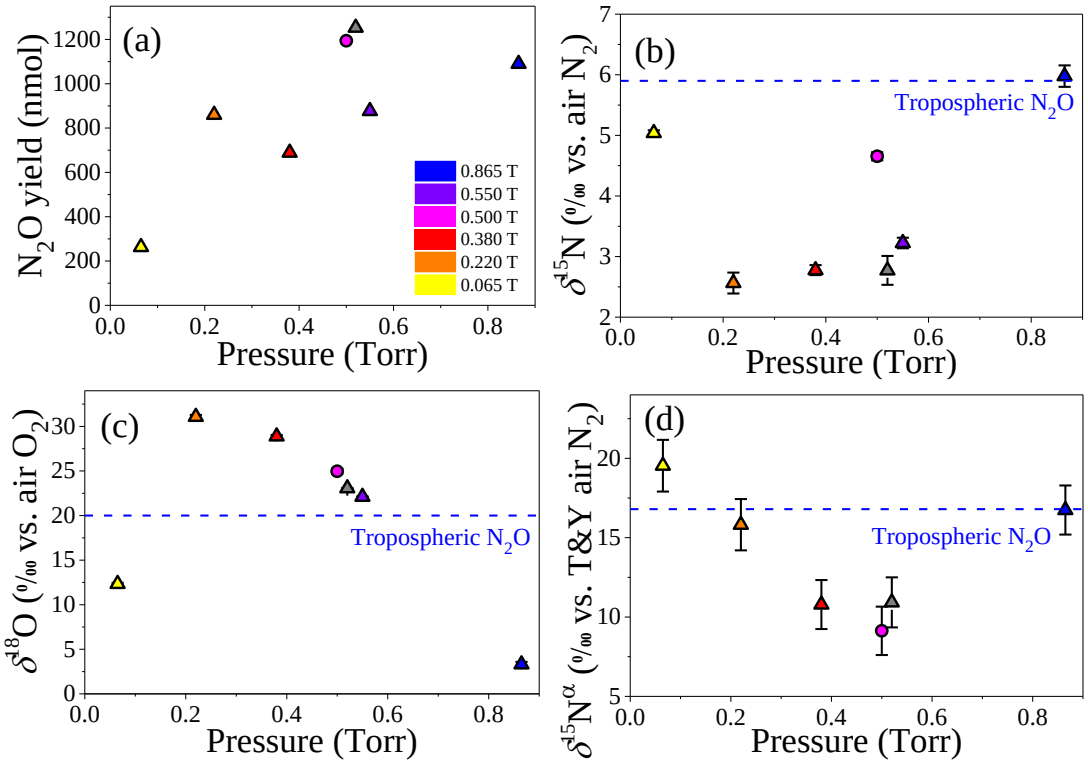

Figure 5D.1. Measured N_2O yields (a) and N_2O isotopic composition (b-d) for all experimental runs (see Appendix 5B) as a function of corona discharge cell pressure for experiments at pressures < 1 Torr at a constant discharge voltage of 5.0 kV (#1a and #2); (b) $\delta^{15}N$ (‰ vs. air N_2), (c) $\delta^{18}O$ (‰ vs. air O_2), (d) $\delta^{15}N^{\alpha}$ (‰ vs. T&Y air N_2). Error bars are 1σ standard deviations of the individual runs. Circle represents sample collected in a 40 mL steel cylinder; triangles represent samples collected in a 10 mL glass tube. Gray symbols represent the sample collected using the -75℃ ethanol slush (Experiment #1a-3). Average values for tropospheric N_2O (see Appendix 5C) are shown as dotted lines.

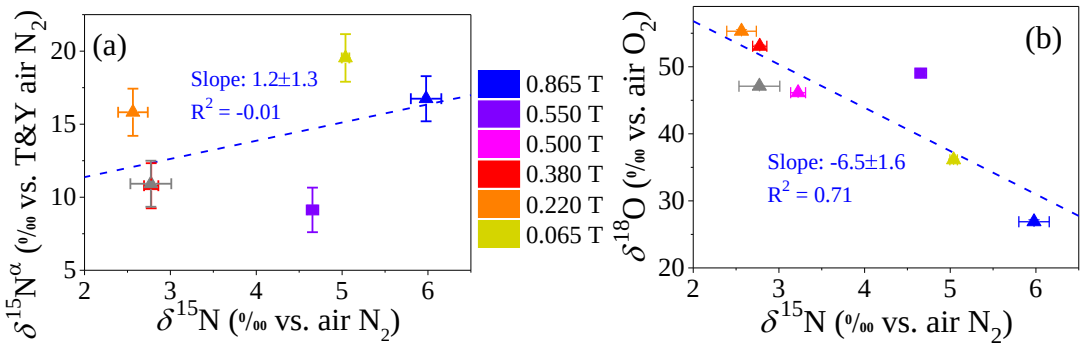

Figure 5D.2. Isotope-isotope plots for (a) $\delta^{15}N^{\alpha}$ vs. $\delta^{15}N$ and (b) $\delta^{15}N$ vs. $\delta^{18}O$ for the results shown in Figure 5D.1. Blue dashed lines represent least-squares linear fits to all data points. (The slopes from the δ-value regressions are the same as those from the more formal ln-ln isotope relationships to within the 1σ uncertainties given.)

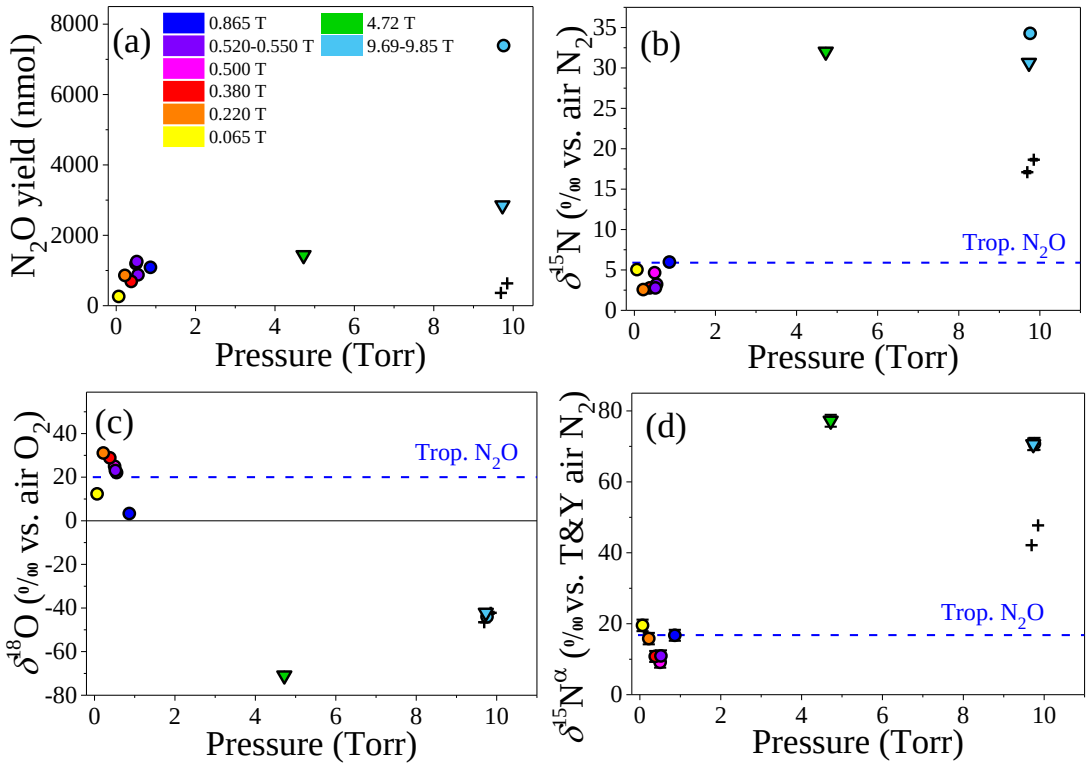

Figure 5D.3. Measured N_2O yields (a) and N_2O isotopic composition (b-d) for all experimental runs (see Appendix 5B) as a function of corona discharge cell pressure for all pressures run at a constant discharge voltage of 5.0 kV (#1a and #2-4); (b) $\delta^{15}N$ (‰ vs. air N_2), (c) $\delta^{18}O$ (‰ vs. air O_2), (d) $\delta^{15}N^{\alpha}$ (‰ vs. T&Y air N_2). Circles represent flow experiments; crosses represent static pressure experiments. Original yields for the 5 min runs are shown with down-pointing triangle symbols (not multiplied by 3 as in Figure 5.3).

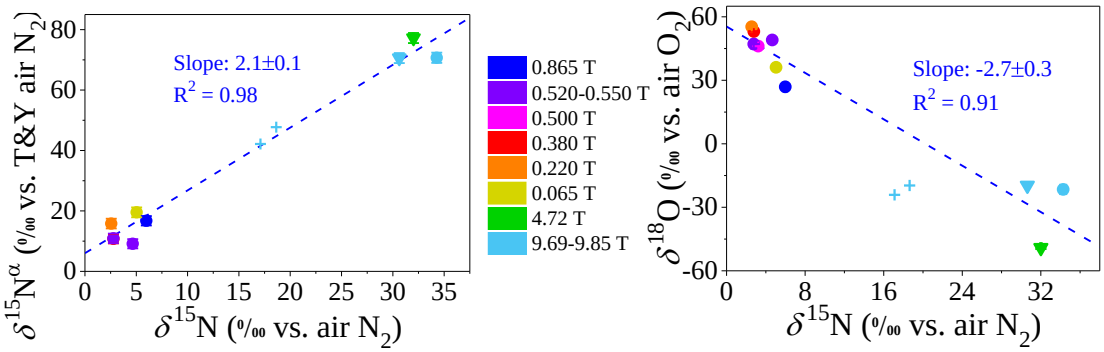

Figure 5D.4. Isotope-isotope plots for (a) $\delta^{15}N^{\alpha}$ vs. $\delta^{15}N$ and (b) $\delta^{15}N$ vs. $\delta^{18}O$ for the results shown in Figure 5D.3. Blue dashed lines represent least-squares linear fits to all data points except the static experiments. (The slopes from the δ-value regressions are the same as those from the more formal ln-ln isotope relationships to within the 1σ uncertainties given.)

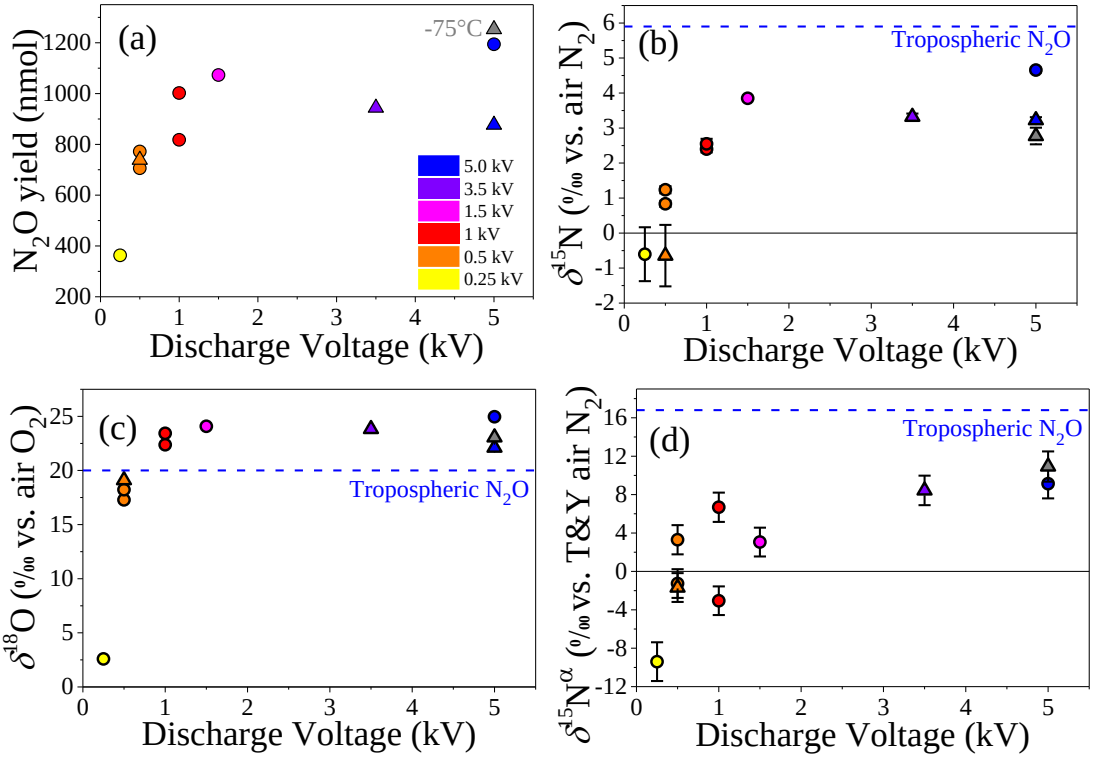

Figure 5D.5. Measured N_2O yields (a) and N_2O isotopic composition (b-d) for all experimental runs (see Appendix 5B) as a function of discharge voltage for all voltages run at a constant pressure of ~0.5 Torr (#1a-1f); (b) $\delta^{15}N$ (‰ vs. air N_2), (c) $\delta^{18}O$ (‰ vs. air O_2), (d) $\delta^{15}N^{\alpha}$ (‰ vs. T&Y air N_2). Average values for current tropospheric N_2O (see Appendix 5C) are shown as dashed lines. Circles represent samples collected in a 40 mL steel cylinder; triangles represent samples collected in a 10 mL glass tube. Gray symbols represent the sample collected using -75°C ethanol slush (Experiment #1a-3).

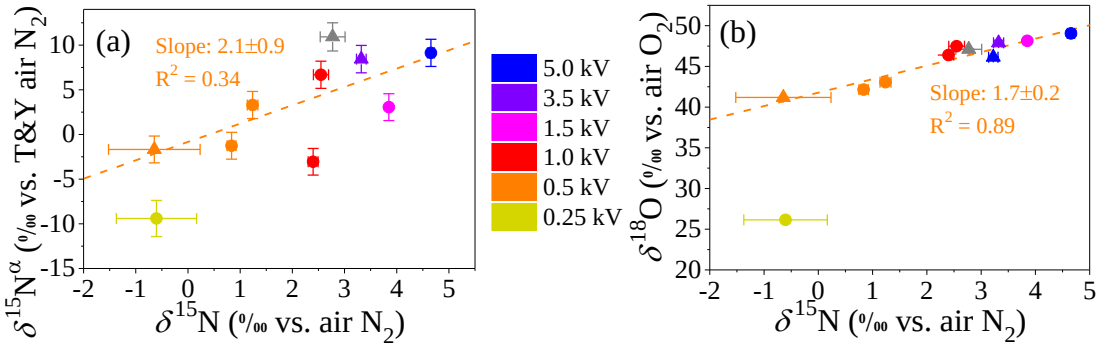

Figure 5D.6. Isotope-isotope plots for (a) $\delta^{15}N^{\alpha}$ vs. $\delta^{15}N$ and (b) $\delta^{15}N$ vs. $\delta^{18}O$ for the results shown in Figure 5D.5. Orange dashed lines represent least-squares linear fits to all data points except 0.25 kV; see text. (The slopes from the δ-value regressions are the same as those from the more formal ln-ln isotope relationships to within the 1σ uncertainties given.)

References

1. Stocker, T. F. et al. IPCC, 2013: Climate change 2013: the physical science basis. Contribution of working group I to the fifth assessment report of the intergovernmental panel on climate change (2013).
2. Davidson, E. A. The contribution of manure and fertilizer nitrogen to atmospheric nitrous oxide since 1860. *Nat. Geosci.* **2,** 659–662 (2009).
3. Park, S. et al. Trends and seasonal cycles in the isotopic composition of nitrous oxide since 1940. *Nat. Geosci.* **5,** 261–265 (2012).
4. Blasing, T. J. Recent Greenhouse Gas Concentrations. Carbon Dioxide Information Analysis Center (2016). Available at: http://cdiac.ornl.gov/pns/current_ghg.html. (Accessed: 13th July 2016)
5. Kyoto Protocol: Targets for the first commitment period. United Nations Framework Convention on Climate Change Available at: http://unfccc.int/kyoto_protocol/items/3145.php. (Accessed: 4th May 2016)
6. Wollenberg, E. et al. Reducing emissions from agriculture to meet the 2 ℃ target. *Glob. Change Biol.* (2016).
7. Stein, L. Y. & Yung, Y. L. Production, isotopic composition, and atmospheric fate of biologically produced nitrous oxide. *Annu. Rev. Earth Planet. Sci.* **31,** 329–356 (2003).
8. Bouwman, L. & United Nations Environment Programme. Drawing down N_2O to protect climate and the ozone layer: a UNEP synthesis report (2013).
9. Schumann, U. & Huntrieser, H. The global lightning-induced nitrogen oxides source. *Atmos. Chem. Phys.* **7,** 3823–3907 (2007).
10. Johnston, H. Reduction of stratospheric ozone by nitrogen oxide catalysts from supersonic transport exhaust. *Science* **173,** 517–522 (1971).
11. Ravishankara, A. R., Daniel, J. S. & Portmann, R. W. Nitrous oxide (N_2O): the dominant ozone-depleting substance emitted in the 21st century. *Science* **326,** 123–125 (2009).
12. Mosier, A. et al. Closing the global N_2O budget: nitrous oxide emissions through the agricultural nitrogen cycle. *Nutr. Cycl. Agroecosystems* **52,** 225–248 (1998).
13. Kroeze, C., Mosier, A. & Bouwman, L. Closing the global N_2O budget: A retrospective analysis 1500–1994. *Glob. Biogeochem. Cycles* **13,** 1–8 (1999).
14. Hirsch, A. I. et al. Inverse modeling estimates of the global nitrous oxide surface flux from 1998–2001. *Glob. Biogeochem. Cycles* **20,** GB1008 (2006).
15. Huang, J. et al. Estimation of regional emissions of nitrous oxide from 1997 to 2005 using multinetwork measurements, a chemical transport model, and an inverse method. *J. Geophys. Res. Atmospheres* **113,** D17313 (2008).
16. Jiang, X. et al. Seasonal cycle of N_2O: Analysis of data. *Glob. Biogeochem. Cycles* **21,** GB1006 (2007).
17. US Department of Commerce, N. ESRL Global Monitoring Division - Halocarbons and other Atmospheric Trace Species. Available at: http://www.esrl.noaa.gov/gmd/hats/. (Accessed: 20th July 2016)
18. Saikawa, E. et al. Global and regional emissions estimates for N_2O. *Atmos. Chem. Phys.* **14,** 4617–4641 (2014).
19. Thompson, R. L. et al. Nitrous oxide emissions 1999 to 2009 from a global atmospheric inversion. *Atmos. Chem. Phys.* **14,** 1801–1817 (2014).

20. Thompson, R. L. et al. TransCom N_2O model inter-comparison – Part 2: Atmospheric inversion estimates of N_2O emissions. *Atmos. Chem. Phys.* **14,** 6177–6194 (2014).
21. Bergamaschi, P. et al. Top-down estimates of European CH_4 and N_2O emissions based on four different inverse models. *Atmos. Chem. Phys.* **15,** 715–736 (2015).
22. Wofsy, S. C. & the HIPPO Science Team and Cooperating Modellers and Satellite Teams. HIAPER Pole-to-Pole Observations (HIPPO): fine-grained, global-scale measurements of climatically important atmospheric gases and aerosols. *Philos. Trans. R. Soc. Math. Phys. Eng. Sci.* **369,** 2073–2086 (2011).
23. Kort, E. A. et al. Tropospheric distribution and variability of N_2O: Evidence for strong tropical emissions. *Geophys. Res. Lett.* **38,** L15806 (2011).
24. Nevison, C. D. et al. Southern Ocean ventilation inferred from seasonal cycles of atmospheric N_2O and O_2/N_2 at Cape Grim, Tasmania. *Tellus* B **57,** 218–229 (2005).
25. Nevison, C. D. et al. Exploring causes of interannual variability in the seasonal cycles of tropospheric nitrous oxide. *Atmos. Chem. Phys.* **11,** 3713–3730 (2011).
26. Park, S., Atlas, E. L. & Boering, K. A. Measurements of N_2O isotopologues in the stratosphere: Influence of transport on the apparent enrichment factors and the isotopologue fluxes to the troposphere. *J. Geophys. Res. Atmospheres* **109,** D01305 (2004).
27. Kaiser, J., Engel, A., Borchers, R. & Röckmann, T. Probing stratospheric transport and chemistry with new balloon and aircraft observations of the meridional and vertical N_2O isotope distribution. *Atmos. Chem. Phys.* **6,** 3535–3556 (2006).
28. Toyoda, S. et al. Temporal and latitudinal distributions of stratospheric N_2O isotopomers. *J. Geophys. Res. Atmospheres* **109,** D08308 (2004).
29. Schmidt, J. A., Johnson, M. S. & Schinke, R. Isotope effects in N_2O photolysis from first principles. *Atmos. Chem. Phys.* **11,** 8965–8975 (2011).
30. Schmidt, J. A. & Johnson, M. S. Clumped isotope perturbation in tropospheric nitrous oxide from stratospheric photolysis. *Geophys. Res. Lett.* **42,** 2015GL063102 (2015).
31. Ostrom, N. E. et al. Isotopologue effects during N_2O reduction in soils and in pure cultures of denitrifiers. *J. Geophys. Res. Biogeosciences* **112,** G02005 (2007).
32. Sutka, R. L., Ostrom, N. E., Ostrom, P. H., Gandhi, H. & Breznak, J. A. Nitrogen isotopomer site preference of N_2O produced by Nitrosomonas europaea and Methylococcus capsulatus Bath. *Rapid Commun. Mass Spectrom.* **17,** 738–745 (2003).
33. Sutka, R. L., Ostrom, N. E., Ostrom, P. H., Gandhi, H. & Breznak, J. A. Nitrogen isotopomer site preference of N_2O produced by Nitrosomonas europaea and Methylococcus capsulatus Bath. *Rapid Commun. Mass Spectrom.* **18,** 1411–1412 (2004).
34. Sutka, R. L. et al. Distinguishing nitrous oxide production from nitrification and denitrification on the basis of isotopomer abundances. *Appl. Environ. Microbiol.* **72,** 638–644 (2006).
35. Pérez, T. et al. Identifying the agricultural imprint on the global N_2O budget using stable isotopes. *J. Geophys. Res. Atmospheres* **106,** 9869–9878 (2001).
36. Pérez, T. et al. Isotopic variability of N_2O emissions from tropical forest soils. *Glob. Biogeochem. Cycles* **14,** 525–535 (2000).
37. Pérez, T. et al. Nitrous oxide nitrification and denitrification ^{15}N enrichment factors from Amazon forest soils. *Ecol. Appl.* **16,** 2153–2167 (2006).

38. Park, S. et al. Can N_2O stable isotopes and isotopomers be useful tools to characterize sources and microbial pathways of N_2O production and consumption in tropical soils? *Glob. Biogeochem. Cycles* **25,** GB1001 (2011).
39. Zhang, W., Li, Y., Xu, C., Li, Q. & Lin, W. Isotope signatures of N_2O emitted from vegetable soil: Ammonia oxidation drives N_2O production in $NH4^+$-fertilized soil of North China. *Sci. Rep.* **6,** 29257 (2016).
40. Ogawa, M. & Yoshida, N. Stable isotope fractionation of nitrous oxide during thermal decomposition and reduction processes. *J. Geophys. Res. Atmospheres* **109,** D19301 (2004).
41. Ogawa, M. & Yoshida, N. Nitrous oxide emission from the burning of agricultural residue. *Atmos. Environ.* **39,** 3421–3429 (2005).
42. Randazzo, J. The effects of high energy processes on atmospheric species: Investigations of isotope effects in the photoionization of N_2 and CO_2 and in the corona discharge formation of N_2O and light-scattering from photochemically-generated aerosols. PhD dissertation, University of California, Berkeley, 2014.
43. Sisterson, D. L. & Liaw, Y. P. An evaluation of lightning and corona discharge on thunderstorm air and precipitation chemistry. *J. Atmos. Chem.* **10,** 83–96 (1990).
44. Hill, R. D., Rinker, R. G. & Coucouvinos, A. Nitrous oxide production by lightning. *J. Geophys. Res.* **89,** 1411–1421 (1984).
45. Bhetanabhotla, M. N., Crowell, B. A., Coucouvinos, A., Hill, R. D. & Rinker, R. G. Simulation of trace species production by lightning and corona discharge in moist air. *Atmos. Environ.* 1967 **19,** 1391–1397 (1985).
46. Kline, L. E., Partlow, W. D., Young, R. M., Mitchell, R. R. & Congedo, T. V. Diagnostics and modeling of RF discharge dissociation in N_2O. *IEEE Trans. Plasma Sci.* **19,** 278–285 (1991).
47. Kossyi, I. A., Kostinsky, A. Y., Matveyev, A. A. & Silakov, V. P. Kinetic scheme of the non-equilibrium discharge in nitrogen-oxygen mixtures. *Plasma Sources Sci. Technol.* **1,** 207 (1992).
48. Levine, J. S. & Shaw, E. F. In situ aircraft measurements of enhanced levels of N_2O associated with thunderstorm lightning. *Nature* **303,** 312–314 (1983).
49. Hill, R. D., Rahmim, I. & Rinker, R. G. Experimental study of the production of NO, N_2O, and O_3 in a simulated atmospheric corona. *Ind. Eng. Chem. Res.* **27,** 1264–1269 (1988).
50. Brandvold, D. K., Martinez, P. & Hipsh, R. Field measurements of O_3 and N_2O produced from corona discharge. *Atmos. Environ.* **30,** 973–976 (1996).
51. Chen, J. & Davidson, J. H. Electron density and energy distributions in the positive DC corona: interpretation for corona-enhanced chemical reactions. *Plasma Chem. Plasma Process.* **22,** 199–224 (2002).
52. Wennberg, P. O., Anderson, J. G. & Weisenstein, D. K. Kinetics of reactions of ground state nitrogen atoms ($^4S_{3/2}$) with NO and NO_2. *J. Geophys. Res. Atmospheres* **99,** 18839–18846 (1994).
53. Funke, B. et al. Enhancement of N_2O during the October–November 2003 solar proton events. *Atmos. Chem. Phys.* **8,** 3805–3815 (2008).
54. Sheese, P. E., Walker, K. A., Boone, C. D., Bernath, P. F. & Funke, B. Nitrous oxide in the atmosphere: First measurements of a lower thermospheric source. *Geophys. Res. Lett.* **43,** 2015GL067353 (2016).
55. Zipf, E. C. A laboratory study on the formation of nitrous oxide by the reaction $N_2(A^3\Sigma_u^+) + O_2 \rightarrow N_2O + O$. *Nature* **287,** 523–524 (1980).

56. Iannuzi, M. P., Jeffries, J. B. & Kaufman, F. Product channels of the $N_2(A^3\Sigma_u^+)$ + O_2 interaction. *Chem. Phys. Lett.* **87,** 570–574 (1982).
57. Fraser, M. E. & Piper, L. G. Product branching ratios from the $N_2(A^3\Sigma_u^+)$ + O_2 interaction. *J. Phys. Chem.* **93,** 1107–1111 (1989).
58. Funke, B. et al. Mesospheric N_2O enhancements as observed by MIPAS on Envisat during the polar winters in 2002-2004. *Atmos. Chem. Phys. Discuss.* **8,** 10561–10596 (2008).
59. DeMore, W. & Raper, O. F. Reaction of $O(^1D)$ with nitrogen. *J. Chem. Phys.* **37,** 2048–2052 (1962).
60. Estupiñán, E. G., Nicovich, J. M., Li, J., Cunnold, D. M. & Wine, P. H. Investigation of N_2O production from 266 and 532 nm laser flash photolysis of $O_3/N_2/O_2$ mixtures. *J. Phys. Chem. A* **106,** 5880–5890 (2002).
61. Cacace, F., de Petris, G., Rosi, M. & Troiani, A. Ionization of O_3 in excess N_2: a new route to N_2O via intermediate $N_2O_3^+$ complexes. *Angew. Chem. Int. Ed.* **40,** 1938–1941 (2001).
62. Midey, A. J., Williams, S., Miller, T. M., Larsen, P. T. & Viggiano, A. A. Investigation of the reaction of O_3^+ with N_2 and O_2 from 100 to 298 K. *J. Phys. Chem. A* **106,** 11739–11742 (2002).
63. Zhu, J., Cao, Z. & Zhang, Q. Theoretical study on reactions of O_3^+ and N_2: novel routes to dinitrogen bond activation. *Chem. Phys. Lett.* **377,** 184–188 (2003).
64. de Petris, G. Atmospherically relevant ion chemistry of ozone and its cation. *Mass Spectrom. Rev.* **22,** 251–271 (2003).
65. Prasad, S. S. A new model of N_2O quantum yield in the UV photolysis of $O_3/O_2/N_2$ mixtures: Contributions of electronically excited O_3 and $O_3 \cdot N_2$. *J. Chem. Phys.* **117,** 10104 (2002).
66. Prasad, S. S. Especially significant new component of N_2O quantum yield in the UV photolysis of O_3 in air. *J. Phys. Chem. A* **109,** 9035–9043 (2005).
67. Prasad, S. S. & Zipf, E. C. Atmospheric production of nitrous oxide from excited ozone and its potentially important implications for global change studies. *J. Geophys. Res. Atmospheres* **113,** D15307 (2008).
68. Fraser, M. E., Tucker, T. R., Piper, L. G. & Rawlins, W. T. N_2O production mechanism from the interaction of discharge-excited species. *J. Geophys. Res. Atmospheres* **95,** 18611–18616 (1990).
69. Zellner, R., Hartmann, D. & Rosner, I. N_2O Formation in the reactive collisional quenching of NO_3* and NO_2* by N_2. *Berichte Bunsenges. Für Phys. Chem.* **96,** 385–390 (1992).
70. Marić, D., Burrows, J. P. & Moortgat, G. K. A study of the formation of N_2O in the reaction of $NO_3(A^2E')$ with N_2. *J. Atmos. Chem.* **15,** 157–169 (1992).
71. Piper, L. G. & Rawlins, W. T. Oxygen-atom yields from microwave discharges in nitrous oxide/argon mixtures. *J. Phys. Chem.* **90,** 320–325 (1986).
72. Hu, X. et al. The destruction of N_2O in a pulsed corona discharge reactor. *Fuel* **81,** 1259–1268 (2002).
73. Cleland, T. A. & Hess, D. W. Diagnostics and Modeling of N_2O RF Glow Discharges. *J. Electrochem. Soc.* **136,** 3103–3111 (1989).
74. Herron, J. T. & Green, D. S. Chemical kinetics database and predictive schemes for nonthermal humid air plasma chemistry. Part II. Neutral species reactions. *Plasma Chem. Plasma Process.* **21,** 459–481 (2001).

75. Gorshunov, N. M. & Gudenko, S. V. Enrichment of the nitrogen atomic component with the ^{15}N isotope in a post-discharge zone. *J. Exp. Theor. Phys. Lett.* **77,** 162–166 (2003).
76. Manuccia, T. J. & Clark, M. D. Enrichment of N^{15} by chemical reactions in a glow discharge at 77 °K. *Appl. Phys. Lett.* **28,** 372–374 (1976).
77. Semeniuk, K. et al. N_2O production by high energy auroral electron precipitation. *J. Geophys. Res. Atmospheres* **113,** D16302 (2008).
78. Davidson, G. & O'Neil, R. Optical radiation from nitrogen and air at high pressure excited by energetic electrons. *J. Chem. Phys.* **41,** 3946 (1964).
79. Gallimberti, I., Hepworth, J. K. & Klewe, R. C. Spectroscopic investigation of impulse corona discharges. *J. Phys. Appl. Phys.* **7,** 880 (1974).
80. Brenninkmeijer, C. A. M. & Röckmann, T. Russian doll type cryogenic traps: Improved design and isotope separation effects. *Anal. Chem.* **68,** 3050–3053 (1996).
81. Croteau, P. et al. Effect of local and regional sources on the isotopic composition of nitrous oxide in the tropical free troposphere and tropopause layer. *J. Geophys. Res. Atmospheres* **115,** D00J11 (2010).
82. Park, S. Measurements of N_2O isotopologues ($^{15}N^{14}NO$, $^{14}N^{15}NO$, and $N_2{}^{18}O$): insights into global biogeochemical cycling and atmospheric chemistry and transport. PhD dissertation, University of California, Berkeley, 2005.
83. Yoshida, N. & Toyoda, S. Constraining the atmospheric N_2O budget from intramolecular site preference in N_2O isotopomers. *Nature* **405,** 330–334 (2000).
84. Kaiser, J. et al. Mass spectrometric method for the absolute calibration of the intramolecular nitrogen isotope distribution in nitrous oxide. *Anal. Bioanal. Chem.* **378,** 256–269 (2003).
85. Severinghaus, J. P., Grachev, A., Luz, B. & Caillon, N. A method for precise measurement of argon 40/36 and krypton/argon ratios in trapped air in polar ice with applications to past firn thickness and abrupt climate change in Greenland and at Siple Dome, Antarctica. *Geochim. Cosmochim. Acta* **67,** 325–343 (2003).
86. Feilberg, K. L., Wiegel, A. A. & Boering, K. A. Probing the unusual isotope effects in ozone formation: Bath gas and pressure dependence of the non-mass-dependent isotope enrichments in ozone. *Chem. Phys. Lett.* **556,** 1–8 (2013).
87. Snider, D. M., Venkiteswaran, J. J., Schiff, S. L. & Spoelstra, J. From the ground up: global nitrous oxide sources are constrained by stable isotope values. *PLOS ONE* **10,** e0118954 (2015).
88. Chen, J. & Davidson, J. H. Ozone production in the positive DC corona discharge: model and comparison to experiments. *Plasma Chem. Plasma Process.* **22,** 495–522 (2002).
89. Toyoda, S. & Yoshida, N. Determination of nitrogen isotopomers of nitrous oxide on a modified isotope ratio mass spectrometer. *Anal. Chem.* **71,** 4711–4718 (1999).
90. Basov, N. G. et al. Isotope separation in chemical reactions occurring under thermodynamic nonequilibrium conditions. *JETP Lett. USSR Engl. Transl.* V 19 No 6 Pp 190-191 (1974).
91. Wang, Y., Desilva, A. W., Goldenbaum, G. C. & Dickerson, R. R. Nitric oxide production by simulated lightning: dependence on current, energy, and pressure. *J. Geophys. Res.* **103,** 19149–19159 (1998).
92. Nna-Mvondo, D., Navarro-González, R., Raulin, F. & Coll, P. Nitrogen fixation by corona discharge on the early Precambrian Earth. *Orig. Life Evol. Biospheres* **35,** 401–409 (2005).

93. Hoering, T. The isotopic composition of the ammonia and the nitrate ion in rain. *Geochim. Cosmochim. Acta* **12,** 97–102 (1957).
94. Ianni, J. C. "A Comparison of the Bader-Deuflhard and the Cash-Karp Runge-Kutta Integrators for the GRI-MECH 3.0 Model Based on the Chemical Kinetics Code Kintecus" in Computational Fluid and Solid Mechanics 2003 (ed. K. J. Bathe, Elsevier Science Ltd., Oxford, UK, 2003).
95. Walters, W. W., Simonini, D. S. & Michalski, G. Nitrogen isotope exchange between NO and NO_2 and its implications for $\delta^{15}N$ variations in tropospheric NO_x and atmospheric nitrate: isotope exchange between NO and NO_2. *Geophys. Res. Lett.* **43,** 440–448 (2016).
96. Gao, Y. Q. & Marcus, R. A. Strange and unconventional isotope effects in ozone formation. *Science* **293,** 259–263 (2001).
97. Ivanov, M. V. & Babikov, D. On molecular origin of mass-independent fractionation of oxygen isotopes in the ozone forming recombination reaction. *Proc. Natl. Acad. Sci.* **110,** 17708–17713 (2013).
98. Sugimitsu, H. & Okazaki, S. Measurement of the rate of ozone formation in an ozonizer. *J Chim. Phys.* **79,** 655–660 (1982).
99. Röckmann, T., Kaiser, J. & Brenninkmeijer, C. A. M. The isotopic fingerprint of the pre-industrial and the anthropogenic N_2O source. *Atmos. Chem. Phys.* **3,** 315–323 (2003).